Annual Report
Grant No. N00014-91-J-4164

September 15, 1991 - September 15, 1992

(2)

ENVIRONMENTALLY ASSISTED CRACKING OF HIGH STRENGTH BETA TITANIUM ALLOYS

Submitted to:

Dr. A. John Sedriks
Materials Division, Code 1131
Office of Naval Research
800 N. Quincy Street
Arlington, VA 22217-5660

Submitted by:

J. R. Scully
Assistant Professor

R. P. Gangloff
Professor

R. G. Kelly
Research Assistant Professor

SEAS Report No. UVA/525461/MSE94/101
November 1993

DEPARTMENT OF MATERIALS SCIENCE AND ENGINEERING

SCHOOL OF
ENGINEERING
& APPLIED SCIENCE

University of Virginia
Thornton Hall
Charlottesville, VA 22903

UNIVERSITY OF VIRGINIA
School of Engineering and Applied Science

The University of Virginia's School of Engineering and Applied Science has an undergraduate enrollment of approximately 1,500 students with a graduate enrollment of approximately 600. There are 160 faculty members, a majority of whom conduct research in addition to teaching.

Research is a vital part of the educational program and interests parallel academic specialties. These range from the classical engineering disciplines of Chemical, Civil, Electrical, and Mechanical and Aerospace to newer, more specialized fields of Applied Mechanics, Biomedical Engineering, Systems Engineering, Materials Science, Nuclear Engineering and Engineering Physics, Applied Mathematics and Computer Science. Within these disciplines there are well equipped laboratories for conducting highly specialized research. All departments offer the doctorate; Biomedical and Materials Science grant only graduate degrees. In addition, courses in the humanities are offered within the School.

The University of Virginia (which includes approximately 2,000 faculty and a total of full-time student enrollment of about 17,000), also offers professional degrees under the schools of Architecture, Law, Medicine, Nursing, Commerce, Business Administration, and Education. In addition, the College of Arts and Sciences houses departments of Mathematics, Physics, Chemistry and others relevant to the engineering research program. The School of Engineering and Applied Science is an integral part of this University community which provides opportunities for interdisciplinary work in pursuit of the basic goals of education, research, and public service.

Annual Report
Grant No. N00014-91-J-4164

September 15, 1992 - September 15, 1993

ENVIRONMENTALLY ASSISTED CRACKING OF HIGH STRENGTH BETA TITANIUM ALLOYS

Submitted to:

Dr. A. John Sedriks
Materials Division, Code 1131
Office of Naval Research
800 N. Quincy Street
Arlington, VA 22217-5660

Submitted by:

J. R. Scully
Assistant Professor

R. P. Gangloff
Professor

R. G. Kelly
Research Assistant Professor

Department of Materials Science and Engineering
UNIVERSITY OF VIRGINIA
SCHOOL OF ENGINEERING AND APPLIED SCIENCE
THORNTON HALL
CHARLOTTESVILLE, VA 22903-2442

SEAS Report No. UVA/525461/MSE94/101
November 1993

Copy No._____

REPORT DOCUMENTATION PAGE

Form Approved
OMB No. 0704-0188

1. AGENCY USE ONLY (Leave blank)	2. REPORT DATE	3. REPORT TYPE AND DATES COVERED
	November 1993	Annual 09/15/92 - 09/15/93

4. TITLE AND SUBTITLE

Environmentally Assisted Cracking of High Strength Beta Titanium Alloys

5. FUNDING NUMBERS

N00014-91-J-4164

6. AUTHOR(S)

J.R. Scully
R.P. Gangloff and R.G. Kelly

7. PERFORMING ORGANIZATION NAME(S) AND ADDRESS(ES)

Department of Materials Science and Engineering
School of Engineering and Applied Science
University of Virginia
Thornton Hall
Charlottesville, VA 22903-2442

8. PERFORMING ORGANIZATION REPORT NUMBER

UVA/525461/MSE94/101

9. SPONSORING/MONITORING AGENCY NAME(S) AND ADDRESS(ES)

Office of Naval Research
800 North Quincy Street
Arlington, VA 22217-5660

10. SPONSORING/MONITORING AGENCY REPORT NUMBER

11. SUPPLEMENTARY NOTES

12a. DISTRIBUTION AVAILABILITY STATEMENT

12b. DISTRIBUTION CODE

13. ABSTRACT (Maximum 200 words)

RESEARCH GOALS

The objective of this integrated research program is to define the conditions under which high strength β-titanium alloys resist environmentally assisted cracking (EAC) in marine environments. Specific goals are to: (1) characterize EAC for metallurgical, chemical and mechanical conditions that could destabilize crack tip passive films to promote local dissolution and hydrogen (H) uptake, (2) test the hydrogen embrittlement mechanism for EAC, and (3) develop a mechanism-based model of EAC by integrating crack chemistry, surface dissolution and repassivation kinetics, hydrogen uptake to trap sites, and crack tip process zone micromechanics and damage.

RESULTS

The following conclusions were established in FY 93 based on rising load fracture mechanics experiments with solution treated and peak aged Ti-15-3 (15V-3Cr-3Al-3Sn; wt%)

14. SUBJECT TERMS	15. NUMBER OF PAGES
titanium alloys, hydrogen embrittlement, mechanical properties, intergranular cracking, transgranular cracking, microstructure, alpha precipitates, Beta phase, hydrides, passive film, Beta titanium alloys, fracture threshold	5
	16. PRICE CODE

17. SECURITY CLASSIFICATION OF REPORT	18. SECURITY CLASSIFICATION OF THIS PAGE	19. SECURITY CLASSIFICATION OF ABSTRACT	20. LIMITATION OF ABSTRACT
Unclassified	Unclassified	Unclassified	Unlimited

and Beta 21S (Ti-15Mo-3Nb-3Al; wt%) in aqueous NaCl. This work is detailed in the attached paper: L.M. Young, G.A. Young, Jr., J.R. Scully and R.P. Gangloff, "Aqueous Environment Enhanced Crack Propagation in High Strength Beta Titanium Alloys", *Metall. Trans. A*, in review, 1993.

- oo The susceptibility of β-21S to intergranular environment assisted cracking (EAC), compared to the resistance of Ti-15-3, correlates with preferential and copious α-colony precipitation on β grain boundaries of the former. Grain boundary α (and planar slip, as discussed below) are promoted by long time and high temperature processing. Processing of β-titanium alloys must be controlled for EAC resistance.

- oo While susceptible to EAC under rising load in NaCl, β-21S is not prone to intergranular cracking at static stress intensity levels, approaching K_{IC}, over comparable loading times.

- oo Ultra-low amplitude cyclic loading does not promote EAC in β-21S when superposed with high static stress intensities. Calculated crack tip surface plastic strains and average strain rates should be sufficient to promote crack tip surface depassivation and H uptake, however, microscopic plasticity in the process zone appears to be insufficient for EAC damage. "Ripple loading" at higher stress intensity ranges produces *transgranular* fatigue crack growth, however, this behavior is equivalent for Ti-15-3 and β-21S in both NaCl and moist air; there is no evidence of a unique environmental mechanism of ripple load damage.

- oo Existing continuum mechanics models of crack tip strain and strain rate fields are insufficient for micromechanical modeling of loading rate effects on EAC.

- oo EAC in Beta-21S may proceed by hydrogen environment embrittlement. The beneficial effects of cathodic polarization and slow crack tip strain rates are speculatively traced to reduced hydrogen production at the occluded crack tip for the former, and increased crack tip passive film stability or reduced dislocation transport of hydrogen for the latter.

- oo The 25°C NaCl EAC resistance of properly processed peak aged β-titanium alloys is superior to that of quenched and tempered martensitic steels at similar high yield strengths.

Limited work investigated the effect of sulfate reducing bacteria (SRB) on aqueous environment enhanced fatigue. (R.P. Gangloff and R.G. Kelly, "Microbe Enhanced Environmental Fatigue Crack Propagation in HY130 Steel", *Corrosion*, in press, 1993.)

- oo SRB, specifically *Desulfovibrio vulgaris* in Postgate C solution, greatly enhance fatigue crack propagation rates and reduce fatigue crack initiation life for a martensitic alloy steel (HY130) under cathodic polarization (-1000 mV_{sce}). Transgranular fatigue cracking in sterile NaCl becomes intergranular due to the SRB. Metabolic sulfide-enhanced atomic hydrogen uptake and crack tip process zone hydrogen embrittlement

conducting this work will be supported by an NSF fellowship.

- oo Employ Ion Chromatography and Capillary Electrophoresis to measure crack solution chemistry as a function of time during loading, applied electrode potential, and ultra-low amplitude cyclic loading in order to assess the effects of these factors on crack surface reactions and EAC.

- oo Begin to develop a high resolution characterization experiment and mechanics analysis to probe blunt-notch surface film stability, environmental hydrogen uptake and process zone damage evolution in a model β-titanium microstructure.

- oo Hydrogen embrittlement studies will be undertaken on solution treated and aged Beta C. Mechanical studies will include fracture initiation toughness on compact tension samples under slow rising load, as well as notched tensile samples with finite element analyses of stress and strain. Results will be correlated with precipitation behavior, deformation mode, hydrogen trap analysis, and fracture morphology.

- oo Electrochemical studies will continue in order to develop the elements necessary to explain both hydrogen controlled and dissolution controlled aqueous cracking phenomena.

Studies of the electrochemistry, passivity, and repassivation kinetics of β-titanium alloys lead to the following conclusions:

- oo Solid solution Mo in β-21S promotes spontaneous passivation in 5M HCl; while an active-passive transition is observed for V stabilized Ti-15-3 (solution treated), commercially pure α and $\alpha + \beta$ titanium alloys. Mo-lean α precipitates in β-21S are prone to active dissolution in concentrated HCl roughly simulating crack tip chemistry. (D.G. Kolman, J.R. Scully, "The Passivity and Electrochemistry of a Ti-Mo-Nb β-Titanium Alloy in Ambient Temperature Aqueous Sodium Chloride Solution", *J. Electrochem. Soc.*, Vol. 140, No. 10, October, 1993.)

- oo Scratch repassivation studies indicate that peak anodic current densities, peak cathodic current densities, and repassivation rates are similar for solution treated or aged Ti-15-3 compared to β-21S in both neutral NaCl and acidified chloride simulating a crack tip chemistry. The difference in EAC susceptibility between Ti-15-3 and β-21S is currently traced to metallurgical factors (deformation mode and/or α precipitates), rather than intrinsic differences in bare electrode electrochemical reaction kinetics.

In addition to these papers, two Master of Science Dissertations were published:

G.A. Young, Jr., "Hydrogen Effects in Metastable β-Titanium Alloys", M.S. Thesis, University of Virginia, Charlottesville, VA, 22901. (Advised by Scully)

L.M. Young, "Environment Assisted Cracking in β-Titanium Alloys", M.S. Thesis, University of Virginia, Charlottesville, VA, 1993. (Advised by Gangloff)

These students graduated in FY93.

RESEARCH PLANS FOR FY 94

Four graduate students (B.P. Somerday, J.A. Grandle, David G. Kolman and Michelle Gaudett) will conduct the following research in FY94.

- oo Characterize the aqueous chloride environmental cracking resistance of both solution treated and peak aged Beta C (Ti-8V-6Cr-4Mo-4Zr, obtained from RMI Titanium), employing both the rising load and constant stress intensity fracture mechanics methods, and as a function of applied electrode potential as well as crack tip strain rate.

- oo Further define the effect of grain boundary α, and associated thermo-mechanical processing on EAC in β-titanium alloys.

- oo Establish the effect of sulfate reducing bacteria on the EAC resistance of peak aged β-21S as well as both solution treated and peak aged Beta C. The graduate student

are implicated.

- oo Environmental fatigue crack growth kinetics are highly transient due to time-dependent SRB population growth and metabolite concentration increases, as well as to metabolite ion transport in bulk or crack solution and to H diffusion in the metal.

The following conclusions were reached based on internal hydrogen embrittlement (IHE) studies of solution treated and aged Ti-15-3 and β-21S.

- oo Total hydrogen concentrations as low as 500 wt. ppm produce IHE in precracked specimens of peak aged Ti-15-3 and β-21S. The degree of embrittlement is a function of hydrogen concentration, constraint, and yield strength for material with a susceptible microstructure. These results suggest that 900 ppm total hydrogen is required to produce the low threshold stress intensity values observed for β-21S in aqueous NaCl.

- oo An embrittlement threshold of approximately 1000 wt. ppm total hydrogen was observed for blunt notched tensile specimens of peak aged Ti-15-3 and β-21S. (G.A. Young, Jr., J.R. Scully, "The Influence of Hydrogen on the Mechanical Properties of a Ti-Mo-Nb Alloy", *Scripta. Metall.*, Vol. 23, pp. 507-512, 1993. and G.A. Young, Jr., J.R. Scully, "Internal Hydrogen Embrittlement of Solution Heat Treated and Aged Ti-15V-3Cr-3Al-3Sn and Ti-15Mo-3Nb-3Al, *Corrosion J.*, in review, 1993.)

- oo Long time/high temperature solution treatments promote localized planar slip in solution treated β-21S and 15-3. This deformation mode lowers strength and ductility in the presence of internal hydrogen. Fine intragranular α precipitates in aged β-titanium alloys could be readily sheared by dislocations, further promoting planar slip. NaCl EAC in peak aged β-21S, but EAC resistance for Ti-15-3, may be governed by planar slip in the former but not in the latter. (G.A. Young, Jr., J.R. Scully, "Internal Hydrogen Embrittlement of Solution Heat Treated and Aged Ti-15V-3Cr-3Al-3Sn and Ti-15Mo-3Nb-3Al, *Corrosion J.*, in review, 1993.)

- oo Hydriding of a large volume fraction of α and β is not required for IHE of these high strength β-titanium alloys. Hydriding of α was only observed when surface connected α was exposed to electrochemical reactions. Internal hydrogen preferentially partitions to the bcc β matrix. The possibility exists for deformation assisted or highly localized hydriding of α-β interfaces. (G.A. Young, Jr., J.R. Scully, "The Influence of Hydrogen on the Mechanical Properties of a Ti-Mo-Nb Alloy", *Scripta. Metall.*, Vol. 23, pp. 507-512, 1993. and G.A. Young, Jr., J.R. Scully, "Internal Hydrogen Embrittlement of Solution Heat Treated and Aged Ti-15V-3Cr-3Al-3Sn and Ti-15Mo-3Nb-3Al, *Corrosion J.*, in review, 1993.)

- oo A finite element model was developed to determine stress and strain fields in notched tensile bars under applied loads at high triaxial constraint. This capability will be used for micromechanical modelling of EAC and IHE.

MICROBE ENHANCED ENVIRONMENTAL FATIGUE CRACK PROPAGATION IN HY130 STEEL

Richard P. Gangloff
Robert G. Kelly

(Accepted for Publication in Corrosion)

MICROBE ENHANCED ENVIRONMENTAL FATIGUE CRACK PROPAGATION IN HY130 STEEL

Richard P. Gangloff [a] and Robert G. Kelly [b]

Department of Materials Science and Engineering
University of Virginia
Charlottesville, VA 22903

ABSTRACT

The objective of this research is to characterize the effect of sulfate reducing bacteria (SRB) on aqueous environment enhanced fatigue cracking in a high strength alloy steel. *Desulfovibrio vulgaris* in Postgate C solution greatly increases rates of ambient temperature fatigue crack propagation (FCP) in tempered martensitic HY130 steel under cathodic polarization and low frequency, constant stress intensity range loading. Crack growth rates in the SRB solution are increased by 50 to 1000-fold relative to FCP in sterile NaCl solution at -1000 mV_{sce} and vacuum, respectively. The presence of microbes shifts fatigue cracking from a transgranular path, typical of sterile NaCl, to an intergranular crack path consistent with the enhanced growth rates. The SRB reduce fatigue crack initiation resistance, countering the beneficial effect of cathodic polarization for sterile NaCl. Increased hydrogen uptake at the occluded crack tip, due to bacterially-produced $HS^-/S^=$, and metal embrittlement are implicated. SRB do not appear to colonize the occluded alkaline crack tip. Constant ΔK, transient environmental FCP in the SRB solution is substantial, and most likely due to time-dependent bacterial growth and enhanced metabolically reduced sulfides. Other time-dependent hydrogen sources may be important.

---

[a] Professor of Materials Science and Engineering.

[b] Research Assistant Professor of Engineering and Applied Science.

BACKGROUND

Of the variables studied to date, reduced sulfur species dissolved in aqueous chloride solution have the most deleterious effect on environment enhanced fatigue crack propagation (FCP) in steels[1]. In conjunction with cathodic polarization, gaseous H_2S in chloride solution increases FCP rates in low strength C-Mn steels by 300-fold over rates in vacuum[2]. This dramatic increase overwhelms a 15-fold increase in growth rates observed for freely corroding specimens in seawater and a 40-fold increase for FCP under cathodic protection[3]. Sulfide-bearing environments also degrade the monotonic load cracking (stress corrosion cracking or SCC) resistance of steels, particularly for higher strength levels[4]. Sulfur species are present in sour gas wells and papermaking process solutions, and develop due to the metabolic action of sulfate reducing bacteria (SRB)[5-7].

The deleterious effect of SRB on FCP in C-Mn steels has been documented[8-10]; however, data and mechanistic understanding are limited. Thomas *et al.* showed that the decomposition of marine algae in estuary silt by SRB led to a 60 to 120-fold increase in FCP rates under free corrosion conditions or with mild cathodic polarization[8]. SRB effects on cracking in moderate to high strength alloy steels have not been characterized[1,11]. Understanding of SRB effects is hindered by several factors. Fatigue experiments generally yield steady state cracking kinetics and neglect transient growth rates. The bacterial environment chemistry generally changes with time as the bacterial population progresses through different growth stages[12,13]. The chemical composition of the solutions is complex, both biologically and electrochemically. SRB may populate test chamber surfaces, boldly exposed fatigue specimen surfaces and areas within the occluded crack. The relative importance of SRB at each location has not been defined. Finally,

the basic chemo-mechanical mechanisms for environment enhanced fatigue cracking are unclear, even for steels in sterile NaCl solutions[1]. Both anodic dissolution and cathodic hydrogen production processes are important.

Cathodic protection is used to retard both general corrosion and fatigue crack initiation in steels exposed to sterile and SRB containing marine environments[1,14-16]. Protection against general corrosion in SRB environments requires larger applied cathodic potentials than in sterile solutions[15,16], supporting the cathodic depolarization theory of SRB influenced corrosion. Since SRB prefer near-neutral pH conditions, the local alkalinity produced by cathodic polarization might retard their growth[10]. The anodic reaction rate (iron dissolution) is also decreased by cathodic polarization and the contributions of each effect have not been delineated. Cathodic polarization effects on FCP are complex for sterile environments[1], and have not been characterized for biologically inoculated solutions.

The objectives of this study are: (1) to characterize the effect of SRB on environmental FCP in a moderate strength alloy steel, including the influence of cathodic polarization, and (2) to make a first assessment of the location of embrittling bacterial colonies and their metabolites with respect to the fatigue crack tip process zone.

EXPERIMENTAL PROCEDURE

Material

HY130 alloy steel (Fe-0.1 C-0.4 Mn-5.3 Ni-0.5 Cr-0.6 Mo-0.2 Si-0.06 V; by wt %) was investigated in the quenched and tempered condition. Oversized specimen blanks were austenitized (830°C for 90 minutes) in flowing argon, water quenched and tempered in a salt bath

at 610°C for 60 minutes to produce a hardness of R_C 33, a prior austenite grain size of 30 μm, and a calculated tensile yield strength of 1040 MPa[11].

Fatigue Crack Growth Rate Measurement

Fracture mechanics single edge notched tension (SENT) specimens (5.1 mm thick, 38.1 mm wide, 10.2 mm deep edge notch) in the LT orientation were employed for fatigue crack growth rate measurements. Pin gripping with free rotation and maximum load levels were consistent with the boundary conditions of the stress intensity solution and small scale yielding, respectively[11].

Fatigue experiments were conducted in a computer-controlled servohydraulic test machine operated in load control. Crack growth was continuously monitored by direct current electrical potential measurements. Real-time computer control guaranteed constant applied stress intensity range ($\Delta K = K_{max} - K_{min}$) at low constant stress ratio ($R = K_{min}/K_{max} = 0.10$) and a constant loading frequency of either 1 Hz (for crack initiation) or 0.1 Hz (for FCP). Additional experiments were conducted with a single specimen at R values between 0.1 and 0.85; K_{max} was constant as ΔK levels were incrementally decreased to avoid delay retardation. A constant frequency of either 1 Hz or 5 Hz was maintained. Electrical potential-derived crack lengths were linearly corrected based on the difference between predicted and optically measured crack lengths from the fractured specimen. Fatigue crack growth rates were calculated by linear regression analysis of crack length versus load cycles data for each constant ΔK and R condition.

Aqueous Environment Control

Two aqueous environments were investigated, 3% NaCl and a bacteriological medium, both at near-neutral pH and 23°C. For the latter, *Desulfovibrio vulgaris* bacteria were cultivated

in deaerated Postgate Medium C (in g/l of distilled water: 6.0 lactic acid, 4.5 Na_2SO_4, 1.0 yeast extract, 1.0 NH_4Cl, 0.5 KH_2PO_4, 0.3 hydrated sodium citrate, 0.06 hydrated $CaCl_2$, 0.06 hydrated $MgSO_4$, 0.004 hydrated $FeSO_4$) stored in 15 ml vials.

For each environment, the central portion of the edge cracked specimen was immersed in a sealed plexiglass chamber of 1 liter volume as shown in Fig. 1. No dissimilar metal contacted the immersed portion of the specimen. All tubing and fittings were PTFE and the electrolyte was argon deaerated. The grounded specimen was maintained at a constant electrode potential of -1000 mV_{SCE} by a Wenking potentiostat in conjunction with a Ag/AgCl reference electrode and two platinum counter electrodes. The reference electrode was located adjacent to the notch mouth, while the two counter electrodes were normal to and about 5 cm from the broad faces of the SENT specimen. The reference and counter electrodes contained 3% NaCl, and were isolated from the test solution by asbestos frits. The sterile 3% NaCl solution was peristaltically pumped at 30 ml/min through the chamber, and solution in the chamber was continuously deaerated with argon. For experiments with SRB, 45 ml of bacterial solution was added to the cell which contained 550 ml of Postgate Medium C, diluted by 400 ml of distilled water and fully argon deaerated. This environment was statically maintained during the FCP experiment. Specimens were immersed in the bacterial solution for 4 hours prior to fatigue loading.

These corrosion fatigue procedures are detailed elsewhere[11,17].

RESULTS AND DISCUSSION

Results are considered in four sections. The first characterizes the effect of SRB on

fatigue crack growth in HY130 steel under cathodic polarization. The second section describes the microscopic fatigue crack paths, as related to both the cracking kinetics and the presence of the SRB. The third section demonstrates the deleterious effect of SRB on fatigue crack initiation resistance. The discussion qualitatively explains these results from the hydrogen embrittlement perspective, the generally accepted mechanism for FCP in the high strength steel/aqueous solution system.

SRB-Enhanced Fatigue Crack Growth

The strong and damaging effect of SRB on FCP in HY130 steel is demonstrated by the crack growth rate (da/dN) versus applied stress intensity range (ΔK) data in Fig. 2. The FCP behavior of HY130 steel in moist air and vacuum is shown by two dashed lines which represent extensive literature data for C-Mn and alloy steels[1,11]. Growth rates at ΔK above 20 MPa$\sqrt{m}$ were measured at several constant ΔK levels, a single constant R value (0.10) and a constant loading frequency of 0.1 Hz. Below ΔK of 20 MPa$\sqrt{m}$, K_{max} was maintained constant at 33 MPa$\sqrt{m}$ as ΔK was step-reduced (and R was step-increased) after each increment of steady-state FCP was obtained at frequencies of 1 or 5 Hz. This procedure minimizes the complicating mechanical effect of fatigue crack closure, and produces unique growth rate relationships for fatigue in moist air and vacuum where intrinsic R-value effects are not likely[1,11]. Limited FCP data for HY130 steel in moist air (○), obtained with this constant $\Delta K/K_{max}$ procedure, are in excellent agreement with the literature results shown by the dashed line.

The sterile NaCl environment with cathodic polarization at -1000 mV_{sce}[c] increases da/dN

---

[c] Polarization to -1000 mV_{SCE} required application of cathodic currents, on the order of 500 $\mu A/cm^2$ for each deaerated aqueous environment.

by 4-fold relative to moist air and 30-fold relative to vacuum for HY130 steel at a wide range of ΔK and R. Da/dN depends on ΔK raised to the 2.9 power below 20 MPa√m and the 1.6 power above this ΔK level. This environmental effect is typical of the behavior of a wide variety of C-Mn and alloy steels in aqueous chloride[1,11,17,18]. *Desulfovibrio vulgaris* in diluted Postgate Medium C (-1000 mV_{sce}) enhances crack growth rates by up to 1000 times relative to vacuum, 100-fold relative to air and 40-fold compared to 3% NaCl, as indicated by the filled triangular data points in Fig. 2.[d] While crack growth experiments were not conducted in diluted Postgate Medium C without SRB, this environment is likely to enhance da/dN similar to sterile NaCl[1]. The deleterious effect of SRB demonstrated in Fig. 2, specific to cathodic polarization at -1000 mV_{SCE}, is comparable to published data for SRB enhanced crack growth in C-Mn steels under freely corroding and mildly cathodic (-850 mV_{SCE}) conditions[8,9]. Substantial cathodic protection does not mitigate the deleterious effect of SRB on environmental FCP in HY130 steel.

The importance of the deleterious SRB effect is demonstrated in Fig. 3. Trend lines from extensive literature data represent the environmental FCP behavior of a wide range of C-Mn and alloy steels, cyclically loaded at R of 0.05 and a frequency of 0.1 Hz in 3.5% NaCl (sterile) at a fixed cathodic potential of -1000 mV_{sce}[1]. The two filled data points for the steady state low R-low frequency SRB environment are replotted from Fig. 2, and are represented by a power-law ($da/dN \propto \Delta K^{1.6}$) parallel to the sterile NaCl results in Fig. 2. (These two da/dN values for HY130/SRB are equally consistent with a relationship parallel to the $\Delta K^{1.2}$ dependence indicated by the open circle literature results for HY130 steel in sterile NaCl, Fig. 3.) While the effects

---

[d] The da/dN-ΔK dependence for the steady-state SRB case in Fig. 2 was plotted parallel to the data for HY130 steel in sterile NaCl and should be interpreted with caution because R increases with decreasing ΔK. The intrinsic effect of stress ratio on environmental FCP in steels is undefined.

of steel yield strength and microstructure are less than a factor of 2 on FCP rate at any ΔK, the SRB dramatically enhance da/dN by up to two orders of magnitude.

Environmentally enhanced FCP in steels of yield strength below about 1200 MPa, exposed to sterile aqueous chloride at various cathodic electrode potentials (see Fig. 3), generally occurs at cyclic stress intensity levels well below the threshold stress intensity for monotonic load cracking, K_{ISCC} (that is, both K_{max} and K_{min} in the fatigue cycle are below K_{ISCC})[1]. For such cases, environmental FCP is both time- and load cycle-dependent. Considering the HY130/sterile NaCl (-1000 mV_{sce}) system, K_{ISCC} equals 110 $MPa\sqrt{m}$[19] and the data in Fig. 2 represent FCP at K levels well below this monotonic threshold. K_{ISCC} for steels at this yield strength is lowered to perhaps 20 $MPa\sqrt{m}$ by acid and gaseous H_2S additions to NaCl (e.g., the solution defined in NACE Standard MRO175), and time-dependent crack growth rates (da/dt) are rapid[4]. K_{ISCC} is, however, unknown for quenched and tempered steels in the SRB solution. The potency of SRB-enhanced FCP indicates that SCC could be produced by particular metallurgical, biological and electrochemical conditions. This issue must be examined.[e]

When the applied ΔK is maintained at a constant level, FCP in steels exposed to sterile NaCl generally is steady-state after minimal short-term transient growth. That is, crack length increases linearly with the number of load cycles for constant applied ΔK. For sterile NaCl (as well as moist air and vacuum), each point in Fig. 2 resulted from such a linear record; transient FCP was not observed.

---

[e] For environmental FCP above K_{ISCC}, and with high da/dt, da/dN depends on ΔK raised to a power between 10 and 40 at cyclic K levels near K_{ISCC}, followed by essentially ΔK-independent behavior at higher ΔK[1]. The HY130/SRB growth rates in Fig. 2 are only of the above-K_{ISCC} type if K_{ISCC} is less than 10 $MPa\sqrt{m}$. Alternately, since similar power-law da/dN-ΔK relationships are observed for HY130 in moist air (ΔK exponent of 2.5), sterile NaCl (2.9 and 1.6), and the SRB environment (1.6), the FCP behavior in Fig. 2 could be of the below-K_{ISCC} type.

In sharp contrast to sterile NaCl, transient crack growth was observed for the SRB environment. Figure 4 shows measured values of fatigue crack length versus loading cycles which were analyzed to yield a portion of the da/dN versus ΔK data in Fig. 2. In this experiment, a single HY130 specimen was immersed in SRB plus diluted Postgate C with cathodic polarization at -1000 mV_{sce} for four hours without loading. The fatigue crack was then grown from the notch (depth of 10.2 mm) to a depth of 1.46 mm (total notch plus crack length = 11.66 mm) over 8100 cycles at 1 Hz (2.3 hour exposure). After this initial crack growth, constant ΔK (20.8 MPa$\sqrt{m}$, R = 0.1) loading commenced at 0.1 Hz. As this loading continued from 8,100 to 10,800 cycles (over 7.5 hours), the FCP rate accelerated from 8.9×10^{-4} to 2.0×10^{-3} mm/cycle. Since crack length did not linearly increase with loading cycles, steady-state FCP was not achieved during Day 1. The specimen was maintained in the SRB solution for 12 hours without load, and the experiment was reinitiated at the same constant ΔK and frequency (Day 2 in Fig. 4). The resultant crack advance was essentially linear for a time period of 1.2 hours and at an average rate of 7.2×10^{-3} mm/cycle, indicating that steady state was achieved.

The initial SRB rate on Day 1 (the open triangle in Fig. 2) is slightly higher than the da/dN value typical of FCP in sterile NaCl, while increasingly rapid rates are observed during Day 1 (as shown by the arrow from the open triangle). The steady state behavior observed during Day 2 is represented by the filled triangle labelled "1" in Fig. 2. Subsequent sequential crack growth experiments, labelled "2" and "3" in Fig. 2, were conducted over a period of 48 hours at different ΔK and R, and yielded essentially linear a versus N data. The trend line in Fig. 2 approximates steady-state FCP for HY130 in the SRB solution; da/dN depends on ΔK raised to the 1.6 power, similar to the behavior of C-Mn steel in H_2S saturated chloride solution,

however, a wider range of ΔK must be examined[2].

Bacteria concentrations and dissolved H_2S levels were not measured during these experiments. The SRB solution continuously darkened during the first day of the experiment and H_2S was formed in the cell based on smell. These observations indicate increasing bacterial activity, coincident with the accelerating crack growth rates. It is likely that a constant SRB environment condition was achieved, but only after the first day[12,13]. Additional factors may cause transient FCP for the SRB case, as considered in the section on the cracking mechanism.

These results demonstrate that SRB environmental effects must be considered in damage tolerant analyses of fatigue in marine structures[20]. Such work will be complicated because da/dN can change with exposure time at constant ΔK due to varying biological environment chemistry. Fracture mechanics growth rate similitude, in conjunction with steady state da/dN versus ΔK data, may not adequately describe component performance.[f] The data in Fig. 2 may provide a reasonable upper bound da/dN-ΔK relationship for HY130 steel in SRB of essentially constant activity. Studies of metallurgical effects on corrosion fatigue, for example weld HAZ behavior, must include SRB chemical variables such as the cultivating medium. From a practical perspective, significant cathodic polarization did not mitigate the deleterious effect of SRB on either FCP or fatigue crack initiation (as presented in an ensuing section), in agreement with the work of Edyvean and coworkers[10]. FCP may be more severely enhanced by the SRB in the presence of mild anodic polarization or under free corrosion conditions.

---

[f] Paris, Wei and coworkers experimentally demonstrated the principle of fracture mechanics similitude for FCP; that is, equal da/dN are produced for equal applied ΔK independent of applied load, crack size and component or specimen geometry[21,22]. Similitude enables integration of laboratory da/dN-ΔK data to predict component fatigue behavior; in terms of either applied stress range versus total life, or crack length versus applied load cycles; for any initial defect size and component configuration.

SRB-Sensitive Fatigue Crack Surface Morphology

Environmental fatigue crack surfaces were examined by scanning electron microscopy (SEM). Results contained in Fig. 5 demonstrate the strong embrittling effect of *Desulfovibrio vulgaris* on FCP in HY130 steel. (All fractographs are oriented with the fatigue crack growth direction from top to bottom and the crack front parallel to the horizontal direction.) Figure 5a shows the crack morphology typical of environmental FCP in sterile NaCl at -1000 mV_{sce}. Cracking is entirely transgranular, and most probably associated with environment-enhanced martensite lath interface cracking and crystallographic cracking along a low index plane through the tempered martensite[11]. The environmental crack path illustrated in Fig. 5a is different from that which is typical of FCP in HY130 steel stressed in either moist air or vacuum. For these benign environments, FCP is transgranular, but involves crack tip plasticity damage independent of environment-embrittled martensite.

In contrast to the vacuum and sterile NaCl cases, *Desulfovibrio vulgaris* in diluted Postgate C promotes intergranular cracking, the increasing proportion of which correlates with increasing FCP rates.[g] Figure 5b illustrates that SRB enhanced cracking on Day 1 progressed by a mixture of transgranular and intergranular separation. Qualitatively, the proportion of transgranular cracking is equal to or greater than the amount of intergranular separation, as suggested in Fig. 5b. This mixed morphology is consistent with the modestly enhanced crack growth rate relative to fully transgranular FCP in sterile NaCl (Fig. 2). Crack growth in SRB during Day 2, Fig. 5c, occurred by a larger proportion of intergranular separation, correlating

---

[g] Fatigue cracking in the SRB environment is intergranular with respect to prior austenite boundaries in HY130 steel.

with the increase in bacterial activity and increased da/dN compared to FCP during Day 1. Portions of the Day 2 crack surface were nearly 100% intergranular.

Apart from severe temper embrittlement and abiotic sulfide additions, no chemical or mechanical variable has been previously reported to induce intergranular fatigue cracking in low to moderate strength quenched and tempered alloy steels[1].

SRB-Enhanced Fatigue Crack Initiation

The effect of environment on notch-tip fatigue crack initiation (FCI) in HY130 steel was measured at the beginning of each crack propagation experiment, and based on a fracture mechanics estimate of the local pseudo-elastic stress and total strain ranges[23,24]. SENT specimens for experiments in moist air, sterile NaCl, and SRB/Postgate C were similarly notched (with a root radius, ρ, of 0.25 mm and by grinding without additional polishing), and subjected to a constant ΔK of 20.8 MPa$\sqrt{m}$ (calculated as if the blunt notch was a crack of the same length) at a frequency of 1 Hz and R of 0.1.[h] After a period of no measurable crack formation, FCI progressed from the notch, as monitored by electrical potential measurements during cyclic loading.

The chloride environments affected FCI in tempered martensitic HY130 steel, as demonstrated in Fig. 6. This figure presents the number of load cycles required for FCI at constant $\Delta K/\sqrt{\rho}$, where a crack growth increment of 1 mm is employed to approximate the initiation stage of cracking. Results are given for FCI in moist air and three aqueous chloride environments. It is well known that, compared to fatigue in moist air, sterile NaCl degrades the

---

[h] This loading condition corresponds to a notch root pseudo-elastic stress range of 1315 MPa, calculated from $\Delta K/\sqrt{\rho}$[24], and to a proportional local plastic strain range that was not determined. Fatigue crack initiation is governed by plastic strain, however, the stress-based approach provides a basis for comparing environmental effects.

FCI resistance of C-Mn and alloy steels[23,24]. This environmental effect is severe for electrode potentials near free corrosion (-600 to -750 mV_{sce}), and is mitigated by applied cathodic potentials near -1000 mV_{sce}[26]. The detrimental effect of sterile NaCl at -600 mV_{sce} and the beneficial effect of applied cathodic polarization are reflected in Fig. 6; the result for HY130 steel in NaCl at -1000 mV_{sce} was measured in the current study and the free corrosion result was estimated based on data reported for a similar high strength steel loaded at a frequency of 0.2 Hz and R of 0.1[24]. For this latter case, FCI life may be higher for a loading frequency of 1 Hz.

Desulfovibrio vulgaris in Postgate C with cathodic polarization reduces the FCI resistance of HY130 steel relative to both moist air and sterile aqueous chloride at -1000 mV_{sce}. This result is technologically important because cathodic polarization is widely used to mitigate corrosion fatigue crack initiation in the steel/chloride system. SRB appear to reduce its effectiveness.

Comparing the SRB environment at -1000 mV_{sce} to sterile NaCl at free corrosion, the bacterial solution enhanced FCP in HY130 steel, but reduced FCI susceptibility. SRB-stimulated hydrogen embrittlement could contribute to the environmental effects on both crack initiation and propagation, as discussed in the next section. The aggressive character of the sterile solution at -600 mV_{sce} suggests an increased role of pitting-based FCI compared to SRB at -1000 mV_{sce}[25]. Pitting due to SRB-produced reduced sulfide species at -600 mV_{sce}, and the associated FCI life, have not been characterized. SRB may also degrade FCI resistance for freely corroding steels in bacterially active electrolytes with reduced near-electrode-surface alkalinity.

Mechanism for the SRB Effect on Environmental FCP

Hydrogen environment embrittlement (HEE) is an accepted mechanism to enhance FCP

in steels exposed to many gaseous and electrolytic environments near 25°C[1]. For sterile aqueous electrolytes, atomic hydrogen (H) forms on metal surfaces by cathodic reduction of hydrogen ions and water. That H which does not recombine to H_2 can enter the metal lattice, diffuse to the crack tip region, segregate at microstructural trap sites, and enhance fatigue damage as well as crack growth rate by one of several controversial mechanisms. The H source for crack tip embrittlement depends on environment chemistry[27]; the crack tip surface is dominant when occluded crack acidification occurs or when crack surface strain stimulates electrochemical reactions. H production on specimen surfaces that are boldly exposed to the bulk environment can be important for aggressive solutions, particularly those containing reduced sulfur species, and for prolonged exposures.

FCP rates are controlled by the kinetics of the slow step(s) in the sequence which produces and delivers embrittling H to the crack tip process zone[22]. An environmental factor (cathodic polarization, H_2S, decreasing loading frequency) which increases H uptake to the crack tip process zone is likely to increase FCP rates. For example, H_2S dissolved in chloride solution increases atomic H uptake by reducing the rate of atomic hydrogen recombination to H_2 and greatly enhances rates of FCP[2,9,28]. Scully and Moran demonstrated that this mechanism promotes H permeation in tempered martensitic 4340 steel, but only for acids (pH 3 or less)[29].

SRB may affect both atomic H production and uptake through metabolic action[30-32]. SRB generate energy by coupling the reduction of sulfate ions and the oxidation of a food source (often an organic molecule such as lactate)[13]. Bacterial sulfate reduction involves atomic hydrogen according to:

$$SO_4^{-2} + 8\,H \Rightarrow S^{-2} + 4\,H_2O \qquad [1]$$

The cathodic depolarization theory of SRB-influenced corrosion is based on the idea that bacterial utilization of H removes the cathodic product in the corrosion reaction couple and thus increases the open circuit corrosion rate of steel[15,33-35]. This effect lowers the amount of H available to enter the metal. Countering the potentially beneficial effect of the consumption of H in SRB metabolism, the production of sulfide or other metabolites may increase the uptake efficiency of H produced on the occluded crack tip or boldly exposed metal surfaces. Walch *et al.* have shown that hydrogen uptake into Pd and steel is enhanced in near-neutral solutions containing SRB[30,31]. The net effect of SRB on H production and environmental FCP depends on the relative strengths of these individual processes.

We speculate that the HEE mechanism describes the deleterious effect of SRB on da/dN in HY130 steel. Increased atomic hydrogen uptake and environmental cracking rates are caused by the metabolic production of sulfide overwhelming any beneficial effect of H consumption by the bacteria. In this regard, SRB play a role that is analogous to hydrogen recombination poisons[36]; promoting both H uptake efficiency and brittle cracking.[i] The observed intergranular FCP indicates that SRB-enhanced hydrogen production resulted in increased H partitioned to trap sites at prior austenite grain boundaries within the fracture process zone, compared to that from sterile chloride[37]. The fracture strength of the austenite grain boundaries must more strongly depend on local hydrogen concentration, compared to the behavior of coherent lath interfaces, in order to rationalize the transgranular to intergranular fatigue crack path transition. This

---

i Sulfide does not promote hydrogen uptake on unstrained, filmed steel surfaces in neutral to alkaline solutions[29], and therefore may not enhance da/dN for the cathodic polarization case where the crack tip is alkaline[38]. If cyclic plastic strain destabilizes a crack tip surface film, formed by reaction with high pH solution, then HS^- from SRB activity could promote hydrogen uptake at the crack tip.

speculation is unproven.

It is necessary to determine if SRB directly act at the crack tip, or on boldly exposed specimen surfaces, or if ions from SRB metabolism in the bulk solution migrate to such locations to enhance hydrogen uptake.

Transient FCP in the SRB Environment

The observation of long-term transient crack propagation, for HY130 steel only in the SRB solution, raises important issues for fatigue in bio-active environments. Here we open the discussion by examining possible origins of this phenomena. Since the SRB population grew during the fatigue experiment in the statically contained environment, da/dN could have increased at constant ΔK over a 24 hour period due to increased concentrations of metabolic sulfur species. The extent to which a solution concentration transient dominated the transient FCP was not measured. It is difficult to maintain bacterial solutions at constant activity, compared to typical environmental cracking experiments. Experiments must be developed to characterize the importance of biological environment chemistry changes.

Additional causes for time-dependent da/dN at constant ΔK can be assessed by diffusion calculations within the HEE framework. The effective diffusivity of hydrogen in HY130 steel (D_H) is 4×10^{-7} cm^2/sec[38], and the diffusivity of ions (D_I) in the electrolyte is 10^{-5} cm^2/sec[39]. For FCP in sterile NaCl (at free corrosion to modest cathodic polarization), transient crack propagation is not observed because the elements of the embrittlement process are localized at the crack tip. Crack solution transport, crack surface electrochemical reactions and crack tip

process zone H diffusion [j] are relatively fast; H diffusion from boldly exposed surfaces is not important[1,11,22,27]. If SRB rapidly migrate and populate the crack tip, then steady state FCP should result, similar to sterile NaCl. The observed long-term transient suggests that the SRB do not colonize surfaces, presumably because the occluded crack solution is alkaline for chloride at -1000 mV_{sce}[40]. This conclusion is contingent on a constant SRB population.

$HS^-/S^=$, produced by bacteria throughout the bulk solution and on specimen/chamber surfaces, could cause a FCP transient, however, ion diffusion times are relatively short. For example, if sulfur species are produced on or near boldly exposed notch surfaces, one hour is required for diffusion to the tip of a 4 mm deep fatigue crack. Since ion migration and convective mixing promote ion transport to the crack tip[40], this and shorter times are not consistent with the observed 24 hour transient FCP. Metabolite diffusion could limit FCP for transport distances on the order of 25 mm or larger. Remote SRB colony sites would be important if cathodic polarization reduced SRB metabolism on and near the steel specimen due to local alkalinity. For the current experiments with low cathodic current density and buffered Postgate C, only solution within hundreds of microns of specimen surfaces should be sufficiently alkaline to hinder SRB metabolism.

Finally, sulfur metabolites may stimulate H production on boldly exposed steel surfaces with subsequent diffusion to the crack tip process zone. From diffusion calculations (footnote j), 11 hours are required for H to diffuse through the steel over a distance equal to one-half of the single edge crack specimen thickness. This "lag time" for hydrogen supply is consistent with

---

j The distance (x) for hydrogen diffusion from the crack tip surface to the point of maximum stress within the process zone is of order 5 μm (K = 25 MPa√m, σ_{ys} = 1040 MPa and elastic modulus (E) = 200 GPa)[1,11]. Hydrogen will penetrate to a level of 95% of the surface concentration in a time (t) of 0.2 seconds ($x = 2(D_H t)^{1/2}$).

the transient cracking response of HY130 steel in SRB solution, but not with the observed crack profiles. Similar crack front shapes were observed for HY130 in sterile NaCl and SRB at -1000 mV_{sce}. The environmental fatigue cracks did not preferentially advance near specimen surfaces compared to crack penetration at the specimen midplane. Such inverse crack tunnelling is likely when boldly exposed surface hydrogen uptake is substantial relative to the crack tip[27]. Additionally, Austin and Walker report equal rates of FCP for bare and painted fracture mechanics specimens of a C-Mn steel loaded cyclically in gaseous H_2S doped seawater[2,10]. This result suggests that sulfide enhances crack tip H production, while hydrogen from boldly exposed specimen surfaces is not important.

The question of whether organic molecules from the Postgate medium adsorb on metal surfaces to hinder H production and uptake is important[10]. The concentration of dissolved H_2S in solution provides a means of assessing SRB activity and an indication of HEE severity. Media cultured SRB such as *Desulfovibrio vulgaris* produce on the order of 500 to 2000 ppm H_2S[10]. Thomas and coworkers reported that FCP rates in a C-Mn steel, exposed to 200 and 600 ppm H_2S dissolved from the gas, were increased by factors of 20 and 100 respectively compared to da/dN for pure seawater[2,10]. These enhancement factors were only 10 and 15 for similar levels of dissolved H_2S, produced by SRB from algae decomposition in seawater. These results indicate that the biological environment produced substantial sulfide species, but interfered with hydrogen uptake compared to abiotic H_2S. The inhibiting behavior of Postgate C is uncharted.

CONCLUSIONS

1. Sulfate reducing bacteria, *Desulfovibrio vulgaris* in diluted Postgate C, greatly enhance

rates of fatigue crack propagation and reduce fatigue crack initiation life in a martensitic alloy steel (HY130) under cathodic polarization (-1000 mV_{sce}). Metabolic sulfide-enhanced atomic hydrogen uptake and crack tip process zone hydrogen embrittlement are implicated.

2. Transgranular cracking, typical of fatigue in sterile NaCl solution, changes to intergranular cracking due to the presence of SRB.

3. The severity of the SRB effect on growth rates and intergranular cracking is paramount among those variables which influence environmental fatigue in C-Mn and alloy steels.

4. The deleterious SRB effects on fatigue crack propagation, and fatigue crack initiation, are not mitigated by cathodic polarization.

5. Transient environmental FCP in the SRB solution is likely due to time-dependent bacterial growth and enhanced metabolically reduced sulfides. Transient FCP at constant ΔK may also be due to diffusion of metabolites from the bulk to the crack tip solution, and hydrogen penetration from boldly exposed specimen surfaces. SRB may not colonize the occluded alkaline crack tip.

6. Transient fatigue cracking in SRB solutions can compromise life prediction based on stress intensity similitude.

ACKNOWLEDGEMENTS

This research was financially supported by the Virginia Center for Innovative Technology TDC on Electrochemical Science and Engineering (Grant CIT-TDC-88-01) and by the Office of Naval Research (Grant N00014-91-J-4164 monitored by A.J. Sedriks). The experiments were conducted by R. Krishnamurthy and S. Huettner.

REFERENCES

1. R.P. Gangloff, in Environment Induced Cracking of Metals, R.P. Gangloff and M.B. Ives, eds., NACE, Houston, TX, p. 55 (1990).

2. I.M. Austin and E.F. Walker, in Fatigue 84, C.J. Beevers, ed., EMAS, West Midlands, UK, p. 1457 (1984).

3. T.W. Thorpe, P.M. Scott, A. Rance and D. Silvester, Intl. J. Fat., Vol. 5, p. 123 (1983).

4. R.P Gangloff, in Corrosion Prevention and Control, 33rd Sagamore Army Materials Research Conference, M. Levy and S. Isserow, eds., US Army Laboratory Command, Watertown, MA, p. 64 (1986).

5. "Microbiologically Influenced Corrosion: A State-of-the-Art Review", MTI Publication No. 13, Materials Technology Institute of the Chemical Process Industries, Second Edition, NACE, Houston, TX (1989).

6. F. Mansfeld and B. Little, Corr. Sci., Vol. 32, p. 247 (1991).

7. W.A. Hamilton, Ann. Rev. Microbiol., Vol. 39, p. 195 (1985).

8. C.J. Thomas, R.G.J. Edyvean and R. Brook, Biofouling, Vol. 1, p. 65 (1988).

9. M.J. Cowling and R.J. Appleton, in Proc. Inst. Mech. Engrs. Conf on Fatigue and Crack Growth in Offshore Structures, Inst. Mech. Engrs., London, p. 77 (1986).

10. R.G.J. Edyvean, C.J. Thomas, R. Brook and I.M. Austen, in Biologically Induced Corrosion, S.C. Dexter, ed., NACE, Houston, TX, p. 254 (1986).

11. R. Krishnamurthy, "Microstructure and Yield Strength Effects on Hydrogen Environment Fatigue of Steels", PhD Dissertation, University of Virginia, Charlottesville, VA (1991).

12. I.P. Pankhania, Biofouling, Vol. 1, p. 27 (1988).

13. J.R. Postgate, The Sulfate Reducing Bacteria, Cambridge University Press, Cambridge, England (1979).

14. J. Horvath, M. Novak, Corros. Sci., Vol. 4, p. 159 (1964).

15. G.H. Booth, L. Eford, D.S. Wakerley, Brit. Corr. J., Vol. 11, p. 105 (1976).

16. D.J. Duquette and R.E. Ricker, in Biologically Induced Corrosion, S.C. Dexter, ed., NACE, Houston, TX, p. 121 (1986).

17. R. Krishnamurthy, C.N. Marzinsky and R.P. Gangloff, in Hydrogen Effects on Material Behavior, N.R. Moody and A.W. Thompson, eds., TMS-AIME, Warrendale, PA, p. 891 (1990).

18. O. Vosikovsky, J. Test. Eval., Vol. 6, p. 175 (1978).

19. T.W. Crooker, J.A. Hauser and R.A. Bayles, in Environmental Degradation of Engineering Materials III, M.R. Louthan, Jr., R.P. McNitt and R.D. Sisson, Jr., eds., Pennsylvania State University, University Park, PA, p. 521 (1987).

20. P.L. Andresen, R.P. Gangloff, L.F. Coffin and F.P. Ford, in Fatigue 87, Vol. III-A, R.O. Ritchie and E.A. Starke, Jr., eds., EMAS, West Midlands, UK, p. 1723 (1987).

21. P.C. Paris, M.P. Gomez and W.E. Anderson, The Trend in Engineering, Washington State Univ., Vol. 13, No. 1, p. 9 (1961).

22. R.P. Wei and R.P. Gangloff, in Fracture Mechanics: Perspectives and Directions, ASTM STP 1020, R.P. Wei and R.P. Gangloff, eds., ASTM, Philadelphia, Pa, p. 233 (1989).

23. S.S. Rajpathak and W.H. Hartt, in Environmentally Assisted Cracking: Science and Engineering, ASTM STP 1049, W.B. Lisagor, T.W. Crooker and B.N. Leis, eds., ASTM, Philadelphia, PA, p. 425 (1990).

24. S.R. Novak, in Corrosion Fatigue: Mechanics, Metallurgy, Electrochemistry and Engineering, ASTM STP 801, T.W. Crooker and B.N. Leis, eds., ASTM, Philadelphia, PA, p. 26 (1983).

25. R.A. Cottis and A. Markfield, in Fatigue 87, R.O. Ritchie and E.A. Starke, Jr., eds., EMAS, West Midlands, UK, p. 587 (1987).

26. H.H. Lee and H.H. Uhlig, Met. Trans., Vol. 3, p. 2949 (1972).

27. A. Turnbull, Scripta Metall., Vol. 20, p. 365 (1986).

28. R.N. Iyer, I. Takeuchi, M. Zamanzadeh and H.W. Pickering, Corrosion, Vol. 46, p. 460 (1990).

29. J.R. Scully, Unpublished research, University of Virginia, Charlottesville, VA (1993).

30. M. Walch and R. Mitchell, in Biologically Induced Corrosion, S.C. Dexter, ed., NACE, Houston, TX, p. 201 (1986).

31. M. Walch, T.E. Ford and R. Mitchell, Corrosion, Vol. 45, p. 705 (1989).

32. T.E. Ford and R. Mitchell, "Hydrogen Embrittlement: A Microbiological Perspective", Corrosion 89, Paper No. 189, NACE, Houston, TX (1989).

33. C.A.H. von Wolzogen Kuhr, Corrosion, Vol. 17, p. 293t, (1961).

34. W.P. Iverson, Nature, Vol. 217, p. 1265 (1968).

35. G.H. Booth, A.K. Tiller, Corros. Sci., Vol. 8, p. 583 (1968).

36. R.D. McCright, in Stress Corrosion Cracking and Hydrogen Embrittlement of Iron Base Alloys, R.W. Staehle, J. Hochmann, R.D. McCright and J.E. Slater, eds., NACE, Houston, TX, p. 306, 1977.

37. M. Gao and R.P. Wei, Metall. Trans. A, Vol. 16A, p. 2039 (1985).

38. J.R. Scully and P.J. Moran, in Environmentally Assisted Cracking, ASTM STP 1049, W.B. Lisagor, T.W. Crooker and B.N. Leis, eds., ASTM, Philadelphia, PA, p. 5 (1990).

39. J. Newman, Electrochemical Systems, Prentice-Hall, Inc, Englewood Cliffs, NJ, p. 230 (1973).

40. A. Turnbull and D.H. Ferriss, Corr. Sci., Vol. 27, p. 1323 (1987).

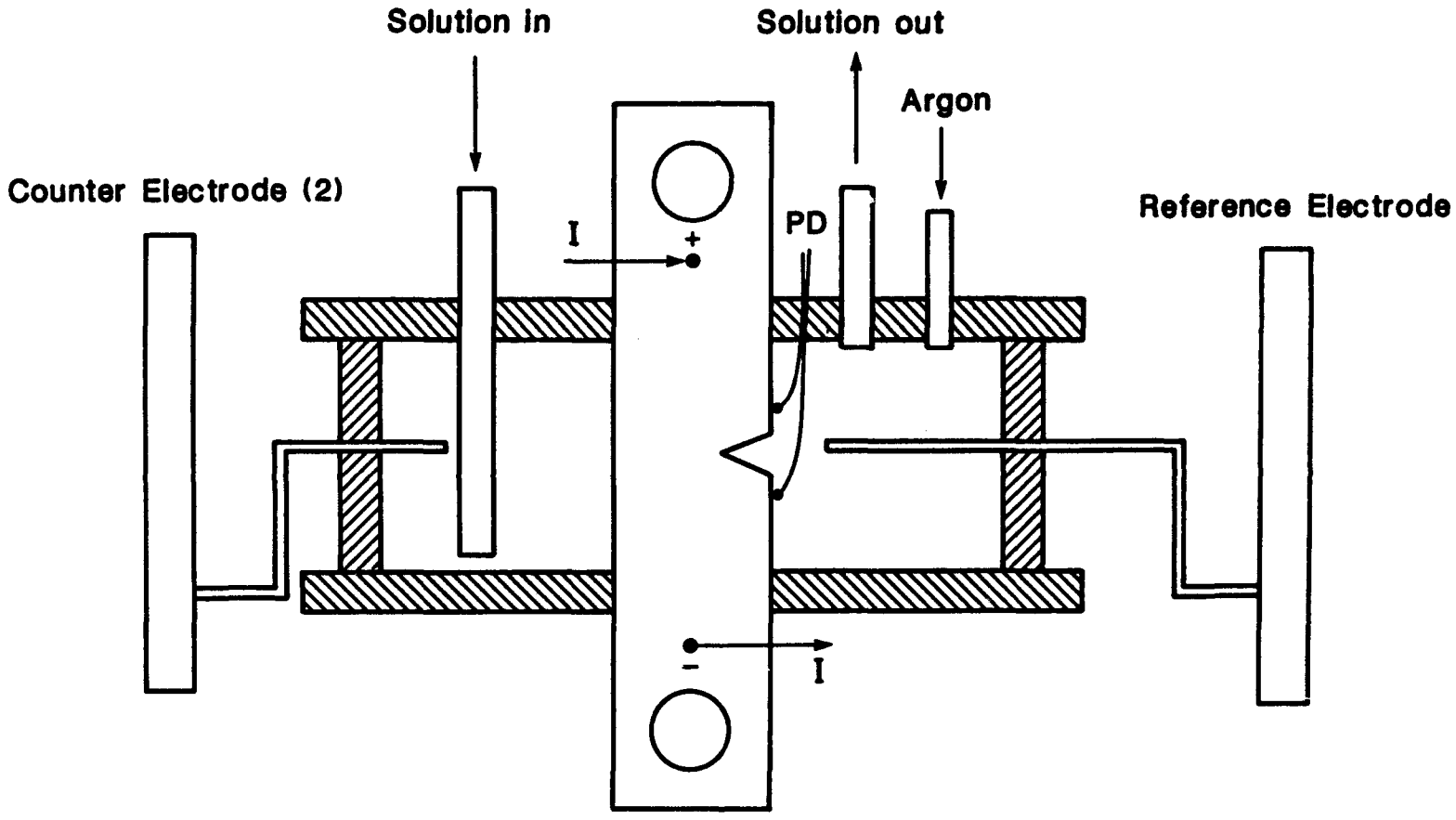

Figure 1 Environmental cell for fatigue cracking experimentation. "PD" indicates the location of probes for measuring electrical potential difference due to passage of a direct current, I, through the uncracked portion of the specimen.

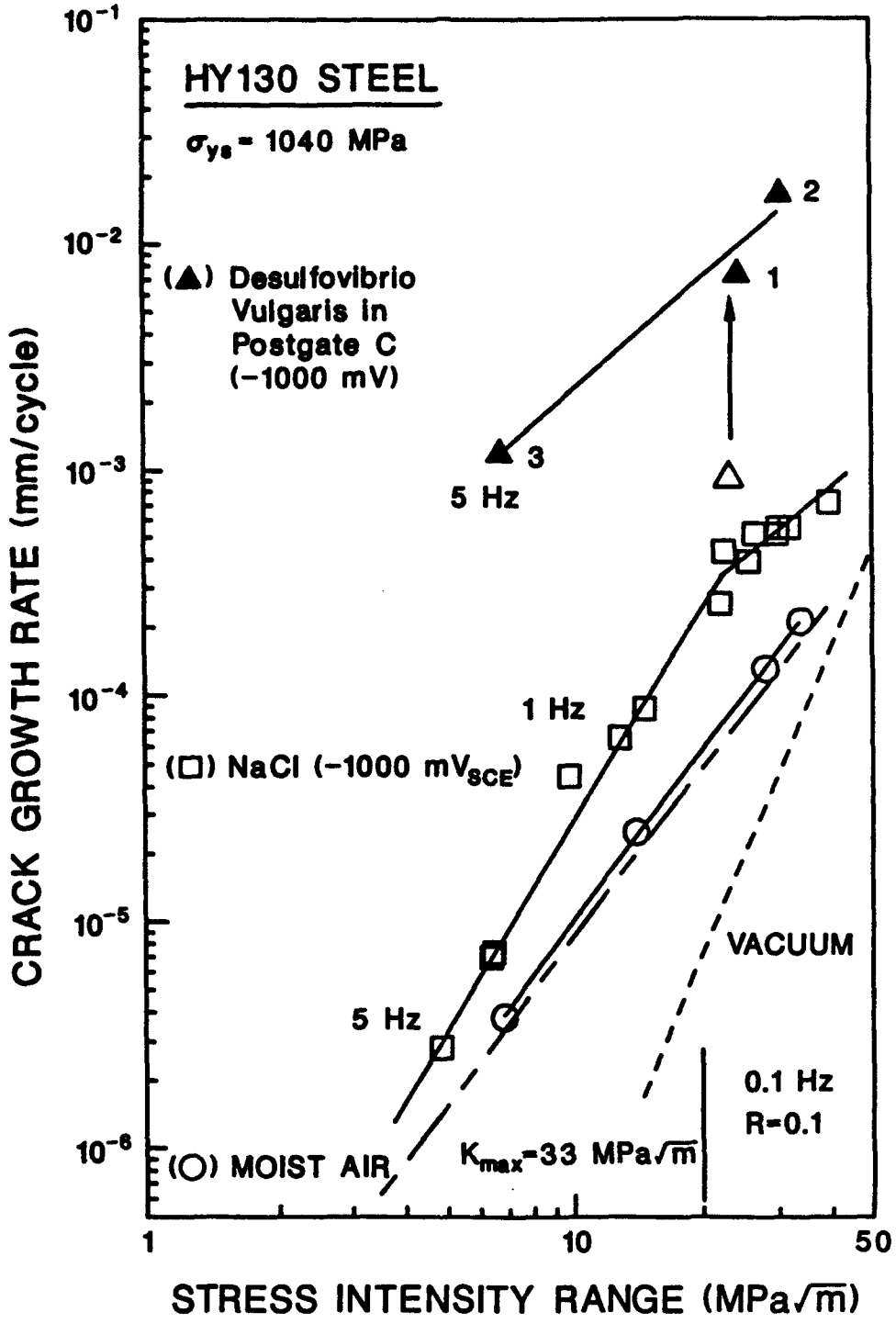

Figure 2 Fatigue crack growth rate versus applied ΔK for tempered martensitic HY130 steel in vacuum[11], moist air, sterile NaCl (-1000 mV_{sce}) and SRB/Postgate C at -1000 mV_{sce}. Stress ratio and frequency were varied as shown. The arrow indicates transient crack growth at constant ΔK and during the approach to steady state in the bacterial solution.

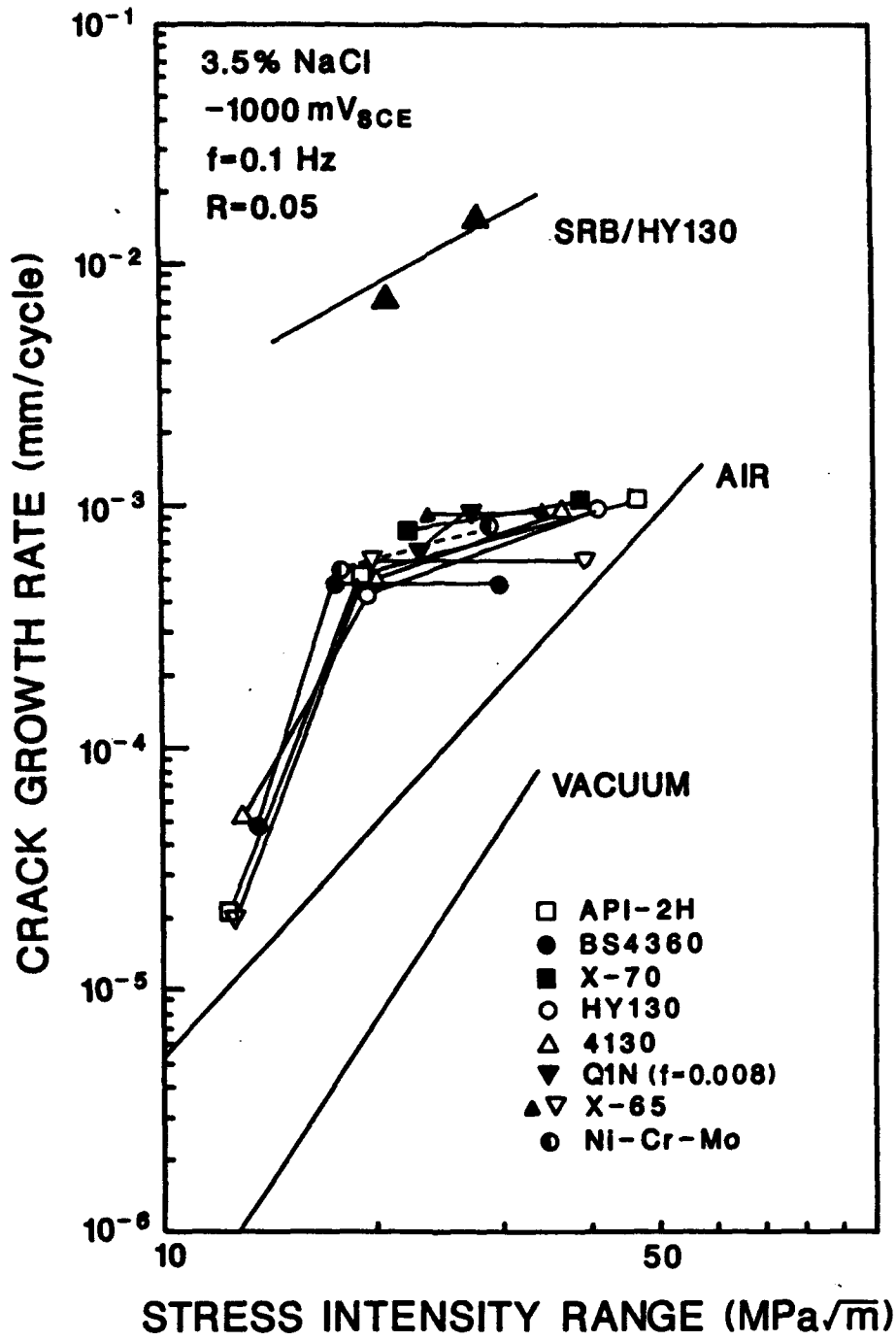

Figure 3 Environmental FCP in C-Mn and alloy steels exposed to sterile NaCl and bacterially active solutions at -1000 mV_{sce}, fixed loading frequency (0.1 Hz), and constant R (0.05)[1].

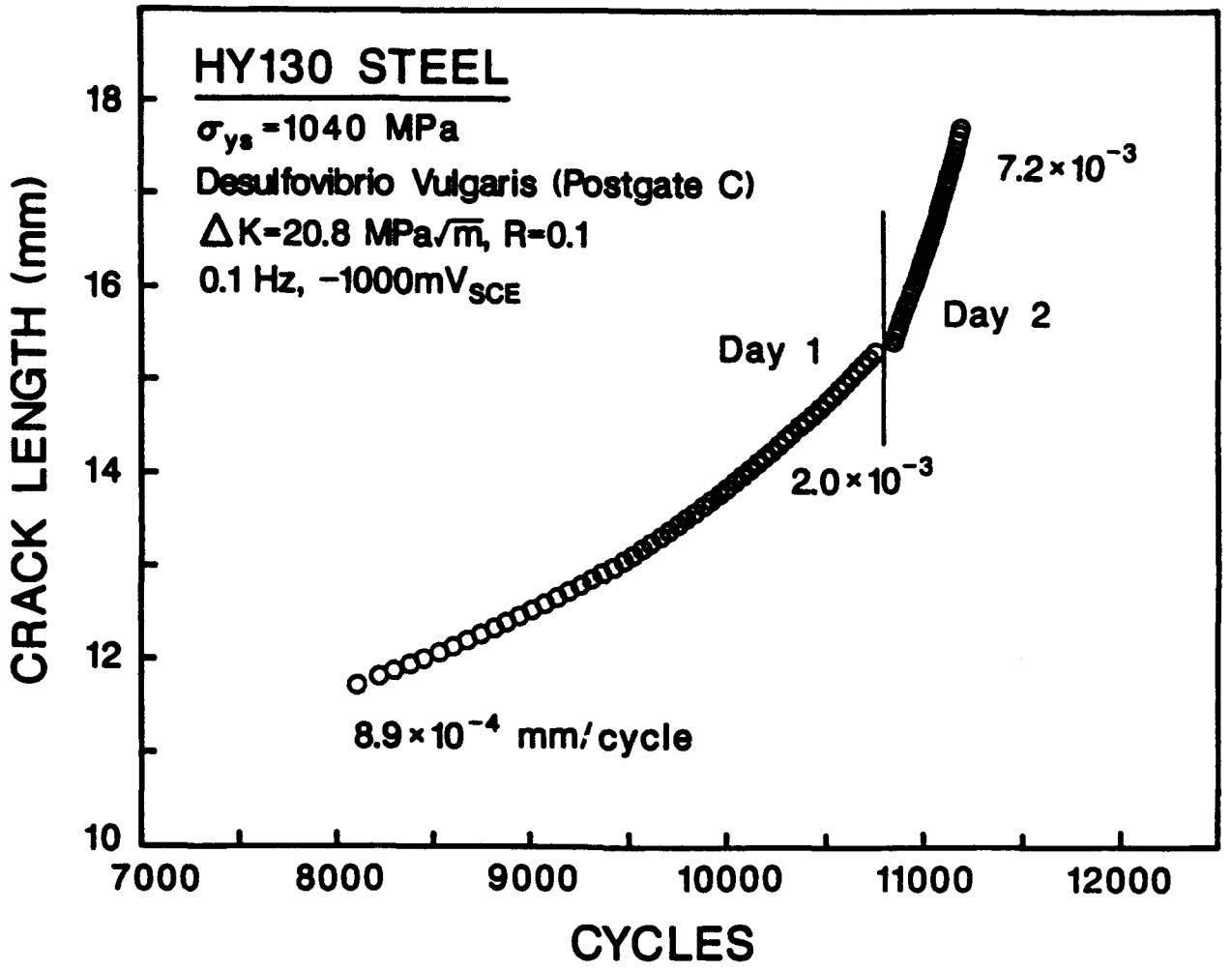

Figure 4 Fatigue crack length versus loading cycles for tempered martensitic HY130 steel in SRB/Postgate C at -1000 mV_{sce}, constant ΔK (20.8 MPa/m), frequency (0.1 Hz) and stress ratio (0.1).

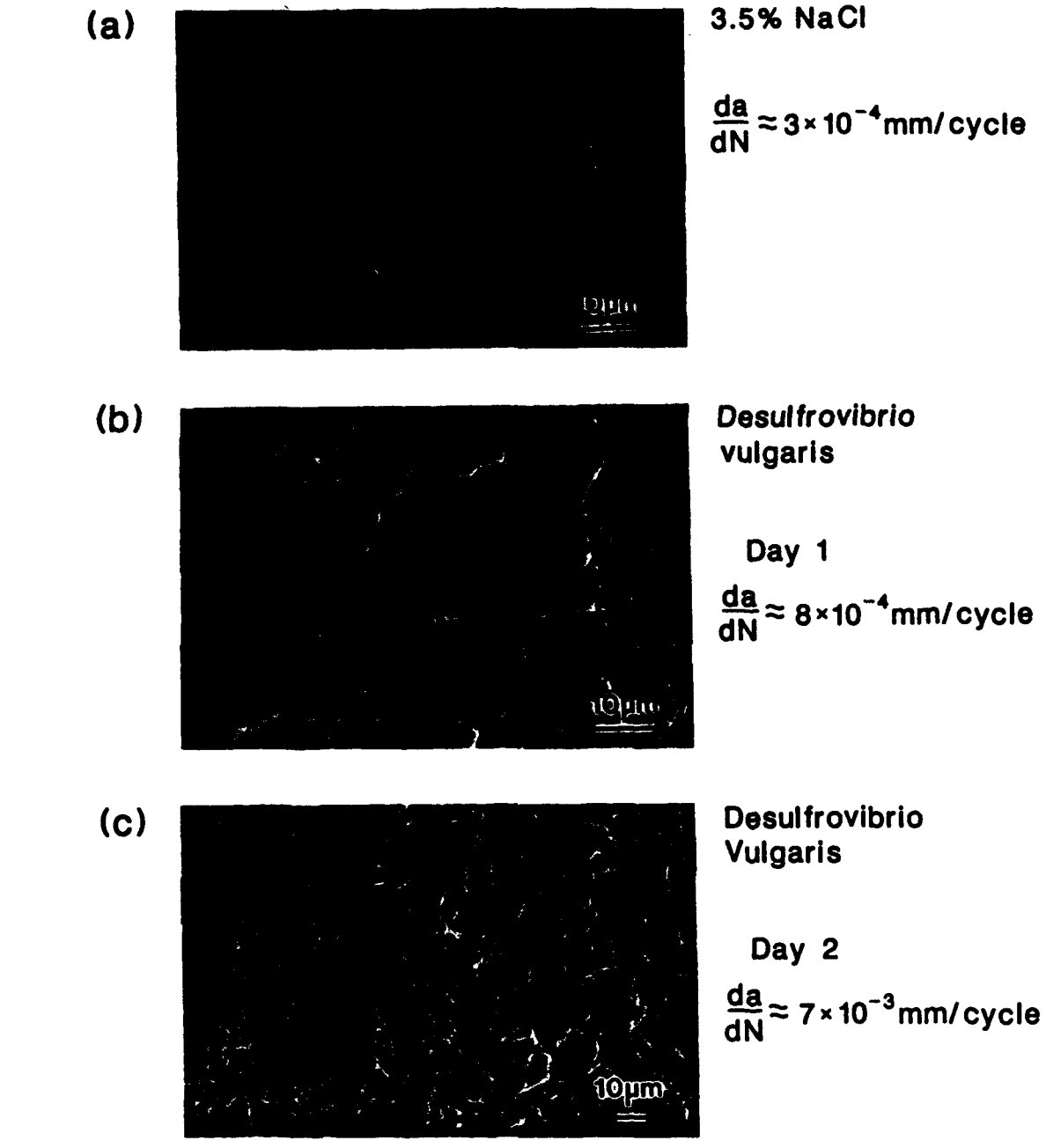

Figure 5 SEM fractographs of high ΔK FCP in HY130 exposed to sterile chloride and SRB solutions, each at -1000 mV_{sce} (ΔK = 20.8 MPa√m, R = 0.1 and f = 0.1 Hz). The crack growth direction is from top to bottom and the crack front is parallel to the horizontal direction.

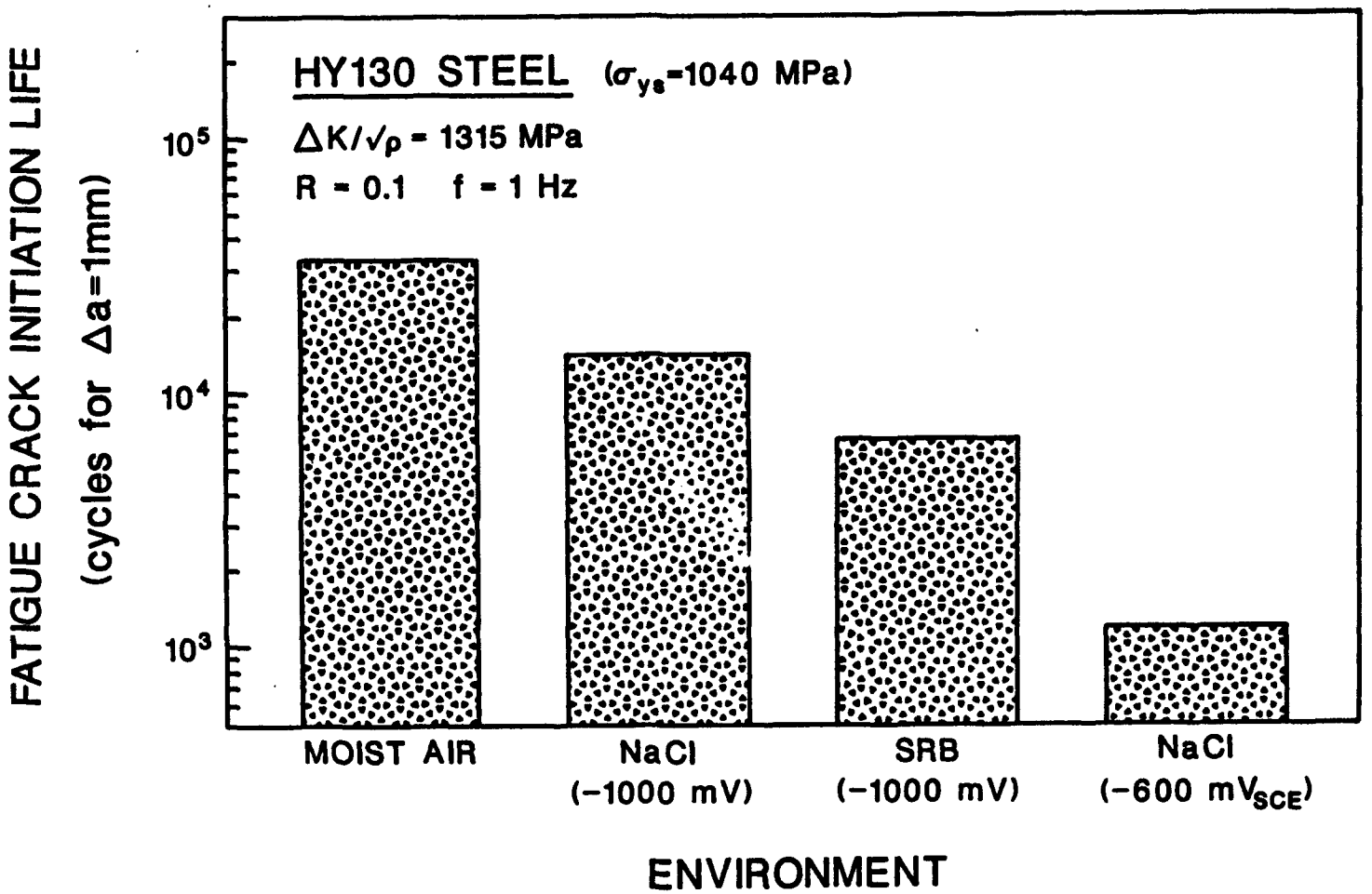

Figure 6 Fatigue crack initiation life (ΔN for 1 mm of crack extension from a notch tip) as a function of environment for HY130 steel at constant loading conditions ($\Delta K/\sqrt{\rho}$ = 1315 MPa, R = 0.1 and f = 1 Hz). The free corrosion result (-600 mV_{SCE}) was reported for similar martensitic steels at a frequency of 0.2 Hz[1,24].

AQUEOUS ENVIRONMENT-ENHANCED CRACK PROPAGATION IN HIGH STRENGTH BETA TITANIUM ALLOYS

Lisa M. Young
George A. Young, Jr.
John R. Scully
Richard P. Gangloff

Submitted for Publication in Metallurgical Transactions

AQUEOUS ENVIRONMENT-ENHANCED CRACK PROPAGATION IN HIGH STRENGTH BETA TITANIUM ALLOYS

Lisa M. Young[1], George A. Young, Jr.[2], John R. Scully[3] and Richard P. Gangloff[3]

[1] General Electric Corporate Research and Development
Schenectady, NY 12301

[2] Martin Marietta Knolls Atomic Power Laboratory
Schenectady, NY 12301

[3] Department of Materials Science and Engineering
School of Engineering and Applied Science
University of Virginia
Charlottesville, VA 22903-2442

ABSTRACT

The environment assisted cracking (EAC) behavior of two peak aged β-titanium alloys was characterized by a rising-load fracture mechanics method. STA Beta-21S is susceptible to EAC under rising load in neutral aqueous 3.5% NaCl at 25°C and -600 mV_{SCE}, as indicated by a reduced threshold for subcritical crack growth (K_{TH}) and fully intergranular fracture. In contrast the initiation toughness (K_{ICI}) of STA Ti-15-3 in moist air is lower than that of Beta-21S at similar high σ_{YS} (1300 MPa), but is unaffected by chloride and cracking is by transgranular microvoiding. The EAC susceptibility of STA Beta-21S correlates with preferential precipitation of α colonies at β grain boundaries, and/or with heterogeneous planar slip. Both features, and EAC, are promoted by prolonged solution treatment at high temperature. Based on hydrogen environment embrittlement, crack tip H could be transported by planar slip bands to irreversible trap sites and stress/strain concentrations at α-colony or β grain boundaries. Chloride EAC in Beta-21S is eliminated by cathodic polarization (-1000 mV_{SCE}) and by static loading for times which produce rising-load EAC. The beneficial effects of cathodic polarization and slow crack tip strain rate could relate to reduced H production at the occluded crack tip for the former, and to increased crack tip passive film stability or reduced dislocation transport for the latter. STA β-titanium alloys are resistant, but not intrinsically immune to chloride EAC; thermomechanical processing must be controlled for cracking resistance.

INTRODUCTION

Metastable beta titanium alloys are being developed for high performance applications that require formability, hardenability, fracture toughness, and aqueous corrosion resistance[1-4]. The environment assisted cracking (EAC) behavior of these alloys is of particular importance for long life components stressed in aggressive marine, oil or gas well, and medical implant environments[5,6]. While the stress corrosion cracking, hydrogen embrittlement and corrosion fatigue of α and α/β-titanium alloys have been extensively researched[7-11], EAC in modern β-titanium alloys is relatively unexplored.

Solution treated and aged (STA) β-titanium alloys exhibit excellent yield strength (σ_{YS}) and fracture toughness (K_{IC}), but are susceptible to brittle environmentally assisted cracking in ambient temperature aqueous solutions containing halide ions[10]. The EAC resistance is, however, apparently higher than that of high strength steels and α/β-titanium alloys, where the hexagonal phase is dominant and continuous[10]. Early experiments utilizing cracked fracture mechanics specimens demonstrated that developmental β-titanium alloys (Ti-11.5Mo-6Zr-4.5Sn and Ti-13V-11Cr-3Al; both STA)[1] and model Ti-Mo compositions were prone to EAC in NaCl and KCl solutions at static or quasi-static load threshold stress intensities (K_{ISCC}) as low as 15% of K_{IC}[8,13-15]. EAC in these high strength β-titanium alloys progressed by both intergranular separation and transgranular cleavage or "quasi-cleavage", depending on the alloy composition and microstructure[7,11,13]. EAC was exacerbated at intermediate loading rates (crack tip strain rates), at intermediate applied electrochemical potentials (near -600 mV_{SCE}), and by increased σ_{YS}[8,14-16].

Studies of EAC in modern STA β-titanium alloys, employing a slow strain rate technique with smooth uniaxially loaded tensile specimens, generally demonstrate excellent resistance to brittle cracking in aqueous NaCl at 25°C and near free corrosion potentials[12,17-22]. For example, high strength Ti-3Al-8V-6Cr-4Mo-4Zr (Beta-C™) was not susceptible to EAC in neutral chloride, with or without cathodic polarization; such conditions severely cracked α/β Ti-6Al-4V[20,21]. Similar

---

[1] All compositions are in weight percent.

good EAC resistance was reported for STA Ti-15Mo-3Nb-3Al (Beta-21S or TIMETAL-21S™)[22], however, high strength Ti-15V-3Cr-3Al-3Sn (Ti-15-3) was susceptible to brittle cracking in neutral aqueous chloride, but only at intermediate loading rates and electrode potentials[17]. (The average smooth specimen gauge strain rate for maximum susceptibility to EAC was about 5×10^{-6} sec^{-1} and the most deleterious electrode potential was -500 mV_{SCE}.) While immune to cracking in neutral chloride at 25°C, EAC was produced in Beta-C upon H_2S addition and with cathodic polarization[23], upon increased temperature to above about 150°C[18], in an anhydrous methanol-chloride environment[19], and after STA[23]. Fracture mechanics experiments which characterize the EAC behavior of modern β-titanium alloys are limited; recent results suggest that Ti-15-3 resists crack growth in chloride for mechanical and electrochemical conditions that embrittle Ti-6Al-4V[24].

The objective of this research is to characterize the environment assisted crack propagation behavior of two high strength β-titanium alloys in aqueous chloride. Experiments are designed to control the factors that may exacerbate EAC based on studies of high strength steels and α/β-titanium alloys. Specific factors include: (a) a fatigue precrack and triaxial constraint,[25] (b) dynamic crack tip straining,[26] (c) high yield strength,[27] (d) controlled electrode potential,[14,15] and (e) heterogeneous α/β microstructures[15,28]. These results are a necessary first step to understand the contributions of crack tip depassivation, transient dissolution and hydrogen uptake in the environmental cracking mechanism of β-titanium alloys. Preliminary data were presented elsewhere[29].

EXPERIMENTAL PROCEDURE

Materials

Two alloys, Beta-21S (Ti-15.4Mo-3.0Nb-2.9Al-0.13 O; measured wt%) and Ti-15-3 (Ti-14.9V-3.0Cr-3.2Al-3.6Sn-0.12 O; measured wt%), were obtained as 10.2 and 9.5 mm thick hot cross-rolled plates, respectively, in a solution treated condition (871°C for 8 hours and 816°C for 30 minutes, respectively). Oversized blanks of each alloy were peak aged at 538°C for 8 hours before specimen machining. (This

condition is referred to as STA.) The resulting microstructures are similar, consisting of a large volume fraction of fine intragranular and grain boundary α-plate precipitates in a β matrix of 100 μm diameter grains (Fig. 1). Figures 1b and 1c suggest that α plates are coarser in Ti-15-3 compared to Beta-21S. While not evident in Fig. 1, these two alloys exhibit dramatically different grain boundary α precipitation, as detailed in an ensuing section. X-ray diffraction and transmission electron microscopy (TEM) did not resolve the ω -phase in solution treated or peak aged Ti-15-3 or Beta-21S[30,31]. Athermal ω-phase is not expected to form in highly β-stabilized Ti-15-3 or Beta-21S, upon cooling from solution treatment temperatures, and isothermal ω should not precipitate prior to α nucleation during subsequent peak aging of either alloy at the relatively high temperature of 538°C[32-35].

Uniaxial tensile data are listed in Table I. The strength of Ti-15-3 is variable, as confirmed by hardness (Rockwell C scale; R_C) and tensile yield strength (σ_{YS}) measurements, and is generally less than that of Beta-21S. Based on the data in Table I, and additional results[36], the yield strength and hardness of Beta-21S and Ti-15-3 are related according to:

$$\sigma_{YS}\,(\text{MPa}) = -97.93 + 33.67\,(R_C) \qquad (1)$$

Equation 1 is in excellent agreement with a correlation for tempered martensitic steels[27].

Environmental Cracking

EAC resistance was characterized with a slowly rising load fracture mechanics method[37-39] applied to fully rotating single edge cracked specimens (initial crack length = 17.8 mm, thickness = 5.08 mm, width = 38.1 mm). A servohydraulic machine was employed for fatigue precracking (load control) and increasing load EAC experiments (actuator displacement control). Specimens were fatigue precracked in the aqueous environment, involving a three day exposure, and were then subjected to rising load at a constant actuator displacement rate.

Crack length was determined by a computer-automated direct current electric potential difference (dcEPD) method. Current polarity switching eliminated

Table I: ***Tensile Properties of STA β-Titanium Alloys***

Alloy	Test	R_c	σ_{YS}* (MPa)	E (GPa)	n**	RA*** (%)
Ti-15-3	1 2	35.7	1030 1050	94.2 93.3	0.036 0.037	21 28
Ti-15-3	1 2	39.4	1315 1315	96.6 97.7	0.032 0.031	13 14
Beta-21S	1 2	44.7	1420 1430	102.2 98.2	0.016 0.015	6 0
Beta-21S	1 2	43.8	1364 1352	103.2 101.8	0.018 0.018	2 1

* Tensile specimens were machined from the ends of broken fracture mechanics specimens.
** n is the exponent in the power-law relationship between true stress and true plastic strain.
*** RA = (Initial Diameter - Diameter at Fracture)/ Initial Diameter.

thermal voltages and reference probes were used to account for temperature and small current variations during long term experiments[36,40]. The applied current was typically maintained at 8.000 ± 0.005 amperes by a constant current power supply. Potential differences, local to the crack tip and between 200 and 500 μV, were amplified by 10,000 times and input to the data acquisition system. Crack length was calculated from averaged measured voltages through a closed form solution for the edge-cracked geometry derived by Johnson[36,40]. Potential difference resolution was ± 0.3 μV, corresponding to a crack length resolution of ± 5 μm assuming uniform advance of the crack front. Applied stress intensity (K) was calculated from measured load and crack length (a) with an elastic solution for the single edge crack geometry[41]. J-integral calculations indicate that the plastic contribution to J_{total} is small compared to $J_{elastic}$; thus small scale yielding is maintained and elastic K analysis is sufficient[36].

A schematic of the EAC procedure is presented in Fig. 2. The critical K for the onset (initiation) of crack growth is defined by the first change in the slope of the initially linear electrical potential versus load record, when coincident with

the onset of nonlinearity in the load versus actuator displacement record[36,42]. This critical K is a lower bound (K_{ICI}) of the standardized plane strain fracture toughness (K_{IC}) for loading in moist air[43], and is a time or loading rate dependent threshold (K_{TH}) for cracking in aggressive environments[37-39]. At initiation, the crack growth increment (Δa) is assumed to equal zero; subsequent crack lengths and Δa are calculated utilizing dcEPD values normalized with the potential at the known fatigue precrack length[36,40]. Environmental effects on crack propagation are indicated by the slope of the K-Δa data, and by subcritical crack growth rates (da/dt) calculated from measured crack length versus time.

Experiments were conducted in either moist air or neutral (pH 8) 0.6M (3.5 wt%) NaCl at fixed electrode potential and 25°C. The central portion of the edge cracked specimen was immersed in flowing (60 ml/min) chloride in a sealed plexiglass chamber. Environment control was complete; no dissimilar metal contacted the specimen, all tubing was teflon, and the electrolyte was argon deaerated. The specimen was maintained at constant electrode potential by a Wenking potentiostat in conjunction with a Ag/AgCl reference electrode and two platinum counter electrodes adjacent to each side of the specimen near the propagating crack. Reference and counter electrodes were isolated to minimize solution contamination. Electrode potentials are reported with respect to the saturated calomel electrode (mV_{SCE}).

RESULTS

Moist Air Fracture Toughness (K_{ICI})

Slow rising load experiments were performed at a single actuator displacement rate of 25.4 μm/min to obtain the moist air fracture toughnesses of STA Ti-15-3 and STA Beta-21S. As shown in Table II, fracture toughness decreases with increasing yield strength for each alloy; Beta-21S is generally tougher than Ti-15-3 at fixed σ_{YS}. K_{ICI} values in Table II are for plane strain constraint, based on ASTM Standard E813[44], and are slightly less than or equal to K_{IC} from ASTM Standard E399[43,45].

Fracture in moist air was predominantly transgranular for both STA Ti-15-3

Table II: ***Moist Air Fracture Toughness of STA β-Titanium Alloys****

Alloy/Test	σ_{YS} (MPa)	K_{ICI} (MPa$\sqrt{m}$)
Ti-15-3/#2	1040**	79
Ti-15-3/#1	1230	59
Ti-15-3/#3	1315	57
Beta-21S/#1	1285**	77
Beta-21S/#3	1330	66
Beta-21S/#2	1425	68

* The grip displacement rate for all experiments was 25.4 μm/min.
** These values are calculated from linear regression of yield strength versus hardness data.

and Beta-21S, as shown by the scanning electron microscope (SEM) fractographs in Fig. 3. The fatigue crack is at the top of each fractograph in Fig. 3 and the crack growth direction is from top to bottom, as is the orientation of all ensuing fractographs. The fracture process zone associated with the crack initiation toughness is on the order of 200 μm. Higher magnification microscopy revealed predominantly microvoided crack surfaces, with intermittent intergranular cracking and possible cleavage facets for each alloy, particularly Beta-21S.

Aqueous Chloride Environmental Cracking Resistance (K_{TH})

Constant Displacement Rate Experiments STA Ti-15-3 is resistant to EAC during rising load, as shown by the K-Δa curves in Fig. 4. For aqueous chloride at a fixed potential of -600 mV_{SCE}, K_{TH} (at Δa equalling zero) ranges from 61 to 64 MPa$\sqrt{m}$, independent of actuator displacement rates of 1.3 and 25.4 μm/min. NaCl does not decrease the crack initiation toughness from the moist

air K_{ICI} value of 59 MPa√m for a Ti-15-3 hardness of R_C 39.4 (σ_{YS} = 1230 MPa in Table II), or from K_{ICI} of 66 MPa√m estimated for a Ti-15-3 hardness of R_C 37.7[36]. Resistance to stable crack extension under plane strain constraint, given by a small but finite slope (dK/dΔa), is not influenced by the chloride solution. The difference in the slope of K versus Δa is larger for the replicate air experiments compared to the aqueous environmental effect. The variability in the initiation and growth resistances in Fig. 4 may be due to either σ_{YS} differences or subtle uncertainties in defining the electrical potential corresponding to crack initiation[36,42]. Crack tip plastic deformation, microvoid damage and macrocrack growth can each contribute to voltage increases.

Exposure to aqueous NaCl did not alter the microscopic fracture morphology for Ti-15-3 compared to loading in moist air. A typical scanning electron fractograph of the crack initiation region, adjacent to the fatigue precrack, is presented in Fig. 5 for Ti-15-3 in NaCl. As for the moist air case, the crack surface is mainly populated by transgranular features indicative of microvoid-based cracking, as confirmed by high magnification SEM observations (Fig. 5b).

In contrast to STA Ti-15-3, peak aged Beta-21S is embrittled by rising load in aqueous chloride, as shown by the K-Δa data in Fig. 6. While K_{ICI} is high for moist air (66 and 68 MPa√m, Table II), K_{TH} ranges from 39 to 46 MPa√m for STA Beta-21S in NaCl at -600 mV_{SCE} and two constant actuator displacement rates. The macroscopic crack growth resistances (average dK/dΔa) are similar for each loading rate in NaCl and for each environment. The data in Fig. 6 show that the two displacement rates were sufficiently high to offset stress intensity reductions due to increasing specimen compliance and declining load during environmental crack growth. Therefore, the rising load EAC experiments were of the increasing-K type.

Aqueous NaCl caused a dramatic fracture mode transition in STA Beta-21S. Compared to transgranular microvoid-based fracture for Beta-21S in moist air (Fig. 3b), Fig. 7 shows that EAC in chloride is almost entirely intergranular, with little evidence of resolvable localized plasticity. The initial stage of EAC, within 25 μm of the fatigue crack (top of Fig. 7), involved some transgranular cracking, similar

to that observed for moist air, while boundary cracking initiated immediately adjacent to the fatigue crack tip in other grains. Presumably, this distribution of modes is related to the location of the fatigue crack within the various grains along the crack front. Fatigue precracking at a loading frequency of 5 Hz and in aqueous NaCl did not produce intergranular cracking[36]. The transition from a transgranular and locally ductile fracture mode to intergranular cracking is consistent with the environmental effect on crack growth initiation resistance shown in Fig. 6.

It is interesting that the macroscopic crack paths and causal fracture mechanisms are markedly different for STA Beta-21S in moist air and NaCl, however, $dK/d\Delta a$ are similar. The resistance to stable tearing in benign environments ($dK/d\Delta a$) is determined by rate independent intrinsic material properties, including the process zone fracture strain and material flow properties[46]. In contrast $dK/d\Delta a$ during EAC is governed by the rate of environmental crack advance, dependent on alloy cracking resistance and environment chemistry, coupled with the applied crack mouth opening displacement rate and specimen compliance. Intuitively, the crack growth resistance slope should be less, or even negative, for EAC compared to the typical moist air R-curve, and could approach this latter value at rapid loading rates. This difference may be negligible for Beta-21S (Fig. 6) because crack growth resistance is small for the plane strain moist air case.

This study emphasized K_{TH} at the onset of environmental cracking, however, average rates of intergranular EAC (da/dt) were estimated. As indicated by the K-Δa data in Fig. 6, stable (subcritical) crack growth occurred in STA Beta-21S due to NaCl exposure and at K levels well below K_{ICI} for moist air. For an experiment at a displacement rate of 25.4 μm/min, intergranular EAC initiated at a K_{TH} of 39 MPa$\sqrt{m}$ and after 1220 seconds of steadily rising load; 2.0 mm of stable crack growth then occurred in 180 seconds, for an average crack growth rate of 10 μm/sec. (K increased from 39 to 50 MPa$\sqrt{m}$ during this amount of EAC at increasing load line displacement.) For the slower loading rate experiment in Fig. 6, intergranular EAC initiated at a K_{TH} of 46 MPa$\sqrt{m}$, after 4.8 hours of loading; subsequently, 2.0 mm of stable crack growth occurred in 1800 seconds, for an

average da/dt of 1 μm/sec. (K increased from 46 to 57 MPa√m during this amount of EAC.) Two discontinuous crack bursts, each 300 μm long, occurred at K levels between K_{TH} and K_{ICI} for the slowest loading rate NaCl experiment in Fig. 6. These burst distances and the average da/dt values are based on the assumption of uniform crack advance along the crack front, as required to analyze the dcEPD voltages.

Static Load Results Fatigue precracked specimens of STA Ti-15-3 and STA Beta-21S were statically loaded during immersion in NaCl at -600 mV_{SCE}. These experiments were performed at several constant K levels (35, 45, 55 and 60 MPa√m) for 24 hour intervals, while crack length was continuously monitored by dcEPD. Crack growth rate resolution over a 24 hour period was about 3×10^{-4} μm/sec. This exposure, while short compared to classic stress corrosion cracking experiments, is longer than the durations of the slow displacement rate experiments represented in Figs. 4 and 6 which required 0.5 or 10 hours. Additionally, a 24 hour hold-time would produce 17 meters of crack advance in an EAC sensitive alloy such as STA Ti-12Mo-6Zr-3Sn in aqueous chloride at about -600 mV_{SCE} [47].

Static loading for 24 hours did not generate resolvable environmental crack growth for either STA Ti-15-3 or Beta-21S in NaCl. In one instance NaCl-enhanced subcritical crack growth was produced in Beta-21S, but only after 94 hours at a K level of 60 MPa√m. The average crack growth rate increased from about 10^{-2} μm/sec to 20 μm/sec with time and crack length (from 20.2 mm to 22.2 mm) at this constant applied K.

Effect of Applied Electrode Potential The effect of applied electrode potential on EAC in the STA Ti-15-3 and Beta-21S/NaCl systems was investigated. In addition to -600 mV_{SCE}, potentials of -150 mV_{SCE} and -1000 mV_{SCE} were employed in conjunction with the rising load method. The free corrosion potential of these two β-titanium alloys in deaerated neutral 0.6M NaCl is between -500 and -600 mV_{SCE}.

Peak aged Ti-15-3 displayed no resolvable susceptibility to EAC in aqueous 3.5% NaCl at any of the applied electrode potentials and a constant displacement

rate of 1.3 μm/min. K_{TH} values were as follows: 66 MPa√m for -150 mV_{SCE} (R_C 37.0), 61 MPa√m for -600 mV_{SCE} (R_C 37.9), and greater than 65 MPa√m for -1000 mV_{SCE} (R_C 36.8)[2]. Measured K_{ICI} equals between 57 and 59 MPa√m for the R_C 39 to 40 hardness of Ti-15-3 in moist air, Fig. 4. Estimated K_{ICI} equals 65 MPa√m for the R_C 37.9 hardness of Ti-15-3 and 69 MPa√m for the R_C 36.8 moist air case[36]. For each electrode potential, the crack surface was transgranular, typical of that shown in Fig. 5 and indicative of ductile fracture without a chloride environmental effect.

Peak aged Beta-21S exhibited EAC at -150 mV_{SCE} (and -600 mV_{SCE}), but not at -1000 mV_{SCE}, as shown by the constant displacement rate (25.4 μm/min) K-Δa data in Fig. 8. Although K_{TH} was significantly reduced at -150 mV_{SCE}, crack growth resistance, dK/dΔa, was relatively high. The microscopic fracture mode for the -150 mV_{SCE} case, shown in Fig. 9a, consists of intergranular cracking joined by limited ductile tearing and supports an environmental effect. Some transgranular cracking was present adjacent to segments of the fatigue crack. These features are similar to those observed for the Beta-21S crack surface produced in NaCl at -600 mV_{SCE} (Fig. 6), a condition which also produced EAC. In contrast NaCl with an applied electrode potential of -1000 mV_{SCE} did not degrade fracture resistance relative to the behavior of Beta-21S in moist air. K_{TH} for this case equals K_{ICI} for Beta-21S in moist air, and the NaCl/cathodic polarization cracking mechanism is based on transgranular microvoid coalescence (Fig. 9b) similar to that observed for moist air (Fig. 3b).

DISCUSSION

Moist Air Fracture Toughness of STA β-Titanium Alloys

The moist air fracture toughnesses of STA Ti-15-3 (K_{ICI} = 57 to 59 MPa√m for σ_{YS} = 1230 to 1315 MPa; Table II) and STA Beta-21S (K_{ICI} = 66 to 68 MPa√m for σ_{YS} = 1330 to 1425 MPa) are comparable to values reported for β-titanium alloys at similar high yield strengths[28,48-51]. This result validates the accuracy of the

---

[2] A data acquisition system failure preempted the conclusion of the experiment at -1000 mV_{SCE}, however, stable crack growth had not initiated at an applied K of 65 MPa√m.

rising load experiment. Both Ti-15-3 and Beta-21S cracked by microvoid-based processes for the moist air case, however, each fracture morphology is complex because of the underlying two phase microstructure.

STA Beta-21S is tougher than Ti-15-3 at constant σ_{YS}, in spite of some grain boundary participation in ductile fracture. This result is notable because grain boundaries in the Beta-21S under study were preferred nucleation sites for colonies of α plates, as discussed in an ensuing section. (A similar result was reported for Ti-15-3 where heterogeneous grain boundary α precipitates were correlated with increased fracture toughness compared to a more homogeneous α microstructure[51].) A thin layer of grain boundary α, 0.1 to 0.2 μm thick was observed for both STA Beta-21S and STA Ti-15-3. Finally, Beta-21S may be more prone to localized planar slip than Ti-15-3[30]. Planar slip and a 1 to 10 μm thick grain boundary α "film" are reported to degrade K_{IC} due to strain localization in the soft α phase or precipitate-free β phase, relative to adjacent α-precipitation hardened β, as well as due to preferred microvoid nucleation at α/β interfaces[4,48-50]. This is apparently not the case for STA Beta-21S with colonies of α at grain boundaries. Additional factors such as the size, distribution, and strengths of α and β; solute (e.g., aluminum and oxygen) partitioning to each phase; and inclusion content may affect initiation fracture toughness.

Environmental Cracking Resistance of STA β-Titanium Alloys

The results in Figs. 4, 6 and 8 show that, while STA Ti-15-3 resists EAC in aqueous NaCl, peak aged Beta-21S is susceptible to severe intergranular environmental cracking in chloride at electrode potentials near or anodic to the free corrosion level. Table III compares the severity of EAC in β and α/β titanium alloys to that in quenched and tempered martensitic alloy steels, at similar strength levels and in aqueous NaCl at about -600 mV_{SCE}. For high σ_{YS} (1300 MPa), the EAC resistance of β Ti-15-3 is superior to that of a typical martensitic steel such as AISI 4340.

The σ_{YS}-K_{TH} properties of STA Ti-15-3 exceed the performance of mill annealed Ti-8-1-1; thermomechanical processing of this and other α/β alloys will not generally produce the high strengths achievable with STA β-titanium alloys, but can improve K_{ISCC}[52]. (K_{ISCC} equals about 60 MPa$\sqrt{m}$ for β-treated or α/β-treated

Table III: ***Fracture Resistance of High Strength Titanium Alloys and Martensitic Steels***

	Ti-15-3 (STA)	Beta-21S (STA)	Ti-8Al-1Mo-1V (Mill Anneal)[52]	HY130 Steel (Quench/Temper)	AISI 4340 Steel[27] (Quench/Temper)
σ_{YS} (MPa)	1300	1330	850	1025	1350
K_{IC} or K_{ICi} (MPa$\sqrt{m}$)	59	66	120	110*	90 to 100
K_{TH} or K_{ISCC} (MPa$\sqrt{m}$)	61 to 64	39 to 46	35	70*	25 (12 to 38)

* Measured by the methods employed in this study, but for 3.5% NaCl at -1000 mV_{SCE}. K_{TH} is between 70 and 100 MPa$\sqrt{m}$ for HY130 steel in chloride at -600 mV_{SCE}[27].

Ti-6Al-4V in aqueous NaCl.) HY130 steel is resistant to chloride EAC, by virtue of relatively low yield strength compared to 4340[27], and intrinsically compared to the α/β Ti alloy at a similar modest σ_{YS} of about 1000 MPa. K_{TH} results have not been reported for solution treated, single phase β-titanium alloys in aqueous chloride; since such alloys exhibit strengths similar to HY130 steel, high EAC resistance is expected unless slip localization[30,53] or dynamic plastic strain[27] prove to be detrimental.

Hydrogen Environment Embrittlement Mechanism Our working hypothesis is that EAC in the STA β-titanium/25°C aqueous chloride system is caused by crack tip hydrogen production, uptake, and process zone embrittlement; the so-called hydrogen environment embrittlement (HEE) mechanism[54-57]. For Ti alloys, the elements of HEE include: (1) anodic dissolution of Ti and the alloying elements to produce hydrolyzable cations which lower the crack tip solution pH[58,59], (2) dissolution-coupled hydrogen ion and water reduction reactions on bare Ti[58,59], (3) transient crack tip repassivation to reduce cathodic hydrogen production and to form a barrier film to atomic hydrogen (H) uptake, (4) film rupture by crack tip strain, (5) H transport within the crack tip process zone, by bulk diffusion and possibly grain boundary diffusion or dislocation transport, (6) H partitioning to microstructural trap sites, and (7) process zone embrittlement, possibly involving titanium hydride

formation in either the α or β phases, interface or lattice plane decohesion, as well as localized plasticity. Here, we qualitatively examine microstructure, loading rate and cathodic polarization effects on NaCl EAC of Beta-21S within the framework of HEE.

Effect of β-titanium Microstructure on EAC While many β-titanium alloys resist EAC, at least in modestly aggressive aqueous chloride solutions[10,12], it is necessary to determine the conditions which promoted intergranular cracking in peak aged Beta-21S.

Effect of Yield Strength on EAC: STA Beta-21S was stronger than STA Ti-15-3, with R_C varying between 41 and 45 for edge cracked specimens of the former alloy (Figs. 6 and 8), and between 36 and 38 for Ti-15-3 (Fig. 4). While K_{TH} decreases with increasing σ_{YS} for martensitic steels in NaCl[27], the data in Fig. 6 suggest similar K_{TH} for Beta-21S at hardness levels of R_C 41 and 45 (σ_{YS} of 1283 and 1417 MPa from Eq. 1). Solution treated (816°C for 30 minutes) specimens of Ti-15-3 were aged at 510°C for 14 hours to produce higher hardness (R_C 41 to 42) compared to the standard (538°C) 8 hour age. The moist air K_{ICi} for higher strength Ti-15-3 equalled 57.1 MPa√m, while K_{TH} for slow displacement rate (25.4 μm/min) loading in NaCl (-600 mV_{SCE}) equalled 50.7 MPa√m. The corresponding fracture modes were transgranular and dimpled for both air and NaCl, with a small amount of intergranular cracking for the latter. These results indicate that the EAC resistance of Ti-15-3 may decrease with increasing σ_{YS}; this trend should be defined for very high strength levels. This modest decline in K_{TH} with increasing σ_{YS} is not sufficient to explain the sensitivity of Beta-21S to intergranular EAC.

Effect of Solution Treatment Conditions on Microstructure: The contrasting chloride EAC resistance of STA Ti-15-3 versus the susceptibility of STA Beta-21S may be traced to either microstructural or slip mode differences derived from variations in thermo-mechanical processing and solution heat treatment. Optical microscopy, SEM and TEM of each alloy in the under[3] and peak aged conditions

---

[3] Specimens of solution treated Ti-15-3 and Beta-21S were under aged at 538°C for 1 hour to clarify the initial stage of α precipitation in the otherwise complex peak aged microstructures.

reveal extensive α precipitation at β grain boundaries in Beta-21S, but not in Ti-15-3. This behavior is clearly detailed by the underaged microstructures represented in parts a and c of Figs. 10 (optical) and 11 (SEM). For Ti-15-3 (Figs. 10a and 11a), relatively homogeneous α precipitation occurs within β grains after the short under aging time; large α plates only infrequently nucleate on or adjacent to β grain boundaries. In contrast for under aged Beta-21S, a large amount of α initially nucleates on or near β grain boundaries, and grows in a colony morphology toward grain interiors (Figs. 10c and 11c). Intragranular α precipitation is limited for under aged Beta-21S. While considerably more difficult to discern, peak aged Ti-15-3 exhibits homogeneously distributed α plates within β grains, with limited grain boundary α colonies (Fig. 1b). In contrast STA Beta-21S exhibits intragranular α plates and coarse grain boundary α colonies, as detailed elsewhere[36]. These peak aged microstructures are consistent with the likely further evolution of the structures shown in Figs. 10 and 11. Extensive grain boundary α colonies should not form in Ti-15-3, during longer time aging, given the extensive intragranular precipitation at short aging times.

Grain boundary microstructures are amplified by the TEM results in Fig. 12. Beta grain boundaries in under aged Ti-15-3 in fact contain a 0.1 μm thick layer of α (Fig. 12a). This boundary α does not substantially grow during additional aging to the peak strength condition, however, α plates separately nucleate and grow within grains (Fig. 12b). The micrograph in Fig. 12c for peak aged Beta-21S shows that an α layer is present at β grain boundaries, analogous to Ti-15-3, and suggests that colony α forms from this grain boundary α layer in Beta-21S. Colony α in Beta-21S is generally normal to the β grain boundary (FIg. 12c), while α plates near grain boundaries in Ti-15-3 appear at one or more varied angles typical of a crystallographic relationship with the β matrix (Fig. 12b). The colony morphology of α has not been widely reported, however, there is precedent for this microstructure[51].

Homogeneous intragranular α precipitation in β-titanium alloys is promoted by several factors including dislocation sites typical of partial recovery and recrystallization during hot working and solution treatment, post-solution treatment cold work, a supersaturation of vacancies quenched from solution

temperatures, lower aging temperatures, as well as by precursor ω or β' precipitates[28,32,34,35,51,60,61]. Athermal and "isothermal" ω can form in metastable β-titanium alloys during cooling after solution treatment[32,34,35], however, this phase was not observed by X-ray diffraction and TEM of either solution treated or STA Beta-21S and Ti-15-3. The correlation between the somewhat higher solution treatment temperature for STA Beta-21S and boundary α is not consistent with a simple argument based on vacancies. Perhaps the quenched in vacancy concentrations were similar for Ti-15-3 and Beta-21S, aged at 816°C and 871°C, respectively, and cooled at unknown rates. Additionally, vacancies influenced α precipitation at low aging temperatures, but not at the higher level (538°C) employed in the current work[61].

The difference in solution treatment conditions, 8 hours at 871°C for Beta-21S compared to 30 minutes at 816°C for Ti-15-3, causes grain boundary α-colony precipitation for the former alloy. To investigate this hypothesis, as-received Ti-15-3 was resolutionized at 1038°C for 2 hours[36] or at 950°C for 12 hours[30]. Metallographic analyses summarized in Figs. 10b and 11b reveal preferential α-colony precipitation at Ti-15-3 grain boundaries, for both solution treatments followed by under aging, similar to Beta-21S. These experiments confirm the importance of high solution treatment temperatures and longer times in promoting grain boundary α-colony precipitation after short aging times. This effect can be explained by heterogeneous α nucleation at dislocation substructure in preference to grain boundary sites. Higher solution treatment temperatures and longer times could promote recovery and recrystallization. Sites for heterogeneous α nucleation are then limited to grain boundaries; α precipitation within grains is less likely compared to the more homogeneous precipitation produced for a partially recovered and recrystallized microstructure. Once intragranular α forms, extensive grain boundary colony α precipitation is unlikely.

Effect of Solution Treatment and Microstructure on EAC: The hypothesized importance of solution treatment condition on EAC resistance is supported by the experimental observation that resolution treated and peak aged Ti-15-3 (1038°C for 2 hours; RSTA) is susceptible to EAC in NaCl, as demonstrated in Figs. 13 and 14. The moist air K_{ICI} for this case is higher (74 MPa$\sqrt{m}$ in Fig. 13) than that for

short-time low temperature STA Ti-15-3 (57 to 59 MPa√m in Fig. 4) at constant yield strength (R_C 39 ± 1). This result parallels the higher moist air fracture toughness of STA Beta-21S, including the point that fracture involved a modest amount of grain boundary cracking. K_{TH} for high temperature RSTA Ti-15-3 in NaCl (64 MPa√m) is less than the K_{ICI} value (74 MPa√m), in contrast to essentially equal K_{TH} and K_{ICI} for low temperature solution treated and peak aged Ti-15-3 (Fig. 4). As shown in Fig. 14, EAC of RSTA Ti-15-3 is more intergranular compared to both transgranular cracking of the lower temperature solution treatment condition in NaCl (Fig. 5), and transgranular/intergranular cracking of RSTA Ti-15-3 in air[36]. STA Beta-21S is more susceptible to EAC in NaCl compared to RSTA Ti-15-3.

Intergranular EAC in STA Beta-21S, and to a lesser extent in RSTA Ti-15-3, may be traced to one or both of two microstructural features which are similarly produced by higher temperature-long time solution treatment; that is, α precipitate colonies at β grain boundaries and highly localized planar slip. Given the metallographic results in Figs. 10 through 12, as well as the EAC results in Figs. 13 and 14, intergranular EAC could be due to grain boundary α. Considering grain boundary microstructure, both Beta-21S and Ti-15-3 exhibit a similar 0.1 μm thick layer of boundary α which could hydride due to the low solubility of H in this phase relative to β[4,8,62]. This grain boundary microstructure similarity does not explain the observed difference in EAC resistance. The prominent α colonies, unique to grain boundaries in STA Beta-21S and RSTA Ti-15-3, could hydride and promote EAC, particularly if crack tip potential and occluded solution acidification by hydrolysis promote hydrogen entry. There is no fractographic evidence that this happened. The intergranular facets shown in Fig. 7 seem to be free of the microscopic detail which would be expected if EAC progressed though hydrided α colonies. (One explanation for the lack of hydrided grain boundary α could be that this phase contains high Al, partitioned from the β phase. Hydriding is suppressed in Ti-Al binary alloys[63].)

Pound employed an electrochemical technique to conclude that hydrogen is more strongly (irreversibly) trapped in STA Beta-21S compared to reduced but

similar trapping in both solution treated and STA Ti-15-3[64,65].[4] He speculated that hydrogen was irreversibly trapped at α/β interfaces associated with the α-colony microstructure, and that this hydrogen localization explains the severe intergranular EAC in STA Beta-21S, but not in STA Ti-15-3. It is plausible that an increased hydrogen concentration at interfaces which are demonstrated brittle crack paths (Fig. 7) can lead to increased EAC susceptibility through the HEE mechanism[27,54]. Hydrogen trapping at α/β interfaces in STA β-titanium alloys could result from misfit strain, and could depend on the compositions of the α and β phases through changes in the lattice parameter of each[66]. Alternately, α-colony interfaces could be disordered, particularly if not crystallographically related to the β matrix or at α plate ends, and hence irreversible H trap sites[66]. While it is reasonable to expect different H trapping behavior for STA Beta-21S with colony α, compared to Ti-15-3, the detailed interfacial structures have not been defined.

The correlation between grain boundary α-colonies, H trapping and intergranular EAC susceptibility in STA Beta-21S, RSTA Ti-15-3, and other β-titanium alloys is highly speculative[64,65]. These electrochemical measurements do not prove a dominant role of hydrogen trapping in EAC, because trapping is but one element in a complex cracking process that depends on a variety of alloy and microstructure-dependent factors. The micromechanical and chemical details of the HEE mechanism are uncertain[27,36]. It is necessary to define the precise crack path through β grain boundaries with adjacent α colonies. Colony α may be hard and prone to EAC due to partitioned aluminum in ordered solid solution, or causing Ti_3Al precipitation analogous to α/β titanium alloys[11,47]. While plastic deformation would localize in softer adjacent β[48-50], aluminum hardened α could constrain this phase and promote high stresses normal to the α/β boundary, and thus favor hydrogen enhanced decohesion. It is equally reasonable to speculate that EAC is dominated by locally intense planar slip. This view is supported by the observation that solution treated Beta-21S is more susceptible to

---

[4] Pound studied specimens of Beta-21S and Ti-15-3 that were provided from the current research.

embrittlement by internally predissolved H compared to Ti-15-3, in the absence of any α and associated hydrogen trap sites[30,31].

Young demonstrated that high temperature-long time solution treated, single phase Beta-21S (871°C for 8 hours) and Ti-15-3 (950°C for 12 hours) each deform by intensely localized planar slip[30,53]. In contrast low temperature-short time solution treated Ti-15-3 deforms by localized but significantly more irregular (wavy) slip. While the solution treatment effect on slip mode in single phase β is clear, the causal mechanism and the effect of α precipitation on this deformation mode in STA alloys were not determined[30,53]. It is reasonable to speculate that slip is more intensely planar in STA Beta-21S compared to the standard solution treatment of STA Ti-15-3. Okada et al. report that slip localization in the β matrix of Ti-15-3 is enhanced by colonies of shearable fine α plates compared to slip homogenization from large intragranular α plates in multiple orientations[67]. TEM showed that intragranular α in low temperature-short time solution treated Ti-15-3 and Beta-21S was similarly of the Burger's orientation (viz., $(110)_\beta$ // $(0001)_\alpha$ and $[111]_\beta$ // $[11\text{-}20]_\alpha$). This phase was somewhat larger in STA Ti-15-3, due to earlier nucleation during peak aging, and could further homogenize slip. In contrast grain boundary α colonies could further intensify localized slip for STA Beta-21S (and in high temperature long-time solution treated Ti-15-3) if colony α plates are crystallographically aligned to favor easy passage of slip[67].

The microstructural factor which governs EAC in STA β-titanium alloys could, therefore, be locally intense planar slip as reported for a variety of aluminum[68] and α/β titanium[7,8,11] alloys. Beta composition, the α-colony structure, and perhaps high aluminum in this α could favor localized slip which would intersect β grain boundaries. Such slip could promote H transport from the crack tip surface, H trapping at deformation induced interfacial defects (e.g., microvoids), and local stress/strain concentration; all of which could contribute to increased HEE[36].

Processing could mitigate chloride EAC in β-titanium alloys. Either cold deformation of high temperature-long time solution treated Beta-21S prior to aging, or lower temperature-short time solution treatment, should provide intragranular nucleation sites for α precipitates and perhaps alter slip localization.

Duplex temperature aging may uniformly nucleate α on precursor ω or β' sites and reduce the likelihood of grain boundary α colonies[28]. STA β-titanium alloys with homogeneously distributed α precipitates should be more resistant to EAC, at least in modestly aggressive aqueous chloride environments.

Effect of Loading Rate on EAC At issue is why NaCl EAC in STA Beta-21S was not produced during constant load exposures for times that were an order of magnitude longer than those which produced intergranular embrittlement during rising load. As reported for several α/β and β-titanium alloys including Ti-15-3, aqueous EAC is maximized at intermediate loading rates for both smooth uniaxial tensile specimens[17] and precracked fracture mechanics specimens[8,26].[5] The lack of resolvable EAC during constant load exposures of STA Beta-21S and Ti-15-3 is consistent with this trend. For a stationary crack, the tip strain rate at constant load is determined by the process zone creep rate and is probably orders of magnitude slower than the crack tip strain rates typical of the rising load experiments which produced intergranular EAC, Figs. 6 and 8[36].

Average crack growth rates for peak aged Beta-21S in NaCl increase with increasing loading rate at stress intensities below K_{ICI}. Since absolute K_{TH} levels were similar for the two loading rates represented in Fig. 6, a 20-fold increase in crack tip strain rate at any location within the crack tip process zone resulted in a 10-fold increase in da/dt estimated from electrical potential measurements of crack length. This behavior is intrinsic to EAC in Beta-21S.[6] Since stress intensity did not decline during EAC extension at either rate (Fig. 6), there is no macroscopic driving force or compliance-based explanation for the reduction in da/dt with decreasing loading rate or crack tip strain rate.

Reduced da/dt and increased K_{TH} with decreasing strain rate are predicted by crack tip film rupture and anodic dissolution modeling of EAC[69]. The amount

---

5 Analogous behavior is not observed for all α/β titanium alloys. Severe aqueous chloride EAC, with K_{ISCC} well below K_{IC}, was produced by static loading[25,52]. K_{TH} was claimed to be minimized at intermediate loading rates, however, only a modest range of strain rates was investigated and constant load experiments were not conducted[26].

6 Average crack growth rates during stable tearing in a benign environment increase in direct proportion to the imposed load line displacement rate[39]. This behavior only occurs at applied K levels above K_{IC} and is not relevant to subcritical EAC.

of dissolution charge passed per unit time, and da/dt, decrease as the frequency of rupture events decreases due to decreased crack tip strain rate. Alternately, this strain rate effect can be qualitatively explained based on HEE. Hydrogen production, uptake and embrittlement could be severe at crack tip strain rates which balance surface passive film destabilization, or rupture (promoted by increased loading rate), the time necessary for H diffusion into the crack tip process zone (promoted by decreased loading rate), and dislocation transport of H to the crack tip region (promoted by increased loading rate up to a critical dislocation velocity)[36]. Static loading may not provide the strain rate and accumulated strain necessary to mechanically destabilize or rupture the crack tip passive film; this film could hinder H production and/or uptake[56]. Alternately, static load strain rates may hinder dislocation motion to transport H from the crack tip surface to trap sites within the process zone, for example at β grain boundaries and α colonies. The displacement rates represented in Figs. 6 and 8 provide the balance between film destabilization, H diffusion, and dislocation transport of H for severe intergranular EAC in the Beta-21S/aqueous NaCl system. The relative contributions of each factor remain to be established, as does the extent of EAC at higher loading rates where H diffusion, dislocation transport of H and perhaps electrochemical reaction may be precluded.

The limited observation of crack bursting for Beta-21S in NaCl is consistent with discontinuous HEE, however, bursting must be systematically characterized.

Effect of Electrode Potential on EAC That intergranular NaCl EAC in STA Beta-21S is mitigated by cathodic polarization (Fig. 9) is explainable based on HEE, provided that local electrochemical conditions near the crack tip are considered. HEE in the ferritic steel/NaCl system is promoted at anodic potentials, where enhanced dissolution promotes hydrolytic acidification and H production at the occluded crack tip, as well as at cathodic potentials where H production increases due to increasingly rapid water reduction kinetics[55,56].

The situation is different for β-titanium alloys in aqueous chloride. Hydrolysis, substantial IR-based crack tip potential differences, and consequently enhanced proton reduction, enable H production and uptake at free corrosion and anodic potentials. A crack tip passive film forms and is periodically ruptured by

crack tip strain; the potential of the bare metal is significantly cathodic (e.g., -1600 mV_{SCE}) to the free corrosion potential[69,70]. With increasing cathodic polarization, acidification is reduced and the crack tip solution becomes alkaline due to increased water reduction producing hydroxyl ions. Recent experiments with scratched electrodes of β-titanium alloys in simulated crack solutions show that current versus time behavior and repassivation rates are similar for pH 1 conditions (approximating solution at the crack tip at free corrosion), pH 8 (a lower bound simulating the crack tip during cathodic polarization at -1000 mV_{SCE}), and pH 10 solution[70]. Critically, however, the rates of cathodic H production are several orders of magnitude lower for the alkaline cases, at a potential of -1600 mV_{SCE}, which simulates the mechanically bared crack tip.

We speculate that K_{TH} for NaCl EAC in STA Beta-21S is low at -600 mV_{SCE} because of substantial H production and uptake from acid solution at the crack tip, analogous to the steel case. K_{TH} increases to equal K_{ICI} with increasing cathodic polarization because H production is greatly reduced for bare titanium in alkaline crack solution, in contrast to the steel case.

CONCLUSIONS

1. Peak aged Beta-21S is susceptible to environment assisted cracking (EAC) in aqueous NaCl at -600 mV_{SCE} when subjected to rising stress intensity. The threshold to initiate subcritical crack propagation (K_{TH} = 39 to 46 MPa$\sqrt{m}$) is significantly reduced compared to the plane strain fracture toughness of 66 MPa$\sqrt{m}$, and environmental crack propagation is fully intergranular for STA Beta-21S in chloride compared to microvoid-based for moist air.

2. The crack initiation fracture toughness (57 to 64 MPa$\sqrt{m}$) and transgranular microvoid fracture processes for STA Ti-15-3 are unaffected by aqueous chloride exposure for several slow loading rates and applied electrode potentials. Intergranular EAC in peak aged Ti-15-3 is promoted by increased solution treatment temperature and/or time.

3. Intergranular EAC in STA Beta-21S and RSTA Ti-15-3 correlates with the

presence of preferentially precipitated α-colonies at β grain boundaries and/or highly localized planar slip; both features are promoted in each alloy by high temperature-long time solution treatment. The relative importance of boundary α-colonies and planar slip is not established, however, hydrogen trapping at α/β interfaces coupled with stress and strain localization near β grain boundaries may be important.

4. EAC in STA Beta-21S is eliminated by applied cathodic polarization at -1000 mV_{SCE}; and occurs, but is not exacerbated during anodic polarization at -150 mV_{SCE}.

5. EAC in peak aged Beta-21S is not produced during static loading for times similar to the deleterious rising load case, and average subcritical EAC growth rates decrease with decreasing crack tip strain rate.

6. EAC in STA Beta-21S may proceed by hydrogen environment embrittlement. The beneficial effects of cathodic polarization and slow crack tip strain rates are speculatively traced to reduced hydrogen production and entry at the occluded crack tip for the former, and to increased crack tip passive film stability or reduced dislocation transport of hydrogen for the latter.

7. The 25°C chloride EAC resistance of STA β-titanium alloys can be superior to that of quenched and tempered martensitic steels at similar high strengths, certainly for cathodic polarization and short term static loading. Beta titanium alloys are not, however, intrinsically immune to chloride EAC; thermomechanical processing must be controlled for cracking resistance.

ACKNOWLEDGEMENTS

This research was supported by the Office of Naval Research (Grant N00014-91-J-4164), with Dr. A. John Sedriks as Scientific Monitor, and by the Virginia CIT Center for Electrochemical Science and Engineering at the University of Virginia. Material was donated by the Titanium Metals Corporation. Transmission electron microscopy was conducted by Professor K.R. Lawless. These contributions are gratefully acknowledged.

REFERENCES

1. Beta Titanium Alloys in the 80's, R.R. Boyer and H.W. Rosenberg, eds., TMS-AIME, Warrendale, PA, pp. 209-229, 1983.

2. Seventh World Conference on Titanium, F.H. Froes, ed., TMS-AIME, Warrendale, PA, in press, 1993.

3. Beta Titanium Alloys in the 1990's, D. Eylon, R.R. Boyer and D.A. Koss, eds., TMS-AIME, Warrendale, PA, 1993.

4. T.W. Duerig and J.C. Williams, in Beta Titanium Alloys in the 80's, R.R. Boyer and H.W. Rosenberg, eds., TMS-AIME, Warrendale, PA, pp. 19-67, 1983.

5. R.W. Schutz, "Effective Utilization of Titanium Alloys in Offshore Systems", Paper No. 6909, 24th Annual Offshore Technology Conference, Houston, TX, 1992.

6. W.W. Love, C.J. Cron and D. Holligan, in Sixth World Conference on Titanium, P. Lacombe, R. Tricot and G. Beranger, eds., Societe Francaise de Metallurgie, Les Ulis Cedex, France, pp. 443-448, 1988.

7. R.J.H. Wanhill, British Corrosion Journal, Vol. 10, No. 2, pp. 69-78, 1975.

8. M.J. Blackburn, J.A. Feeney, and T.R. Beck, in Advances in Corrosion Science and Technology, M.G. Fontana and R.W. Staehle, eds., Vol. 3, Plenum Publishing, NY, NY, pp. 67-292, 1972.

9. R.W. Schutz and D.E. Thomas, in Corrosion: Metals Handbook, Vol. 13, Ed. 9, ASM International, Metals Park, OH, pp. 669-706, 1987.

10. R.W. Schutz, in Stress Corrosion Cracking, R.H. Jones, ed., ASM International, Metals Park, OH, pp. 265-297, 1992.

11. M.J. Blackburn, W.H. Smyrl, and J.A. Feeney, Chapter 5 in Stress Corrosion Cracking High Strength Steel and in Titanium and Aluminum Alloys, B.F. Brown, ed., Naval Research Laboratory, Washington, D.C., pp. 245-363, 1972.

12. R.W. Schutz in Beta Titanium Alloys in the 1990s, D. Eylon, R.R. Boyer and D.A. Koss, eds., TMS-AIME, Warrendale, PA, pp. 75-91.

13. D.N. Fager and W.F. Spurr, Trans. ASM, Vol. 61, pp. 283-292, 1968.

14. J.A. Feeney and M.J. Blackburn, Met. Trans., Vol. 1, pp. 3309-3323, 1970.

15. M.J. Blackburn, J.A. Feeney and T.R. Beck, "State-of-the-Art of Stress Corrosion Cracking of Titanium Alloys", Monograph Review, Part 4, Advanced Research Projects Agency, ARPA Order No. 878 (or NAS7-489) 1970.

16. Corrosion: Metals Handbook, Vol. 13, Ed. 9, ASM International, Metals Park, OH, pp. 483-485, 1987.

17. C. Gagg and B. Toloui, in Sixth World Conference on Titanium, P. Lacombe, R. Tricot and G. Beranger, eds., Societe Francaise de Metallurgie, Les Ulis Cedex, France, pp. 545-550, 1988.

18. R.W. Schutz, M. Xiao and T.A. Bednarowicz, "Stress Corrosion Behavior of Ti-3Al-8V-6Cr-4Mo Under Deep Sour Gas Well Conditions", Paper No. 51, Corrosion 92, NACE, Houston, TX, 1992.

19. R.W. Schutz and M. Xiao, "Stress Corrosion Behavior of Ti-38644 Titanium Alloys Products in Methanol Solutions", Paper No. 148, Corrosion 93, NACE, Houston, TX, 1993.

20. I. Azkarate and A. Pelayo, "Hydrogen Assisted Stress Cracking of Titanium Alloys in Aqueous Chloride Environments", unpublished research report, INASMET, San Sebastian, Spain.

21. L.H. Wolfe, C.C. Burnette and M.W. Jossten, Materials and Protection, pp. 14-21, July, 1993.

22. B. Bavarian, V. Wahi and M. Zamanzadeh, "Corrosion Behavior of Beta-21S Titanium Alloy in Chloride-Containing Environments", Paper No. 284, Corrosion 93, NACE, Houston, TX, 1993.

23. D.E. Thomas and S.R. Seagle in Titanium Science and Technology, G. Lutjering, U. Zwicker and W. Bunk, eds., pp. 2533-2540, 1984.

24. D.A. Meyn and P.S. Pao, in Slow Strain Rate Testing for the Evaluation of Environmentally Induced Cracking: Research and Engineering Applications, ASTM STP 1210, R.D. Kane, ed., ASTM, Philadelphia, PA, pp. 158-169, 1993.

25. B.F. Brown, Mater. Res. Std., Vol. 6, pp. 129-136, 1966.

26. J.A. Muskovitz and R.M. Pelloux, Corrosion, Vol. 35, pp. 509-514, 1979.

27. R.P Gangloff, in Corrosion Prevention and Control, M. Levy and S. Isserow, eds., US Army Laboratory Command, Watertown, MA, pp. 64-111, 1986.

28. L. Wagner and J.K. Gregory, in Beta Titanium Alloys in the 1990's, D. Eylon, R.R. Boyer and D.A. Koss, eds., TMS-AIME, Warrendale, PA, pp. 199-209, 1993.

29. L.M. Young and R.P. Gangloff, "Hydrogen Environment Embrittlement of Beta Titanium Alloys", in Seventh World Conference on Titanium, F.H. Froes, ed.. TMS-AIME, Warrendale, PA, in press, 1993.

30. G.A. Young, Jr., "Hydrogen Effects in Metastable β-Titanium Alloys", M.S. Thesis, University of Virginia, Charlottesville, VA, 22901.

31. G.A. Young, Jr. and J.R. Scully, Scripta Metall., Vol. 28, pp. 507-512, 1993.

32. T.W. Duerig, G.T. Terlinde and J.C. Williams, Metall. Trans. A, Vol. 11A, pp. 1987-1998, 1980

33. G. Hari Narayanan and T.F. Archbold, Met. Trans. Vol. 1, pp. 2281-2290, 1990.

34. T.J. Headley and H.J. Rack, Metall. Trans. A, Vol. 10A, pp. 909-920, 1979.

35. J.C. Williams, in Titanium Science and Technology, R.I. Jaffee and H.M. Burte, eds., TMS-AIME, New York, pp. 1433-1494, 1973.

36. L.M. Young, "Environment Assisted Cracking in β-Titanium Alloys", M.S. Thesis, University of Virginia, Charlottesville, VA, 1993.

37. D.R. Anderson and J.P. Gudas, in Environment Sensitive Fracture: Evaluation and Comparison of Test Methods, ASTM STP 821, S.W. Dean, E.N. Pugh and G.M. Ugiansky, eds., ASTM, Philadelphia, PA, pp. 98-113, 1984.

38. E.M. Hackett, P.J. Moran and J.P. Gudas, in Fracture Mechanics: Seventeenth Volume,ASTM STP 905, J.H. Underwood, et al., eds., ASTM, Philadelphia, PA, pp. 512-541, 1986.

39. R.A. Mayville, T.J. Warren and P.D. Hilton, Trans. ASME, Vol. 109, pp. 188-193, 1987.

40. J.K. Donald and J. Ruschau, in Fatigue Crack Measurement: Techniques and Applications, K.J. Marsh, R.A. Smith and R.O. Ritchie, eds., EMAS, Ltd, West Midlands, UK, pp. 11-37, 1991.

41. H. Tada, P.C. Paris and G.R. Irwin, The Handbook, Del Research Corp., St. Louis, MO, p. 2.11, 1985.

42. P. Doig and K.R. Abbott, J. Test. Eval., Vol. 12, pp. 297-304, 1984.

43. W.C. Porr, Jr. and R.P. Gangloff, "Elevated Temperature Fracture of RS/PM Alloy 8009: Part I-Fracture Mechanics Behavior", Metall. Trans. A, in press, 1993.

44. "Standard Test Method for J_{IC}, A Measure of Fracture Toughness", Designation E 813-89, Annual Book of ASTM Standards, 3.01, ASTM, Philadelphia, PA, pp. 732-746, 1992.

45. "Standard Test Method for Determining Plane-Strain Fracture Toughness of Metallic Materials", Designation E 399-83, Annual Book of ASTM Standards, 3.01, ASTM, Philadelphia, PA, pp. 506-536, 1992.

46. K.S. Chan, Acta Metall., Vol. 37, pp. 1217-1226, 1989.

47. M.J. Blackburn and W.H. Smyrl, in Titanium Science and Technology, R.I. Jaffee and H.M. Burte, eds., Plenum Press, NY, NY, pp. 2577-2609, 1973.

48. F.H. Froes, J.C. Chesnutt, C.G. Rhodes and J.C. Williams, in Toughness and Fracture Behavior of Titanium, ASTM STP 651, ASTM, Philadelphia, PA, pp. 115-153, 1978.

49. E. Breslauer and A. Rosen, Matls. Sci. and Tech., Vol. 7, pp. 441-446, 1991.

50. G. Terlinde and K.-H. Schwalbe, "The Role of α-phase in the Fracture Toughness of and Tensile Fracture of an Aged, Metastable β-Ti-Alloy", in Microstructure, Fracture Toughness and Fatigue Crack Growth in Titanium Alloys, A.K. Chakrabarti and J.C. Chesnutt, eds., TMS-AIME, Warrendale, PA, pp. 97-109, 1987.

51. N. Niwa and H. Takatori, in Beta Titanium Alloys in the 1990s, D. Eylon, R.R. Boyer and D.A. Koss, eds., TMS-AIME, Warrendale, PA, pp. 237-247, 1993.

52. W.F. Czyrklis and M. Levy, in Environment Sensitive Fracture of Engineering Materials, Z.A. Foroulis, ed., TMS-AIME, Warrendale, PA, pp. 303-313, 1979.

53. G.A. Young, Jr. and J.R. Scully, in Beta Titanium Alloys in the 1990s, D. Eylon, R.R. Boyer and D.A. Koss, eds., TMS-AIME, Warrendale, PA, pp. 147-158, 1993.

54. R.P. Gangloff, Matls. Sci. Engr., Vol. A103, pp. 157-166, 1988.

55. R.P. Gangloff and A. Turnbull, in Modeling Environmental Effects on Crack Initiation and Propagation, R.H. Jones and W.W. Gerberich, eds., TMS-AIME, Warrendale, Pa., pp. 55-81, 1986.

56. J.R. Scully and P.J. Moran, J. Electrochem. Soc., Vol. 135, pp. 1337-1348, 1988.

57. H.G. Nelson, in Hydrogen in Metals, I.M. Bernstein and A.W. Thompson, eds., TMS-AIME, Warrendale, PA, pp. 445-464, 1973.

58. D.G. Kolman and J.R. Scully, "Electrochemistry and Passivity of a Ti-15Mo-3Nb-3Al β-Titanium Alloy in Ambient Temperature Aqueous Chloride Solutions", J. Electrochem. Soc., in press, 1993.

59. D.G. Kolman and J.R. Scully, "Electrochemistry and Passivity of a Ti-15V-3Cr-3Al-3Sn β-Titanium Alloy in Ambient Temperature Aqueous Chloride Solutions", J. Electrochem. Soc., in press, 1993.

60. M.A. Imam, P.K. Poulose and B.B. Rath, in Beta Titanium Alloys in the 1990s, D. Eylon, R.R. Boyer and D.A. Koss, eds., TMS-AIME, Warrendale, PA, pp. 261-271, 1993.

61. H. Fujii and H.G. Suzuki, in Beta Titanium Alloys in the 1990s, D. Eylon, R.R. Boyer and D.A. Koss, eds., TMS-AIME, Warrendale, PA, pp. 249-259, 1993.

62. J.E. Costa, D. Banerjee and J.C. Williams, in Beta Titanium Alloys in the 80's, R.R. Boyer and H.W. Rosenberg, eds., TMS-AIME, Warrendale, PA, pp. 69-84, 1983.

63. J.D. Boyd, Trans. ASM, Vol. 62, pp. 977-988, 1969.

64. B.G. Pound, "The Effect of Aging on Hydrogen Trapping in β-Titanium Alloys", Acta Metall. et Mater., in review, 1993.

65. B.G. Pound, "Hydrogen Trapping in β-Titanium Alloys-The Link Between Microstructure and Hydrogen Embrittlement", Acta Metall. et Mater., in review, 1993.

66. G.M. Pressouyre, Metall. Trans. A, Vol. 10A, pp. 1571-1592, 1979.

67. M. Okada, D. Banerjee, and J.C. Williams, in Titanium Science and Technology, Vol. 3, G. Lütjering, U. Zwicker, and W. Bunk, eds., Oberursel, Deutsche Gesellschaft für Metallkunde, pp. 1835-1842, 1984.

68. J. Albrecht, A.W. Thompson and I.M. Bernstein, Metall. Trans. A, Vol. 10A, pp. 1759-1766, 1979.

69. F.P. Ford in Environment Induced Cracking of Metals, R.P. Gangloff and M.B. Ives, eds., NACE, Houston, TX, pp. 139-166, 1990.

70. D.G. Kolman and J.R. Scully, unpublished research, University of Virginia, Charlottesville, VA, 1993.

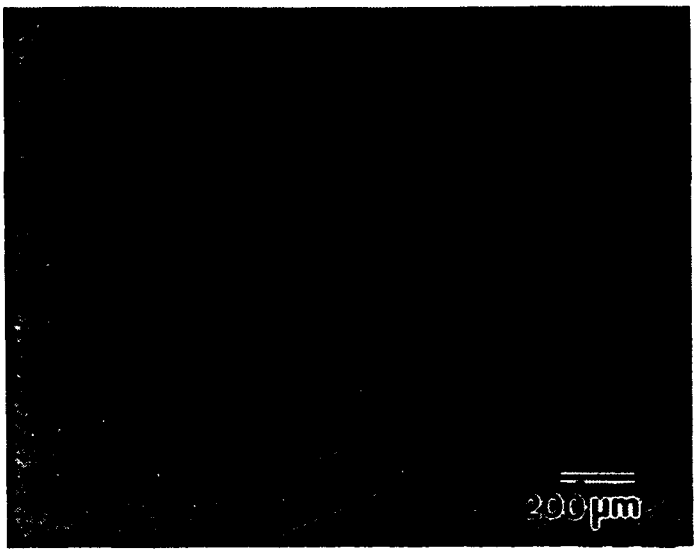

(a)

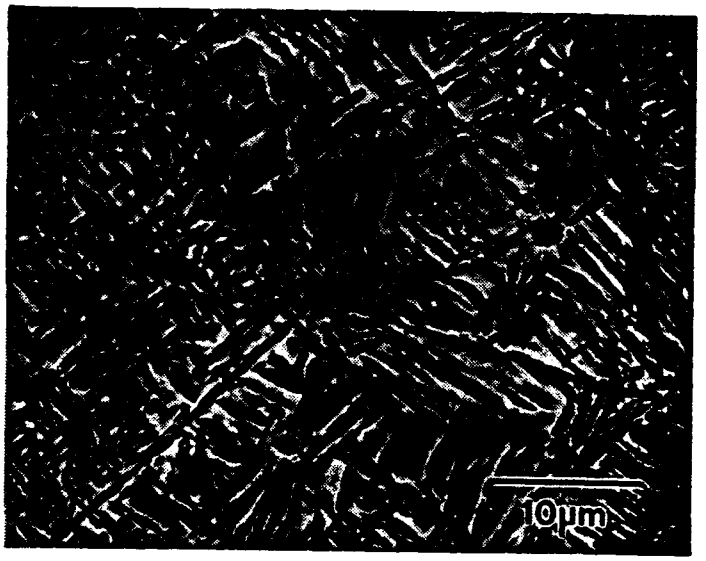

(b)

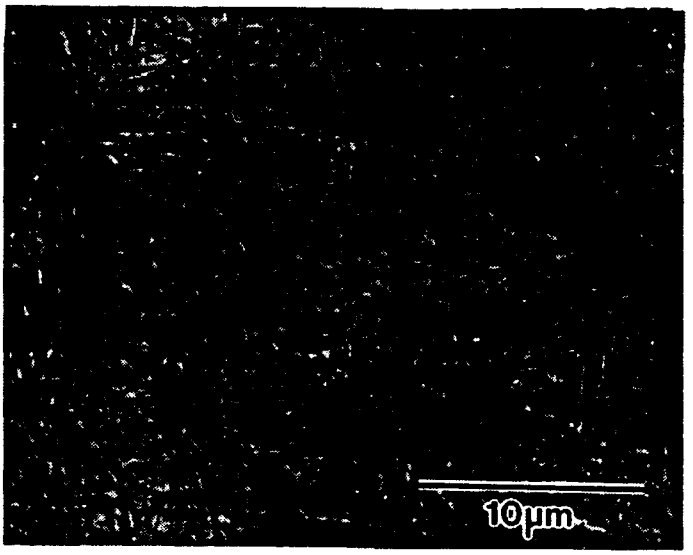

(c)

Figure 1 (a) Optical micrograph of as-received solution treated Beta-21S, and scanning electron micrographs of solution treated and peak aged (STA): (b) Ti-15-3 and (c) Beta-21S.

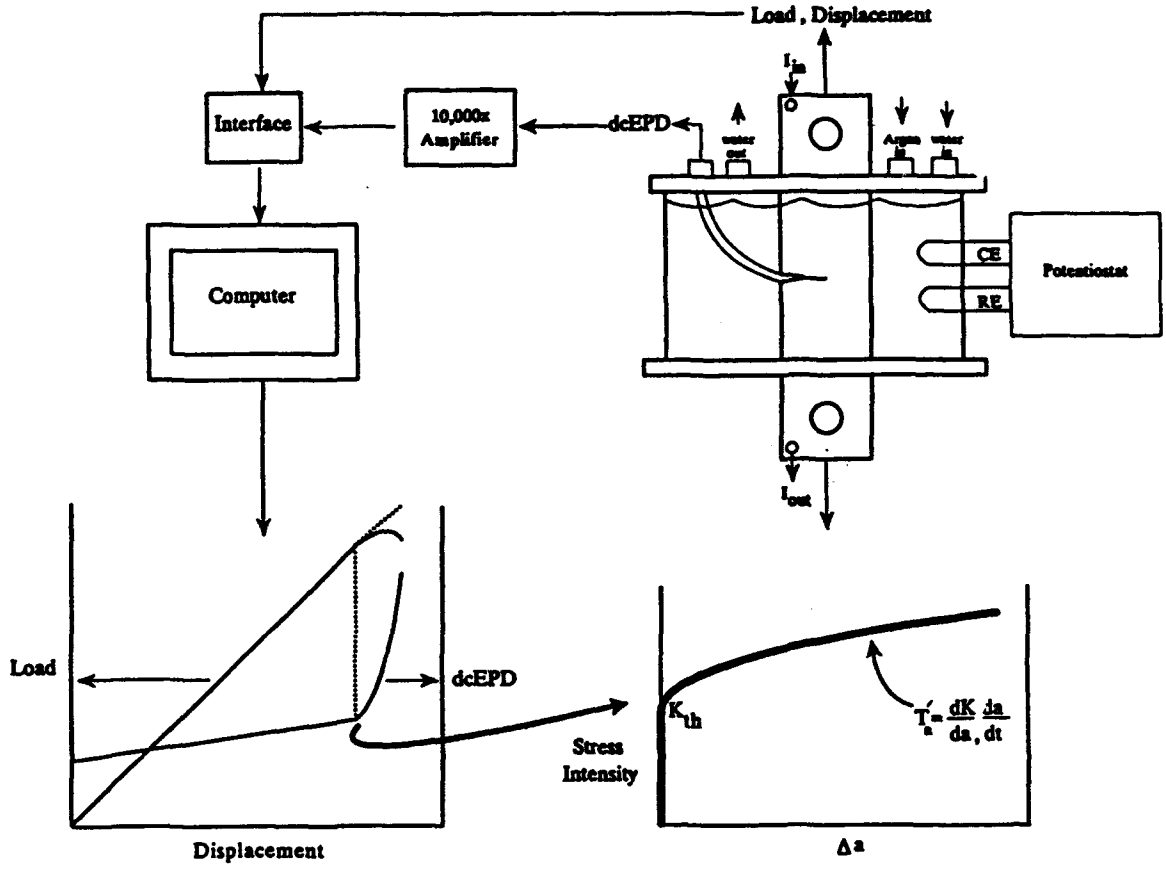

Figure 2 The rising load EAC experimental method. (K_{TH} is defined at zero crack extension, while stable crack growth is characterized by dK/dΔa and by da/dt.)

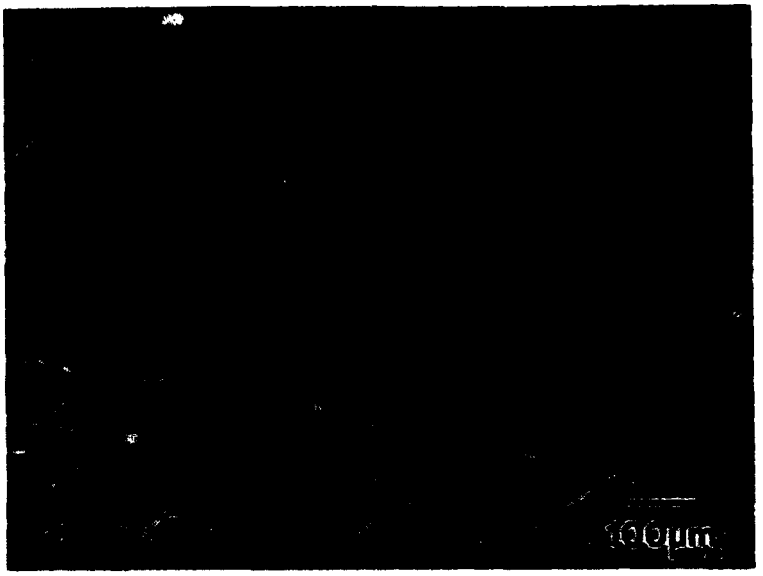

(a)

(b)

Figure 3 Scanning electron fractographs for: (a) STA Ti-15-3 in moist air and (b) STA Beta-21S in moist air. The fatigue crack is at the top of each image and the crack grew from top to bottom.

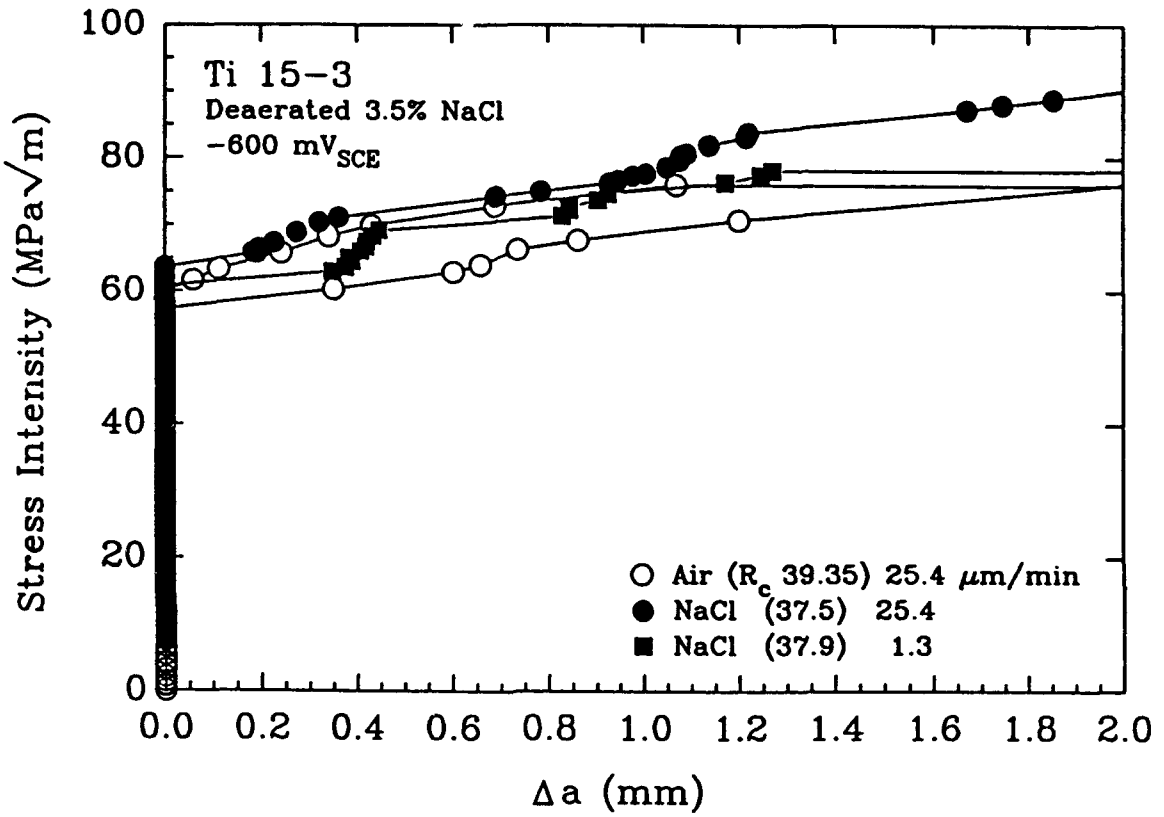

Figure 4 K-Δa data for STA Ti-15-3 in air and 3.5% NaCl (-600 mV_{SCE}) at two fixed actuator displacement rates. Hardness values (R_c) for each specimen are given in the legend.

(a)

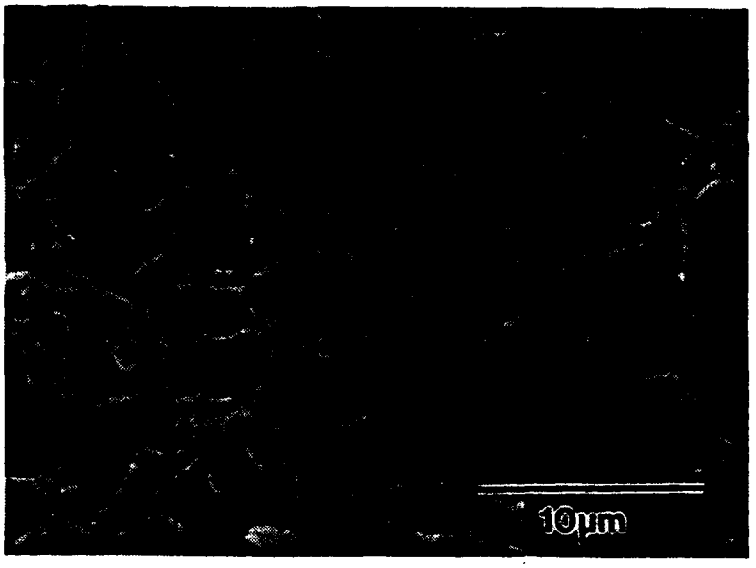

(b)

Figure 5 Scanning electron fractographs for STA Ti-15-3 in 3.5% NaCl (-600 mV_{SCE} and 25.4 μm/min) at: (a) low magnification showing the fatigue precrack (top) and initial cracking in the aqueous solution and (b) high magnification showing microvoids.

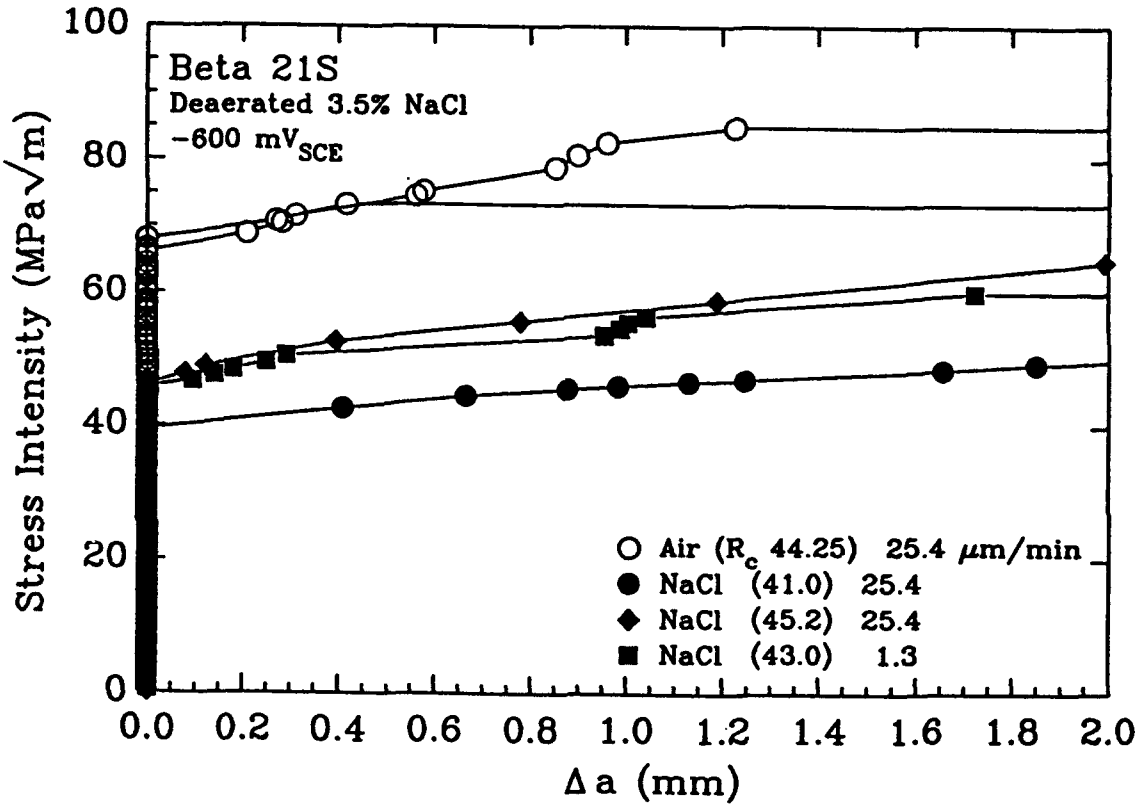

Figure 6 K-Δa for STA Beta-21S in air and 3.5% NaCl (-600 mV_{SCE}) at two loading rates. Hardness values (R_c) for each specimen are in the legend.

Figure 7 Scanning electron fractograph for STA Beta-21S in 3.5% NaCl at -600 mV_{SCE} and an actuator displacement rate of 25.4 μm/min.

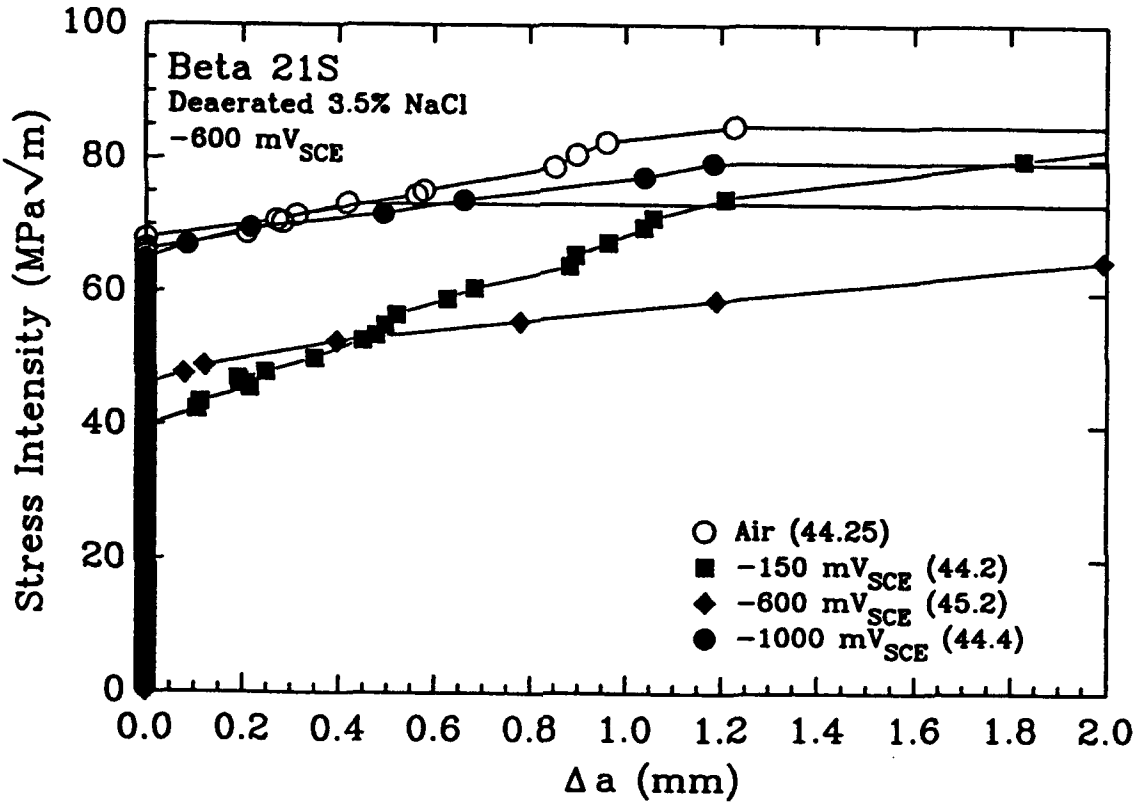

Figure 8 Effect of electrode potential on K-Δa for STA Beta-21S in 3.5% NaCl at a constant displacement rate of 25.4 μm/min. Hardness values (R_c) for each specimen are provided in the legend.

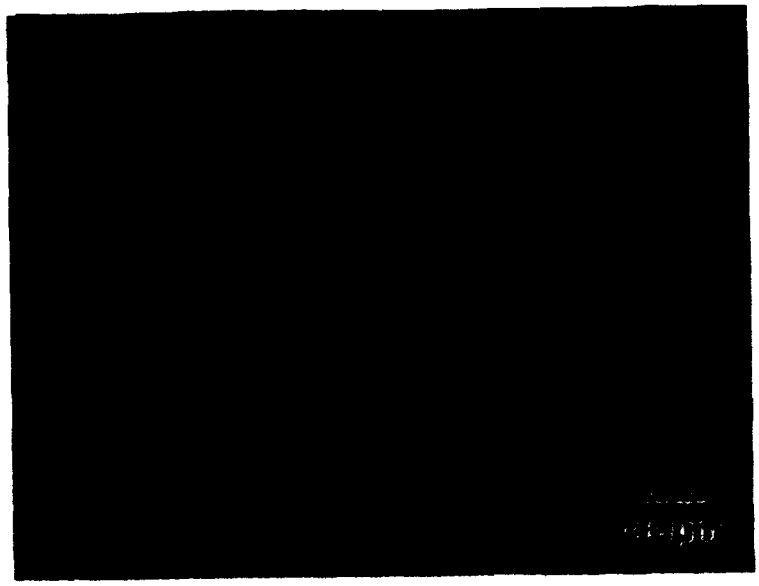

(a)

(b)

Figure 9 SEM fractographs of STA Beta-21S in NaCl at: (a) -150 mV_{SCE} and (b) -1000 mV_{SCE}.

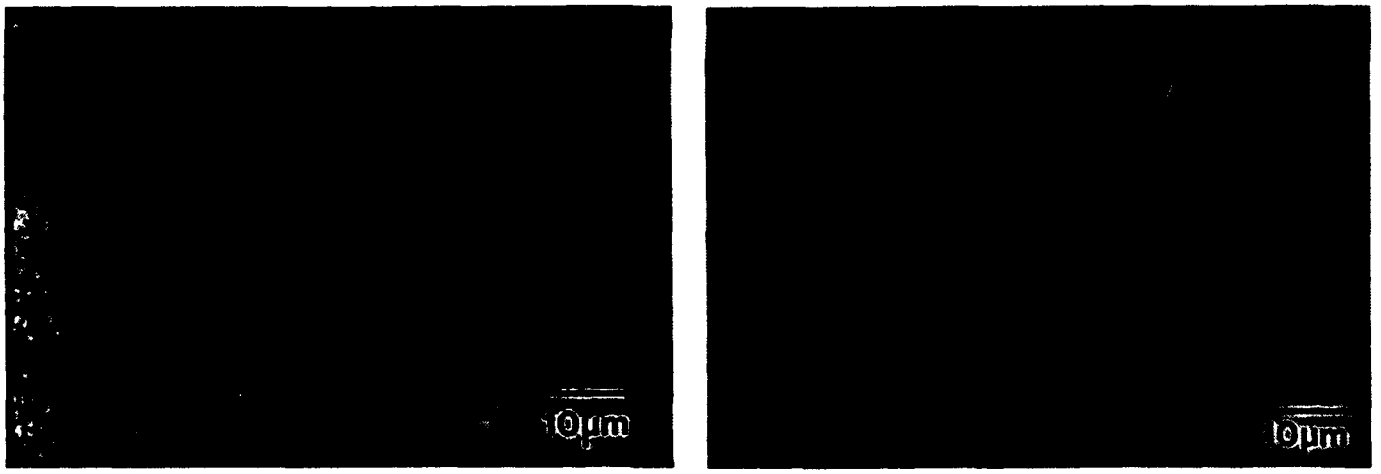

(a) (b)

(c)

Figure 10 Optical micrographs of underaged (1 hour at 538°C): (a) as received solution treated (816°C for 0.5 hours) Ti-15-3, (b) resolution treated (950°C for 12 hours) Ti-15-3, and (c) as received solution treated (871°C for 8 hours) Beta-21S.

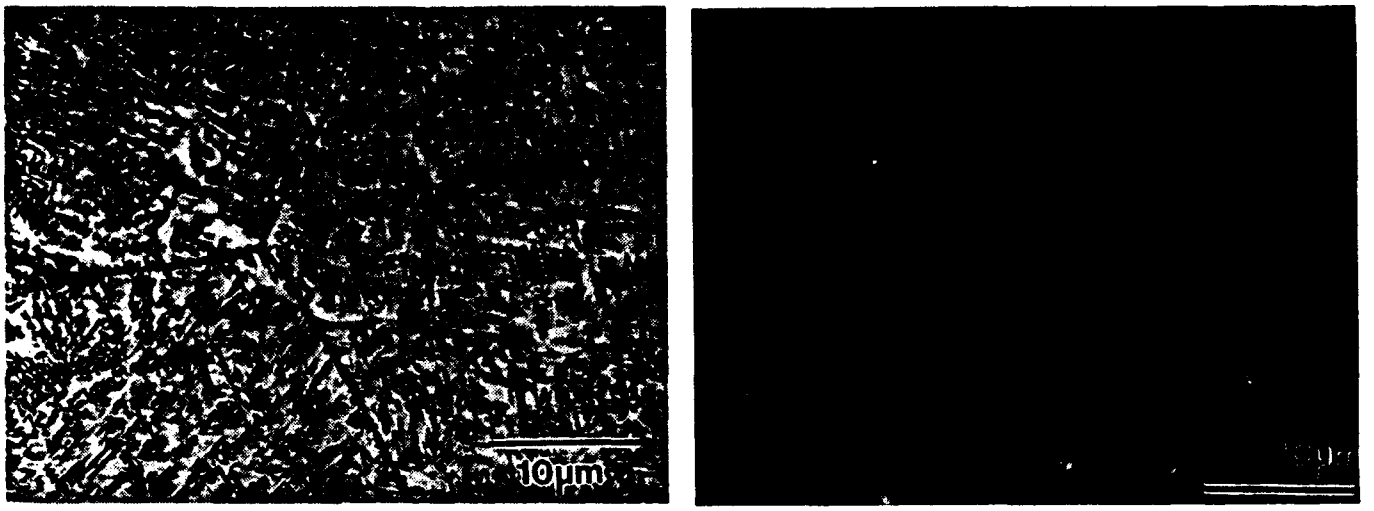

(a) (b)

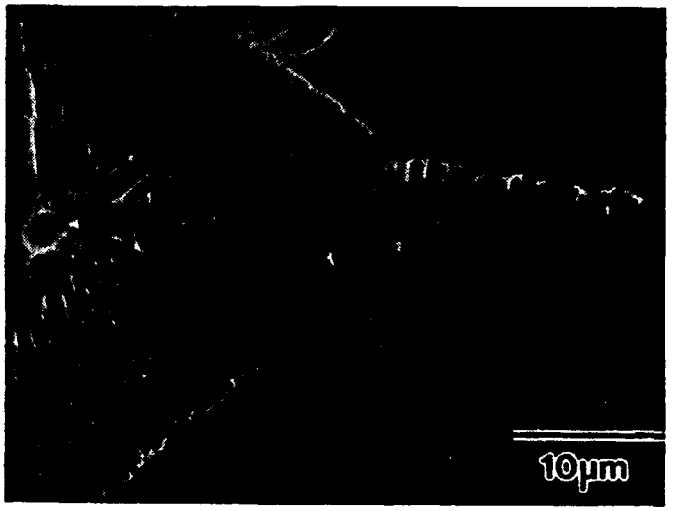

Figure 11 Scanning electron micrographs of underaged (1 hour at 538°C): (a) as received solution treated (816°C for 0.5 hours) Ti-15-3, (b) resolution treated (1038°C for 2 hours) Ti-15-3, and (c) as received solution treated (871°C for 8 hours) Beta-21S.

(a) (b)

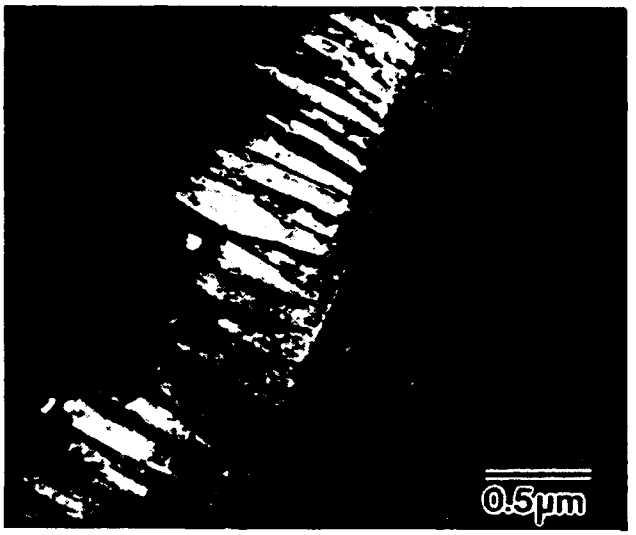

(c)

Figure 12 Transmission electron micrographs of: (a) underaged (1 hour at 538°C) Ti-15-3, (b) peak aged (8 hours at 538°C) Ti-15-3, and (c) peak aged (8 hours at 538°C) Beta-21S; all beginning with the as received solution treatments.

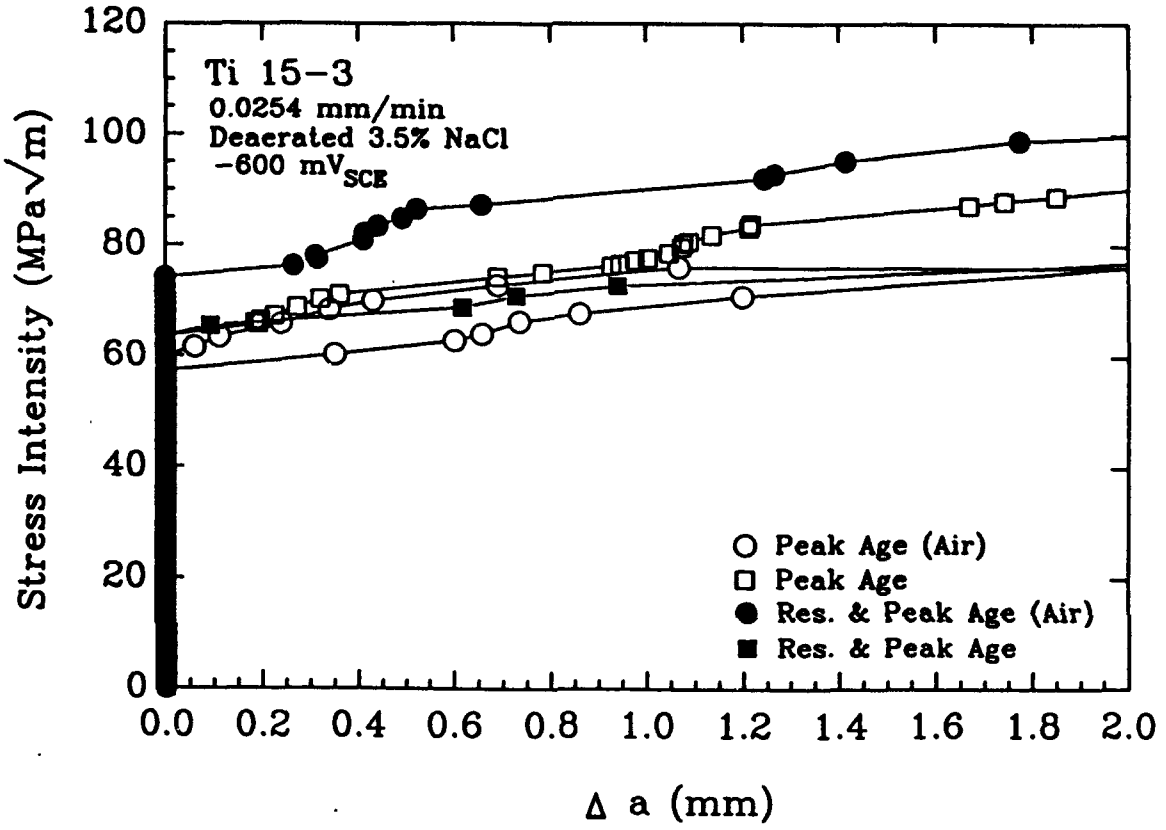

Figure 13 K-Δa for resolution treated (1038°C for 2 hours) and peak aged (8 hours at 538°C) Ti-15-3 in moist air and NaCl (-600 mV_{SCE}), for a single displacement rate of 25.4 μm/min.

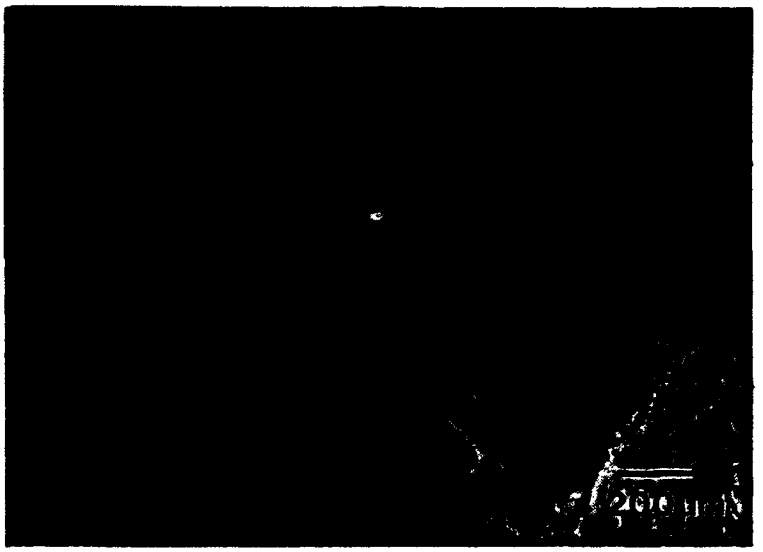

Figure 14 SEM fractograph of resolution treated and peak aged Ti-15-3 in NaCl at -600 mV_{SCE} and a displacement rate of 25.4 μm/min.

INTERNAL HYDROGEN EMBRITTLEMENT OF SOLUTION HEAT TREATED AND AGED Ti-15V-3Cr-3Al-3Sn AND Ti-15Mo-3Nb-3Al

George A. Young, Jr.
John R. Scully

Submitted to *Corrosion Journal*, November 1993

INTERNAL HYDROGEN EMBRITTLEMENT OF SOLUTION HEAT TREATED AND AGED Ti-15V-3Cr-3Al-3Sn AND Ti-15Mo-3Nb-3Al

George A. Young, Jr.* and John R. Scully
Materials Science & Engineering
The University of Virginia
Charlottesville, VA 22903-2442

*Present Address: Knolls Atomic Power Laboratory
Schenectady, NY 12301-1072

ABSTRACT

The effects of electrochemically introduced hydrogen on the room temperature mechanical properties of two β titanium alloys, Ti-15V-3Cr-3Al-3Sn and Ti-15Mo-3Nb-3Al are compared. Solution heat treated (SHT), peak aged (PA), and duplex aged (DA) conditions are investigated using notched tensile bars and Bridgman's analysis of longitudinal stress and average effective plastic strain. Ti-15Mo-3Nb-3Al is more susceptible to hydrogen embrittlement than Ti-15V-3Cr-3Al-3Sn based on reductions in longitudinal stress, plastic strain, and changes in fracture mode at hydrogen concentrations above 1000 wt. ppm. Hydriding of the α and β phases was not observed over the range of hydrogen concentrations investigated. Instead, changes in fracture paths with hydrogen are correlated with deformation behavior and α precipitation. The susceptibility of Ti-15Mo-3Nb-3Al is attributed to a high temperature, long time solution treatment which affects deformation behavior in the SHT condition and promotes grain boundary α precipitation in the PA condition. The high temperature solution treatment removes α nucleation sites from grain interiors and promotes planar slip. Subsequent α precipitation occurs preferentially on β grain boundaries and, lastly, in grain interiors resulting in fine intragranular precipitates. It is hypothesized that fine intragranular α plates as well as aligned boundary α colonies are readily sheared and also promote planar slip in the PA condition. In contrast, a lower temperature, shorter duration solution treatment for Ti-15V-3Cr-3Al-3Sn results in wavy slip and more homogeneous, slightly coarser α precipitates upon aging, which may be less prone to slip localization by dislocation shearing. Localized planar slip and grain boundary α colonies are believed to promote both internal hydrogen embrittlement and aqueous environmentally assisted cracking.

/

keywords: α precipitation, ß-titanium alloys, Bridgman's analysis, cleavage, deformation mode, fracture path, hydriding, hydrogen embrittlement, hydrogen trapping, intergranular cracking, multiple slip, planar slip, stress corrosion cracking, transgranular cracking

INTRODUCTION

Modern ß titanium alloys are candidates for room temperature marine and aerospace applications due to their excellent strength, toughness, formability, and resistance to general and crevice corrosion[1-5]. Although the stress corrosion resistance (SCC) of α and α + ß titanium alloys is well characterized, the environmental cracking resistance of aged ß titanium alloys is less well reported in the literature[6-8]. ß-titanium alloys (Ti-11.5Mo-6Zr-4.5Sn, Ti-13V-11Cr-3Al, and binary Ti-Mo compositions) are susceptible to stress corrosion cracking in ambient temperature neutral halide containing solutions in fracture mechanics experiments[7,9,10]. Fracture occurs both intergranularly and by {100} cleavage[9].

SCC susceptibility is found to be a strong function of electrochemical potential and increasing yield strength[7,8,10]. However, the potential dependency observed for SCC of ß-titanium differs from that observed for *bcc* ferrous alloys long known to be prone to hydrogen embrittlement cracking in halide containing aqueous environments. Specifically, cracking is exacerbated at a potentials near -600 mV vs. SCE for ß-titanium alloys[7,8]. Cracking also occurs at more positive potentials but is not observed at potentials more negative than approximately -1000 mV[7,8,11]. In contrast, a different trend is observed in the case of steels of similar yield strengths. Greater susceptibility is observed at increasingly negative potentials relative to -600 mV vs. SCE as well as at more positive potentials[12-14]. In fact, the *minimum* in susceptibility occurs in the range of approximately -500 to -700 mV vs. SCE in neutral halide containing solutions. The increasing susceptibility trend with cathodic polarization in the case of steel occurs due to the strong correlation between embrittlement susceptibility and fracture process zone hydrogen concentration which depends, in turn, on the supply of hydrogen from the reduction of water reaction[13-15]. The anodic trend is attributed to ferrous and ferric ion hydrolysis, local acidification, enhanced hydrogen production and its absorption from the environment established at occluded sites[13]. In the case of ß-titanium, different controlling electrochemical parameters may allow hydrogen production and entry to occur within the -500 to -700 mV potential range, or entirely different mechanisms govern aqueous room temperature SCC.

Based on the observed lack of SCC susceptibility at -1000 mV, the ability of titanium's compact surface oxide film to limit hydrogen entry[8], its rapid repassivation rate[16,17], and the high hydrogen solubility of the beta matrix[18], hydrogen may be prematurely dismissed as an unlikely embrittling agent for ß-titanium alloys. However, the role of hydrogen in the room temperature aqueous SCC of ß-titanium alloys at potentials near -600 mV SCE should be examined more thoroughly for the following reasons. Hydrogen production is thermodynamically assured at the transiently bare crack tip in the case of Ti due to the negative equilibrium potentials associated with the Ti/Ti^{+2} and Ti/Ti^{+3} oxidation reactions (e.g. -1.87 and -1.21 V vs. SCE at 1 M Ti^{+2} and 1 M Ti^{+3} concentrations, respectively)[19] and the likelihood of significant IR-based voltage differences between transiently bare cracks and external surfaces[16]. Ti^{+3} cations are hydrolyzable; a pH < 1.3 has been reported at pit sites while a pH as low as zero is measured when dissolving $TiCl_3$ under deaerated conditions simulating an occluded crack[16,17,20]. Moreover, hydrogen transport rates in ß-titanium (e.g. $\sim 1\text{-}8 \times 10^{-7}$ cm^2/sec at 25°C) are similar to that of *bcc* steels[21-23] and, consequently, are not expected to limit fracture process zone hydrogen accumulation in monotonic loading experiments at slow strain rate. Finally, hydrogen embrittlement susceptibility is well established

for high strength *bcc* materials particularly as yield strength is increased[24,25]. For these reasons, internal hydrogen should be examined as a possible contributor to room temperature aqueous SCC phenomena.

To date, however, the relative importance of internal hydrogen as either a contributor or the root cause of room temperature aqueous embrittlement of β-titanium alloys has not been unambiguously distinguished from aqueous dissolution. Clearly, both binary beta titanium alloys as well as early developmental β alloys (Ti-13V-11Cr-3Al) can be susceptible to hydrogen embrittlement. Shih and Birnbaum have shown that the solution treated beta alloy Ti-30Mo is extrinsically embrittled through the formation of the *fcc* δ hydride containing 66 at% hydrogen[26]. Solution treated beta alloys are also intrinsically embrittled by hydrogen at bulk concentrations well below that required to produce hydriding of the β matrix[21-27]. Gerberich, et al., have shown a continuous decrease in the fracture stress of solution annealed Ti-30Mo containing 20-1800 ppm by weight of hydrogen without the formation of a hydride[27]. Nakasa and co-workers studied Ti-13V-11Cr-3Al and found a decrease in bending strength for both the solution annealed and peak-aged conditions, again without detection of hydriding in either the α or β phases at hydrogen concentrations up to 15,000 wt. ppm[28]. A {100} cleavage plane was identified on flat fracture surfaces in both the solution annealed and aged conditions. The *fct* ε hydride was detected under extreme autoclave conditions at hydrogen concentrations of the order of 40,000 ppm[28]. Hydrogen was also implicated in the aqueous cracking of aged β-titanium alloy Beta-C (Ti-3Al-8V-6Cr-4Mo-4Zr)[29]. In this study, embrittlement was only observed when pre-cracked specimens were cathodically polarized in H_2S containing acidified chloride solutions. Previous studies of α-β and metastable β-titanium alloys in aqueous solutions also attribute environmental cracking to a hydrogen environment assisted cracking mechanism[11,30,31]. Coincidentally, a {100} cleavage plane[9] as well as intergranular separation[9,11] are observed. Factors supporting a time dependent hydrogen embrittlement phenomena for Ti-15Mo-3Nb-3Al in aqueous solutions include (a) electrochemical conditions at the crack tip which favor hydrogen production, (b) a loading rate dependency, (c) and discontinuous crack bursts[11].

This paper seeks to define the effects of a broad range of internal hydrogen concentrations on the room temperature mechanical properties of solution annealed, peak aged, and duplex aged beta titanium alloys Ti-15Mo-3Nb-3Al and 15V-3Cr-3Al-3Sn and to correlate hydrogen assisted cracking to observed aqueous, environmentally assisted cracking[11]. Here, electrochemical pre-charging of aged or solution heat treated material is conducted near ambient temperature to avoid the complications of hydrogen induced β phase stabilization common to high temperature gaseous charging studies[32-34]. Mechanical testing of pre-charged specimens is performed in air, to decouple hydrogen effects from other aqueous embrittlement mechanisms which may complicate in-situ SCC studies. The strong permeation barrier provided by the titanium oxide is exploited to minimize outgassing of precharged hydrogen during the duration of these tests. Embrittlement is quantified as a function of maximum longitudinal stress, plastic strain at maximum load, and total hydrogen concentration. Hydriding of the α and β phases is investigated through x-ray diffraction. Metallographic, plastic deformation mode and fractographic features are correlated with mechanical property data and likely fracture scenarios are discussed.

EXPERIMENTAL

Metallurgy

Cross rolled plates, nominally 10 mm thick, of Ti-15V-3Cr-3Sn-3Al (referred to as 15-3) and Ti-15Mo-3Nb-3Al (referred to as 21S) were received in the solution annealed condition. The Ti-15V-3Cr-3Sn-3Al alloy was solution heat treated (SHT) at 816°C for 0.5 h while the Ti-15Mo-3Nb-3Al alloy was SHT at 871°C for 8 h (Table 1). Average grain sizes of 90 and 100 μm were determined for 15-3 and 21S, respectively. Solution annealed (SHT), single step peak aged (PA), and duplex aged (DA) heat treatments were investigated. Duplex aging was performed in an attempt to promote a finer, more homogenous α distribution and avoid preferential precipitation on β grain boundaries[35]. Preferential α precipitation has previously been associated with increased susceptibility to stress corrosion cracking, hydrogen embrittlement, and intergranular cracking[36,38]. Table 1 details the heat treatments and corresponding hardness of each condition. Air tensile properties are reported elsewhere[11,37]. Both PA and DA 21S exhibited preferential nucleation of α plates at β grain boundaries while α plates nucleated intragranularly in both PA and DA 15-3. This difference in nucleation behavior is identified metallographically after a one hour age at 538°C as shown in Figure 1a and b. Dark field transmission electron microscopy (TEM) analysis also revealed a 0.1 μm thick α film along β grain boundaries in both 21S and 15-3 after aging at 538°C. Aligned plate-like α colonies were observed perpendicular to β grain boundaries in the 21S alloy both metallographically (Fig. 1a) and by dark field TEM[37]. Subsequent aging to peak strength at 538°C or duplex aging resulted in a high density of intragranular α plates in both alloys. X-ray diffraction (XRD) after SHT, PA and DA heat treatments indicated presence of the β phase (SHT), or β+ secondary α phases (PA, as well as DA). The ω phase was neither detected by TEM-selected area diffraction nor by X-ray diffraction in PA alloys.

Hydrogen Charging

Electrochemical pre-charging of hydrogen was conducted in a solution of 10ml H_2SO_4, 1000ml H_2O and 0.8 g $Na_4P_2O_7$ at 90°C[39]. Previously heat treated and machined tensile specimens were cathodically polarized to 100 A/m^2 for various times, as described elsewhere[36], to facilitate hydrogen uptake and were tested in air. Upon removal from the charging bath, the oxide which forms in air is an effective barrier to hydrogen egress. Hydrogen concentrations reported for each tensile specimen were obtained from a section of the same tensile bar adjacent to the notch by thermal emission (LECO) and represent an average total concentration for the volume of metal tested. Note that the hydrogen uptake rate of 15-3 was approximately 5-6 times greater than that of 21S for all the heat treatments investigated. This increase in hydrogen uptake is attributed, in part, to a higher hydrogen overpotential and fugacity on the surface of 15-3. At 25°C, galvanostatic measurements in the charging solution indicate that 15-3 develops a potential approximately 200 mV cathodic to 21S at an equivalent current density of 100 A/m^2.

Mechanical testing

Circumferentially notched "Bridgman" tensile bars were employed to quantify the effects of hydrogen on the mechanical properties of the alloys investigated[40]. Degree of embrittlement was quantified by determining the maximum longitudinal stress developed at the centerline of the

notched region and the effective plastic strain across the notch diameter at maximum load following the procedures of Hancock et al.[41,42]. All tensile tests were conducted at a crosshead displacement rate of 2.5 x 10^{-6} cm/s. The effect of constraint on the failure stress and strain in PA material was determined as a function of hydrogen concentration at four different initial constraint levels (0.52, 0.62, 1.03, 1.43) where the triaxial constraint is defined as the ratio of mean to effective stress, ($\sigma_m/\bar{\sigma}$)[40-42]. These constraint levels correspond to notch radii of 7.9 mm, 4.8 mm, 1.6 mm, and 7.9 mm respectively at a constant initial diameter across the notch of 6.4 mm. Additional tensile tests, conducted at the constraint level of 1.43 (0.33 = uniaxial tension, 2.50 = sharp notch), compared the effects of hydrogen on SHT, PA, and DA heat treatments.

Deformation mode

The slip behavior of each alloy was investigated by deforming electropolished cubes of SHT material (approximately 1 cm^3) in compression and observing the surface slip lines via optical microscopy.

Detection of hydriding

X-ray diffraction experiments were performed with a Scintag automated diffractometer utilizing copper K_α radiation, which was continuously scanned over 30-80° 2θ at a rate of 1° per minute. Both the heat treated and heat treated + hydrogen charged conditions were investigated. Diffraction spectra of electrochemically charged plate were taken both at the charged surface and well into the specimen interior. The latter was achieved by sectioning and grinding.

RESULTS

Mechanical Testing - Influence of Constraint and Hydrogen

The maximum longitudinal stress increased and the corresponding plastic strain decreased with increasing level of constraint for uncharged PA 15-3 and 21S (Figure 2). The maximum longitudinal stress and plastic strain developed in PA 15-3 decreased almost linearly with hydrogen concentration. Ti-15Mo-3Nb-3Al, however, exhibited a sharp decrease in longitudinal stress and plastic strain at hydrogen concentrations greater than approximately 1000 wt. ppm. The threshold hydrogen concentration required to produce the distinct decrease is a function of constraint. Similarly, larger reductions in plastic strain occur for 21S at the highest constraint (Figure 2b). As reported previously, the fracture appearance of 21S at a constraint of 1.03 changed from a process completely governed by microvoid initiation, growth and coalescence to transgranular and intergranular separation processes with increasing hydrogen concentration[36]. In contrast, the fracture mode of PA 15-3 was relatively insensitive to hydrogen concentration as will be detailed below. Given the strong influence of constraint on the effects of internal hydrogen, SHT, PA and DA metallurgical conditions were investigated at the high constraint level of 1.43.

Mechanical Testing - Influence of Heat Treatment

Solution heat treated alloys were tested over a total hydrogen concentration range extending from the as-received levels to almost 3000 wt. ppm at the highest constraint level investigated

(1.43). The failure stress and strain of 15-3 are unaffected by hydrogen concentrations up to 3000 wt. ppm as shown in Figure 3. In contrast, 21S is embrittled at less than 3000 wt. ppm (Figure 3). Although the maximum longitudinal stresses are nearly equal for each alloy in the SHT condition, 15-3 displays approximately twice the plastic strain at maximum load as 21S for low hydrogen concentrations and more than five times the plastic strain at the hydrogen concentration of 2900 wt. ppm. It should be noted that the difference in the hardness of the two alloys is only slight in the solution heat treated condition as shown in Table 1.

In the PA condition (Fig. 4), both 15-3 and 21S exhibit a decrease in strength and ductility above approximately 1000 wt. ppm total hydrogen. This decrease is more pronounced for 21S as is the change in fracture mode which will be discussed below. Again, Table 1 indicates that the 21S alloy is of only slightly greater hardness than the 15-3 alloy.

Duplex Aged 15-3 also exhibits greater resistance to hydrogen embrittlement than DA 21S at equivalent total hydrogen concentrations (Fig. 5). Embrittlement is observed at hydrogen concentrations of approximately 1000 wt. ppm or greater. Comparison of material at equivalent hardness levels (as in the case of DA 15-3 at Rockwell C 41.4 versus PA 21S at Rockwell C 42.1) clearly shows that 15-3 still exhibits superior resistance to hydrogen embrittlement.

Fractography

All fractography reported was examined at approximately equivalent radial distances from the notch surface. The fracture mode of SHT 15-3 was relatively insensitive to hydrogen concentration. At all hydrogen levels investigated SHT 15-3 failed by transgranular microvoid processes. In PA material, the fracture mode of transgranular 15-3 was also transgranular microvoid coalescence at all constraint and hydrogen levels investigated. One effect of increasing hydrogen and constraint for the 15-3 alloy was to increase the density of microvoids per given fracture area and decrease the depth and width of the microvoids. Such a trend has also been associated with decreased fracture toughness of Beta III, but as a function of aging time[10]. The fracture mode of DA 15-3 also consisted of progressively finer microvoids up to its highest hardness (Rockwell C 41) and hydrogen concentration (3793 ppm H) where the fracture mode changed to transgranular ductile tearing characterized by fine undetermined features as shown in Figure 6.

In contrast to 15-3, the fracture modes of the SHT, PA and DA 21S alloys all changed significantly as the hydrogen concentration was increased (Fig. 7). The fracture mode of SHT 21S changed from large microvoids at approximately 100 ppm hydrogen, the as-received hydrogen concentration (Fig. 7a), to small microvoids and ductile tearing features at 680 ppm hydrogen (not shown). At 3000 ppm a flat fracture appearance characterized by three distinct fracture modes was observed: (1) fine voids and tearing features similar to the 680 ppm hydrogen level, (2) flat transgranular fracture, and (3) transgranular fracture displaying relatively straight parallel markings (Fig. 7b). These parallel markings typically extend across an entire grain diameter and are consistent with hydrogen induced slip band fracture which has been observed in hydrogen charged bcc steels, pure nickel, and nickel and iron base alloys[43-46]. The transgranular surfaces of other grains intercepting the surface contained almost entirely the fractures modes described by (1) and (2) above. The difference in fracture mode between individual grains is believed to be caused by differences in slip system orientation relative to the tensile axis.

The fracture mode in PA 21S is strongly influenced by both level of constraint and hydrogen concentration as detailed elsewhere[36]. At the highest constraint levels, peak aged 21S exhibits a transgranular microvoid fracture appearance with a bimodal distribution of dimple sizes in the

uncharged condition. This changed to a mixture of intergranular and transgranular fracture as hydrogen concentration is increased (Fig. 7c). The flat featureless areas of the PA 21S at 4664 ppm hydrogen (Fig. 7d) suggest that slip plane decohesion has occurred. However, this hypothesis requires crystallographic confirmation.

Duplex aged 21S fails by transgranular fracture with approximately 10 μm wide irregular terraces at 75 ppm hydrogen, the as-received level. Flat transgranular fracture characterized by parallel arrays of ridges containing micro-voids is observed across entire grains at 3800 ppm (Fig. 7e). Cleavage (Fig. 7f) apparently occurs at 5600 ppm as evidenced by a flat transgranular fracture appearance with markings.

Deformation Mode

Compression tests on SHT alloys revealed that both alloys are prone to highly localized planar slip at low plastic strains (3%) while at strains on the order of 8%, extensive multiple or wavy slip occurred in 15-3 but not in 21S. In contrast, localized planar slip persists in the SHT 21S material. Figure 8a and b compares the surface slip observed in SHT 15-3 and 21S at approximately 8% plastic strain and illustrates the difference.

X-ray Diffraction

Analysis of x-ray diffraction (XRD) data was undertaken for both peak aged 21S and 15-3. A β phase lattice parameter of 0.325 nm was determined for uncharged 21S ($\approx$75 $\pm$ 25 ppm), 0.328 for 24 hour charging ($\approx$1400 $\pm$ 400 ppm) and 0.331 nm for 64 hour charging ($\approx$2600 $\pm$ 800 ppm) using the (110) reflection. These results suggest partitioning of hydrogen to the β phase. In contrast, very little change in the *hcp* α phase lattice parameter is observed. Paton et al. also correlated β lattice parameter to hydrogen concentration in solution annealed Ti-18 Mo[47]. Lattice parameters equal to 0.328 and 0.331 nm were obtained at 1000 and 2100 ppm hydrogen, respectively, in good agreement with the data presented here. No evidence of hydriding of the β phase was found. Regarding the possibility of hydriding of α precipitates, x-ray diffraction analysis was conducted on (a) specimen surfaces, (b) several micrometers beneath the specimen surface, and (c) at a position as near as possible to the centerline of the notched region of a high constraint, high hydrogen tensile bar. The latter two conditions were achieved by surface grinding and sectioning, respectively. Neither α nor β phase hydride formation were detected at (a), (b) or (c) for charged and plastically strained PA 21S. Instead, diffraction peaks coinciding with the α and β phases are observed, except for immediately at the charged surface where neither the α phase nor its corresponding hydride are observed (Figure 9a). Electron microscopic examination revealed that selective removal of the α phase occured due to spalling of the near surface α precipitates (Fig. 9b). Such spalling might be expected based on the 18% volume increase which occurs upon hydriding of the α phase[27,47]. Spalling of hydrided α phase has previously been reported by Nakasa in Ti-6Al-4V during electrochemical hydrogen charging[48]. To confirm the notion that surface α could be hydrided under the electrochemical conditions used here, commercially pure Ti was charged under identical conditions used for Ti-15Mo-3Nb-3Al. Hydride formation was indeed confirmed by XRD and metallography.

Diffraction spectra taken from the surface of as-charged PA 15-3 indicated that surface exposed α also became hydrided but did not spall (Fig. 10). Hydriding appears to be a phenomena associated with surface exposed α for both alloys since no hydride peaks were detected in the

interior of either material when diffraction spectra were taken after serial grinding of the hydrogen charged surface. Instead, partitioning of hydrogen to the β phase is again observed as indicated by increases in the β lattice parameter. However, this does not preclude the possibility of localized deformation assisted hydriding in slip bands or localized hydriding of α/β interfaces as discussed by Boyd[49], if the volume fraction of hydride formed was too small for detection by XRD. To summarize, our findings suggest that hydriding of α precipitates occurs at the free surface but that hydriding of a large volume fraction of the subsurface α does not occur due to partitioning of hydrogen to the high solubility β phase.

DISCUSSION

Metallurgical factors affecting embrittlement susceptibility

Both preferential grain boundary α precipitation and localized planar slip can be circumstantially correlated with the greater susceptibility to internal hydrogen embrittlement (IHE) of the Ti-15Mo-3Nb-3Al alloy. Recall that preferential grain boundary α precipitation was noted in aged 21S (Fig. 1a) and intergranular cracking occurred (Fig. 7c). Planar slip was observed for SHT 21S (Fig. 8b) and is suggested by the fracture appearances in SHT (Fig 7b) as well as aged 21S (Fig. 7e). In contrast, wavy slip was observed in SHT 15-3, intragranular α precipitation was observed in aged 15-3 and transgranular fracture occurred. At issue are the important factors.

It is difficult to attribute the hydrogen embrittlement susceptibility of 21S exclusively to the mere presence of grain boundary α in the aged condition for two reasons. Firstly, aged 15-3 contained a 0.1 μm thick α film along β grain boundaries, although preferential formation of α colonies perpendicular to boundaries did not occur. The thin α film did not render the alloy susceptible. Secondly, 21S was more susceptible than 15-3 in the SHT condition where a solid solution β microstructure was preserved upon cooling from above the β transus. The parallel, linear features shown on the fracture surfaces of hydrogen charged 21S in the SHT and DA conditions (Figures 7b and 7e) and previously observed in hydrogen charged PA material[36] suggest an interaction between hydrogen, slip and fracture mode.

In the present study, planar slip has been observed for SHT 21S but not yet confirmed for aged 21S. However, it is reasonable to expect that aging would exacerbate the planar slip tendency seen in the SHT condition since (a) α plates are fine and, perhaps, shearable, (b) well aligned α colonies at grain boundaries might promote shearing, and (c) TEM/electron diffraction experiments show that both 15-3 and 21S exhibit Burger's α (i.e. $(110)_\beta \parallel (0001)_\alpha$, $[111]_\beta \parallel [11\bar{2}0]_\alpha$)[51]. This suggests that transfer of slip from β to α may be possible and also that shearing of α precipitates may occur. In support of this view, Okada, Banerjee, and Williams found that slip transfer from β to α was a function of precipitate morphology in Ti-15V-3Cr-3Al-3Sn[52]. Slip initiates in the β phase and parallel α plates of the same variant (colony type structure) allow dislocations to shear the α phase while α plates of differing physical orientations promote homogeneous slip[52]. High magnification SEM of aged, metallographically prepared 21S and 15-3 show a difference in the size and physical orientation of α plates for the two alloys[37]. It is plausible that the coarseness of intragranular α in aged 15-3, which has nucleated first and grown for a longer time, is a more effective slip barrier than the fine α of 21S. A greater impedance to planar slip would promote more homogeneous deformation in the form of multiple or wavy slip in aged alloys.

Hydrogen segregation to dislocations and transport by slip is well documented in *bcc* metals[53,54]. Recall that hydrogen has been shown to partition to and is relatively mobile in the

bcc lattice[36,55] which provides a readily available source for hydrogen pickup by dislocations and possible deposition of this hydrogen at grain boundaries. In the case of 15-3, which appears more prone to wavy or multiple slip, we hypothesize that less hydrogen is transported to β grain boundaries and the locally high hydrogen concentrations possible along the intense planar slip bands seen in 21S (Fig. 8b) are avoided. In this way slip mode would also contribute to the observation of intergranular cracking in 21S. This explanation for intergranular cracking is well supported by the fracture modes observed for 21S but not found for 15-3 in this study and is consistent with the work of Albrecht, Thompson, and Bernstein in aluminum alloys[56-59].

Ti-15Mo-3Nb-3Al, which is prone to planar slip, undergoes slip band, possibly slip plane, intergranular, and cleavage cracking depending on microstructure, degree of constraint and hydrogen concentration. 15-3, in which multiple slip is easier to induce, exhibits a microvoid rupture fracture mode until the highest strength and hydrogen level investigated where the fractographic features are on the size and order of the deformation structure seen in heavily plastically strained SHT material as shown by a comparison of Figures 6b and 8a. Correlation of the different fracture modes with the plastic slip behavior exhibited by each alloy indicate that deformation mode strongly influences the hydrogen effected fracture paths and subsequent mechanical properties. Consequently, factors influencing slip behavior should be reviewed. It is reasonable to expect that slip behavior in *bcc* titanium is dependent on both alloy composition, thermo-mechanical processing, and precipitate morphology as in the case of other alloy systems. For SHT β alloys it is plausible that deformation mode may be controlled by chemical composition, operative slip or twinning systems, and residual dislocation density since other factors affecting slip such as the ω phase were not detected, nor expected. The fact that alloying additions affect stacking fault energy and subsequent slip behavior is well known and also may apply to metastable β-titanium alloys. Ling and co-workers noted a changed in deformation mode from wavy, multiple slip in a quenched and recrystallized Ti-28 wt. % V alloy to coarse planar slip in a 40 wt. % V alloy[60]. They traced the difference to an increasing twin fault probability with increasing V which makes cross-slip more difficult[61]. In the present study, the equivalent Mo concentration of 15-3 is 11.9 wt. % while that of 21S is 12.8%, not a large difference. Therefore, we assert that differences in deformation mode observed here are more dependent on heat treatment than alloy composition. In support of this view it should be noted that preferential grain boundary α precipitation and intergranular stress corrosion cracking have been produced in 15-3 which was solution heat treated above the β transus for longer times (e.g. 1038°C, 2 hours) than investigated here[37,50]. The present authors have also produced intergranular cracking in re-solutionized 15-3 (816°C, 0.5 h→Air cool, 950°C, 12 h→Air cool) with room temperature hydrogen charging[62]. Of important note, this condition was also more prone to planar slip than SHT 15-3 after 816°C for 0.5 h[62]. Therefore, solution heat treatment temperature and time appear to affect both slip behavior and α precipitation in 15-3 and 21S more strongly than compositional differences.

The temperature and time associated with solution heat treatments (Table 1) affect residual dislocation density, vacancy concentration, and grain growth. Since minimal grain growth was observed vacancy concentration and dislocation density are implicated as key factors. Fujii has shown that a high excess vacancy concentration created by very high SHT temperatures (i.e. >1000°C) and a low density of vacancy sinks (grain boundaries, twin boundaries and dislocations) accelerate aging and promotes fine homogeneous α precipitation[63]. However, a balance exists between the opposing roles of dislocations as vacancy sinks and as heterogeneous α nucleation sites[63]. Dislocations remaining from prior working clearly readily serve as strong α nucleation sites as shown by studies of the effect of cold work on aging[63,64]. In this study, the differences in excess

vacancy concentration following heat treatment at 816, 871 or 950°C are probably minor. However, long solutionizing times at 871°C (21S: 8h) and 950°C (Re-solution heat treated 15-3: 12h) are likely to lower dislocation density, given temperatures of about one-half the melting temperature. We speculate that residual dislocation substructure is a dominate factor affecting slip mode and aging behavior in the present study and that composition and vacancies play secondary roles. Solution treatment has also been identified as the controlling factor in hot salt stress corrosion cracking susceptibility of the metastable β alloy Beta-III but the mechanism of embrittlement was not discussed[38]. In the present study, solution treatment time and temperature are implicated as important factors affecting the internal hydrogen embrittlement (IHE) susceptibility of β-titanium alloys.

Other factors possibly affecting embrittlement susceptibility

Two other important differences have been reported for Ti-15V-3Cr-3Al-3Sn and Ti-15Mo-3Nb-3Al that pertain to hydrogen embrittlement susceptibility. Pound reports that the high apparent hydrogen trapping constant associated with 21S predicts a greater trapping tendency upon aging than observed for aged 15-3[65]. The materials analyzed were identical to those used in the present study. The controlling trap site is circumstantially identified as α/β interfaces, in particular it is speculated, those associated with grain boundary α colonies[65]. The trap strength of α/β interfaces may depend on coherency and lattice misfit. In general, coherent interfaces are viewed as reversible hydrogen trap sites that rely on local stress state and dislocations to promote trapping[66]. Incoherent interfaces are often regarded as irreversible trap sites and also have lower cohesive strengths[66]. Interestingly, hydrogen alters the β lattice parameter but minimally influences the α lattice parameter[67] and this may change the misfit strain of coherent interfaces. It is unclear whether or not differences exist between the intragranular and grain boundary α/β interface structures, or whether differences exist in the case of 21S relative to 15-3. Recall that a Burger's orientation relationship is found between the β matrix and α plates in both 21S and 15-3[51]. It is difficult to attribute the differences in IHE susceptibility between 15-3 and 21S solely to an intrinsic difference in the irreversible trap strength of α/β interfaces based on alloy composition alone, especially since (a) SHT 21S is more susceptible to IHE than SHT 15-3 even in the absence of α precipitates, (b) re-solution heat treated 15-3 is prone to IHE and re-solution heat treated and aged 15-3 is rendered susceptible to SCC[37], and (c) irreversible trapping at α/β interfaces does not account for many of the fracture paths reported in the present study. It is also difficult to attribute the difference in susceptibility exclusively to the presence of boundary α, since aged 15-3 contained a 0.1 μm α film but did not crack intergranularly in aqueous testing[37] or hydrogen.

The second factor worth mentioning is the affect of hydrogen on the ductile to brittle transition temperature (DBTT) for the β matrix[1,67]. Lederich reports a 50°C difference in DBTT for 15-3 versus 21S, with 21S experiencing the higher of the two transition temperatures at a given β phase hydrogen concentration[67]. Calculations show[62] that it is unlikely that the DBTT has been shifted above room temperature for either of the two alloys in the present study. This conclusion is reached even after taking into consideration a correction in hydrogen concentration due to hydrogen partitioning in the β matrix of β+α Ti microstructures[62]. β phase hydrogen concentrations of 5333 and 7586 wt. ppm would be required to raise the DBTT above 25°C for 21S and 15-3, respectively. Only in the case of DA 21S at 5600 wt. ppm total hydrogen (Figure 7f) is cleavage induced by a high DBTT suspected. Consequently, we conclude that this particular intrinsic difference between 15-3 and 21S is not the operative reason for the susceptibility of 21S

over the range of hydrogen concentrations reported in the present study.

Correlations with aqueous stress corrosion cracking

Hydrogen has previously been suggested as the embrittling species in aqueous chloride testing of PA β titanium alloys[10,11]. Hydrogen-slip interactions may explain the superior SCC resistance of PA 15-3 vs. PA 21S in aqueous sodium chloride solution[11,37]. L. Young and Gangloff have suggested that dislocation motion is a requisite for EAC in 21S based on J-integral resistance curve testing conducted at varying load-line displacement rates and "ripple" loaded tests of PA 15-3 and 21S in aqueous saltwater[37]. This statement fits well with the observations made in this paper. Consider the production of hydrogen at an acidified crack tip and absorption of this hydrogen into the fracture process zone. Under a "ripple" load designed to rupture the surface oxide film (but well below the fatigue ΔK threshold for crack growth in moist air) hydrogen enters the metal if elastic strains rupture the oxide film and diffuses through the lattice, partitioning primarily to the β phase where it is highly soluble. Localized planar slip band formation does not occur, however, below the moist air fatigue ΔK threshold.

Under a rising load test, however, where dislocation motion is occurring, hydrogen may be transported by dislocations and deposited at the dislocation sinks (i.e. grain boundaries) where it is trapped and promotes intergranular separation. The differences in the SCC resistance between 15-3 and 21S may also be traced to the tendency of 21S toward planar slip which promotes hydrogen transport over long distances to grain boundaries. Multiple or wavy slip, which has been shown to occur more readily in SHT 15-3 than 21S, hinders the transport and deposition of hydrogen to grain boundaries and concurrently disperses hydrogen as dislocations transport hydrogen to newly activated slip systems. Planar slip may also promote film rupture phenomena to stimulate hydrogen entry in aqueous SCC testing.

CONCLUSIONS

1. Hydriding of a large volume fraction of the α and β phases is not required for embrittlement to occur in β titanium alloy Ti-15Mo-3Nb-3Al. Reduction in the maximum longitudinal stress and plastic strain developed in solution annealed Ti-15Mo-3Nb-3Al at hydrogen concentrations < 3000 wt. ppm suggest that the β phase is intrinsically embrittled by hydrogen especially when deformation occurs by localized planar slip.

2. Embrittlement is a function of hydrogen concentration, constraint, and yield strength for alloys which have a susceptible microstructure. Susceptible microstructures are caused by high solution treatment temperatures and times which remove heterogeneous nucleation sites from grain interiors to promote grain boundary α, delay intragranular α precipitation and promote planar slip. In aged alloys fine α precipitates may be sheared by dislocations to promote planar slip, concentrate hydrogen along planar slip bands and transport hydrogen to grain boundaries.

3. The relationships between microstructure, deformation mode and speculated hydrogen transport behavior can account for the observed cracking in β titanium which was precharged with hydrogen and slowly strained in air as well as simultaneously polarized and slowly strained in aqueous chloride solution. This correlation supports a hydrogen embrittlement/dislocation transport mechanism for aqueous saltwater stress corrosion cracking of metastable β titanium alloys.

ACKNOWLEDGMENTS

This research was supported by the Office of Naval Research (Grant N00014-91-J-4164) with Dr. A. John Sedriks as Scientific Monitor and by the Virginia Center for Electrochemical Science and Engineering at the University of Virginia. The material used in this study was graciously donated by TIMET. The authors wish to acknowledge the invaluable assistance and discussions with R.P. Gangloff, B.P. Somerday, L.M. Young, K. Lawless and J.M. Howe.

REFERENCES

1. H.G. Nelson, "Hydrogen Environment Effects on Advanced Alloys and Composites in Aerospace Structures," pp. 301-311, (Charlottesville, VA: First Thermal Structures Conference, 1990).

2. P.J. Bania, G.A. Lenning and J. A. Hall, "Development and Properties of Ti-15V-3Cr-3Sn-3Al (Ti-15-3)," pp. 209-299, (Warrendale, PA: Beta Titanium Alloys in the 80's, 1983).

3. A.G. Hicks and H. W. Rosenberg, "Ti-15-3 Foil Properties and Applications," pp. 231-238, (Warrendale, PA: Beta Titanium Alloys in the 80's, 1983).

4. P.J. Bania and W.M. Parris, "BETA-21S: A High Temperature Metastable Beta Titanium Alloy," (Orlando, FL: Titanium Development Association International Conference, 1990).

5. T.W. Duerig and J.C. Williams, "Overview: Microstructure and Properties of Beta Titanium Alloys," pp. 19-67, (Warrendale, PA: Beta Titanium Alloys in the 80's, 1983).

6. R.J. H. Wanhill, British Corrosion J., 10(2)(1975): pp. 69-78.

7. M.J. Blackburn, J.A. Feeney, T.R. Beck, Stress Corrosion Cracking of Ti Alloys (New York, NY: Advances in Corrosion Science and Technology, 1972), pp. 67-292.

8. R.W. Schutz and D.E. Thomas, Corrosion of Titanium and Titanium Alloys (Metals Park, OH: Metals Handbook, 9th edition, Vol. 13, 1987), pp. 669-706.

9. D.N. Fager and W.F. Spurr, Trans. ASM, 61(1968): pp. 283-292.

10. J.A. Feeney, M.J. Blackburn, Metall. Trans., 1(1970): pp. 3309-3323.

11. L.M. Young, Environment Assisted Cracking in β-Titanium Alloys (Charlottesville, VA: Master's Thesis, 1993).

12. H.J. Bhatt, E.H. Phelps, Corrosion J., 17(1961): pp. 430t-434t.

13. B.E. Wilde, Corrosion J., 27(8)(1971): p. 326.

14. J.R. Scully, P.J. Moran, Corrosion J., 44(3)(1988): pp. 176-186.

15. R.P. Gangloff, "Corrosion Prev. and Control," pp. 64-111, (Watertown, MA: Proc. of the 33rd Sagamore Army Materials Research Conf.,1986).

16. D. Kolman, and J.R. Scully, Unpublished research, The University of Virginia, Charlottesville, VA, 1993.

17. T.R. Beck, Localized Corrosion (Houston, TX: NACE, 1974), pp. 644-652.

18. A.D. McQuillan, "An Experimental and Thermodynamic Investigation of the Hydrogen-Titanium System," pp. 309-323, (*Proceedings of the Royal Society of London*, Vol. A204, 1950).

19. M. Pourbaix, Atlas of Electrochemical Equilibria in Aqueous Solutions (Houston, TX: NACE, 1974).

20. B.F. Brown, C.T. Fujii, and E.P. Dahlberg, J. Electrochem. Soc., 116(1969): pp. 218-219.

21. J.J. DeLuccia, "Electrolytic Hydrogen Permeation in Beta Titanium," Report No. NADC-76297-30, Naval Air Development Center, 1976.

22. W.R. Holman, R.W. Crawford, F. Paredes, Jr., Hydrogen Diffusion in a Beta-Titanium Alloy, Trans. TMS-AIME, (233)(1965): pp. 1836-1839.

23. R.L. Schulte, P.N. Adler, "Stress Induced hydrogen Redistribution in High Purity Ti-31V Alloy," pp. 177-185, (Warrendale, PA: Hydrogen Effects in Metals, 1980).

24. K.N. Akhurst, T.J. Baker, Metall. Trans. A, 12A(1981): pp. 1059-1071.

25. N. Bandyopadhyay, J. Kameda, C.J. McMahon, Metall. Trans. A, 14A(1983): pp. 881-888.

26. D.S. Shih, and H.K. Birnbaum, Evidence of FCC Titanium Hydride Formation in β Titanium Alloy: An X-Ray Diffraction Study, Scripta Met., Vol 20(1986): pp 1261-1264.

27. W.W. Gerberich, N.R. Moody, C.L. Jensen, C. Hayman, and K. Jatavallabhula, "Hydrogen in α/β and all β Titanium Systems," pp. 731-745, (Warrendale, PA: Hydrogen Effects in Metals, 1981).

28. K. Nakasa and J. Liu, Bending Strength of Hydrogen Charged Ti-13V-11Cr-3Al Alloy (J.Japan Inst. Metals, Vol 55, No. 9(1991): pp. 922-927.

29. D.E. Thomas and S.R. Seagle, "Stress Corrosion Cracking Behavior of Ti-38-6-44 in Sour Gas Environments," Titanium Science and Technology, Vol. 4, pp.2533-2540, (1984).

30. M.J. Blackburn and W.H. Smyrl, Stress Corrosion and Hydrogen Embrittlement (New York, NY: Titanium Science and Technology, 1973), pp. 2577-2609.

31. H.G. Nelson, "Aqueous Chloride Stress Corrosion Cracking of Titanium - A Comparison with Environmental Hydrogen Embrittlement," pp.445-464, (Hydrogen in Metals, 1973).

32. N.E. Paton and O. Buck, "Effect of Hydrogen Behavior of Materials," pp. 83-89, (Warrendale, PA: 1975).

33. N.E. Paton, R.A. Spurling and C.G. Rhodes, pp.269-279, "Hydrogen Effects in Metals," pp. 269-279, (Warrendale, PA 1981).

34. J.E. Costa, D. Banerjee, and J.C. Williams, "Hydrogen Effects in β-Titanium Alloys," pp. 69-84, (Warrendale, PA: Beta Titanium Alloys in the 80's, 1983).

35. L. Wagner, J.K. Gregory, "Improvement of the Mechanical Behavior in Ti-3Al-8V-6Cr-4Mo-4Zr by Duplex Aging," pp. 199-209, (Denver, CO: Proc. of the TMS Beta-Titanium Symposium, TMS Annual Meeting, 1993).

36. G.A. Young Jr. and J.R. Scully, Effects of Hydrogen on the Mechanical Properties of a Ti-Mo-Nb-Al Alloy, Scripta Met., (28)(1993): pp. 507-512.

37. L.M. Young, G.A. Young, Jr., J.R. Scully, R.P. Gangloff, "Aqueous Environment Enhanced Crack Propagation in

High Strength Beta-Titanium Alloys," in review, Metall. Trans., 1993.

38. J.B. Guernsey, V.C. Petersen, and F.H. Froes, Discussion of Effect of Microstructure on the Strength, Toughness, and Stress-Corrosion Cracking Susceptibility of a Metastable β Titanium Alloy, Met. Trans. A, (3)(1972): pp. 339-340.

39. Z.A. Foroulis, "Factors Affecting Absorption of Hydrogen in Titanium from Aqueous Electrolytic Solutions," pp. 2705-2711, (Warrendale, PA: Ti'80, Science and Technology, 1980).

40. P.W. Bridgman, Studies in Large Plastic Flow, McGraw-Hill Inc.(1952): pp. 9-37.

41. J.W. Hancock and A.C. Mackenzie, On the Mechanisms of Ductile Failure in High-Strength Steels Subjected to Multi-Axial Stress-States, J. Mech. Phys. Solids, (24)(1976): pp. 147-169.

42. A.C. Mackenzie, J.W. Hancock and D.K. Brown, On the Influence of State of Stress on Ductile Failure Initiation in High Strength Steels, Engineering Fracture Mechanics, (9)(1977): pp. 167-188.

43. J. Eastman et al., "Hydrogen Effects in Nickel--Embrittlement or Enhanced Ductility," Hydrogen Effects in Metals, pp. 397-409, (The Metallurgical Society of AIME, 1980).

44. R.E. Stoltz and A.J. West, "Hydrogen Assisted Fracture in FCC Metals and Alloy," Hydrogen Effects in Metals, pp. 541-553, (The Metallurgical Society of AIME, 1980).

45. N.R. Moody and F.A. Greulich, Hydrogen Induced Slip Band Fracture in an Fe-Ni-Co Superalloy, Scripta Met., (19)(1985): pp. 1107-1111.

46. N.R. Moody, R.E. Stolts, and M.W. Perra, The Effect of Hydrogen on Fracture Toughness of the Fe-Ni-Co Superalloy IN903, Met Trans A, (18A)(1987): pp. 1469-1482.

47. N.E. Paton, O. Buck, J.C. Williams, Scripta. Met., 2(1978): p. 669.

48. K. Nakasa and J. Liu, Surface Peeling of Ti-6Al-4V Alloy Specimens during Hydrogen Charging, J. Japan Inst. Metals, 54 (11)(1990): pp. 1261-1269.

49. J.D. Boyd, Precipitation of Hydrides in Titanium Alloys, Trans ASM, (62)(1969): pp. 977-988.

50. D.A. Meyn and P.S. Pao, "Slow Strain Rate Testing of Precracked Titanium Alloys in Salt Water and Inert Environments", Slow Strain Rate Testing: Research and Engineering Applications, ASTM STP 1210, R. Kane, ed., ASTM 1993.

51. K.R. Lawless, Unpublished Research, The University of Virginia, Charlottesville, VA, 1993.

52. M. Okada, D. Banerjee, and J.C. Williams, "Tensile Properties of Ti-15-V-3Al-3Cr-3Sn Alloy," pp. 1835-1842, (Titanium Science and Technology, 1980).

53. J.P. Hirth, Effects of Hydrogen on the Properties of Iron and Steel, Met Trans A,(11A)(1980): pp. 861-890.

54. C.J. MacMahon Jr., "Effects of Hydrogen on Plastic Flow and Fracture in Iron and Steel," Hydrogen Effects in Metals, pp. 219-233,(The Metallurgical Society of AIME, 1980).

55.R.L. Shulte and P.N. Adler, "Stress-Induced Hydrogen Redistribution in High Purity Ti-31V Alloy," Hydrogen Effects in Metals, pp. 177-185, (The Metallurgical Society of AIME, 1980).

56. J.K. Tien et al., Hydrogen Transport by Dislocations, Met. Trans. A, (7A)(1976): pp. 821-829.

57. J. Albrecht, I.M. Bernstein, and A.W. Thompson, Evidence for Dislocation Transport of Hydrogen in Aluminum, Met. Trans. A, (13A)(1982): pp. 811-820.

58. D.A. Hardwick, A.W. Thompson, and I.M. Bernstein, The Effect of Copper Content and Microstructure on the Hydrogen Embrittlement of Al-6Zn-2Mg Alloys, Met.Trans. A, (14A)(1983): pp. 2517-2526.

59. D. Nguyen, A.W. Thompson, and I.M. Bernstein, Microstructural Effects on Hydrogen Embrittlement in a High Purity 7075 Aluminum Alloy, Acta Met., (35) 10(1987): pp. 2417-2425.

60. F.W. Ling, E.A. Starke, Jr., and B.G. LeFevre, Metall. Trans., 5(1974): pp. 179-187.

61. F.W. Ling, H.J. Rack, E.A. Starke, Jr., Metall. Trans., 4(1973): pp. 1671-1676.

62. G.A. Young, Jr., Hydrogen Effects in Metastable Beta Titanium Alloys (Charlottesville, VA: Master's Thesis, 1993).

63. H. Fujii, H.G. Suzuki, "Effect of Solution Treatment Conditions on Aging Response," pp. 249-259, (Beta Titanium Alloys in the 1990's, 1993).

64. M.A. Imam, P.K. Poulose, B.B. Rath, "Modification of Alpha Phase Precipitation by Cold Work of the Ti-15-3 Alloy," pp.261-271, (Beta Titanium Alloys in the 1990's, 1993).

65. B.G. Pound, "Evaluation of a Diffusion/Trapping Model for Hydrogen Ingress in High Strength Alloys," SRI Report PYU-2969, October, 1993.

66. G.M. Pressouyre, Metall. Trans., 10A(1979): p. 1571.

67. R.J. Lederich, D.S. Schwartz, S.M.L. Sastry, "Effects of Internal Hydrogen on Microstructures and Mechanical Properties of β21S and Ti-15-3," pp. 159-169, (Beta Titanium Alloys in the 1990's, 1993).

List of Figures

Table 1. β-titanium alloy heat treatments and corresponding Rockwell C hardness values. Alloys were received in the SHT condition with the reported solution heat treatment temperatures and times.

Condition: Alloy	Heat Treatment	HRC
Solution Annealed:		
Ti-15V-3Cr-3Al-3Sn	816°C, 0.5 h → Air Cool	25.2 ± 0.9
Ti-15Mo-3Nb-3Al	871°C, 8 h → Air Cool	28.7 ± 1.2
Peak Aged:		
Ti-15V-3Cr-3Al-3Sn	538°C, 8 h → Air Cool	38.9 ± 0.6
Ti-15Mo-3Nb-3Al	538°C, 8 h → Air Cool	42.1 ± 1.2
Duplex Aged:	440°C, 20 h → Air Cool →	41.4 ± 0.7
Ti-15V-3Cr-3Al-3Sn	538°C, 0.5 h → Air Cool	
Ti-15Mo-3Nb-3Al	440°C, 20 h → Air Cool →	48.8 ± 0.8
	538°C, 0.5 h → Air Cool	

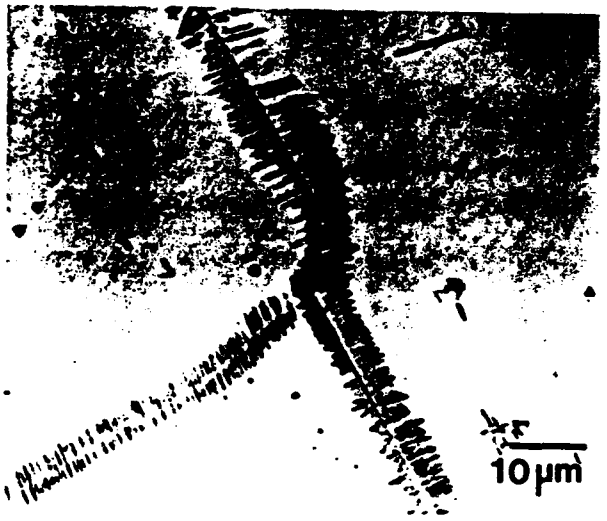

Figure 1a. Optical micrograph showing the β+α microstructure of Ti-15Mo-3Nb-3Al after aging for 1 hour at 538°C.

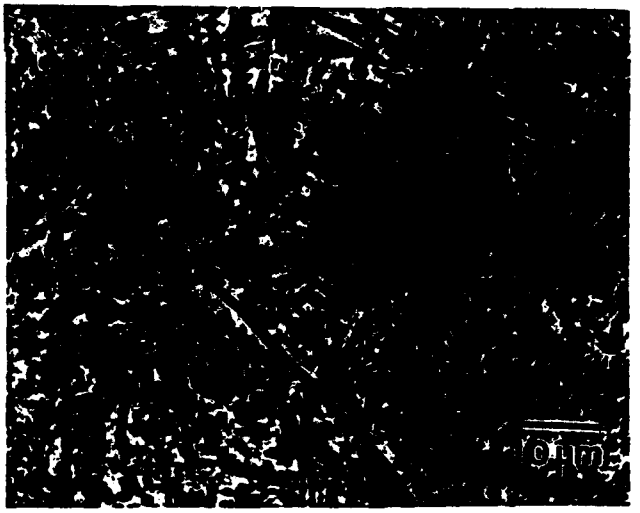

Figure 1b. Optical micrograph showing the β+α microstructure of Ti-15V-3Cr-3Al-3Sn after aging for 1 hour at 538°C.

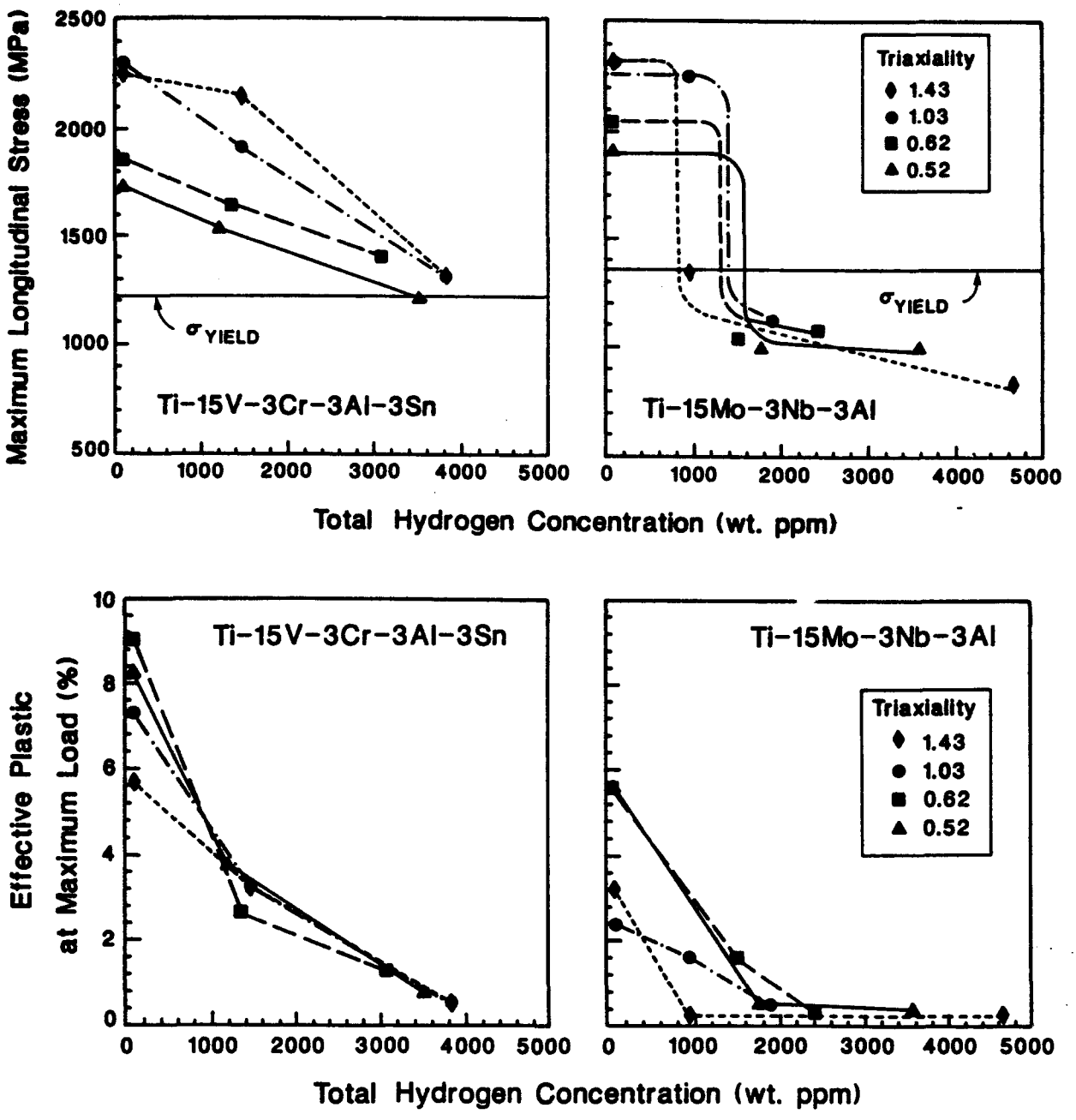

Figure 2. The effects of constraint and total internal hydrogen concentration on the maximum longitudinal stress and effective plastic strain developed in peak aged Ti-15V-3Cr-3Al-3Sn and Ti-15Mo-3Nb-3Al. σ_{YIELD} is the uniaxial yield strength.

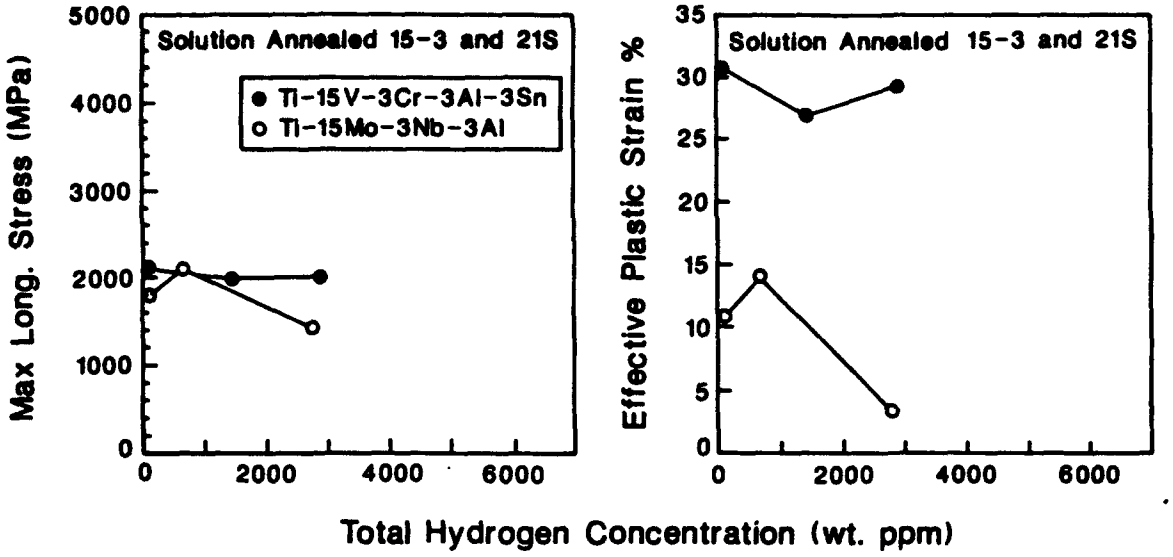

Figure 3. The effect of total internal hydrogen concentration on maximum longitudinal stress and effective plastic strain developed in solution heat treated Ti-15V-3Cr-3Al-3Sn and Ti-15Mo-3Nb-3Al.

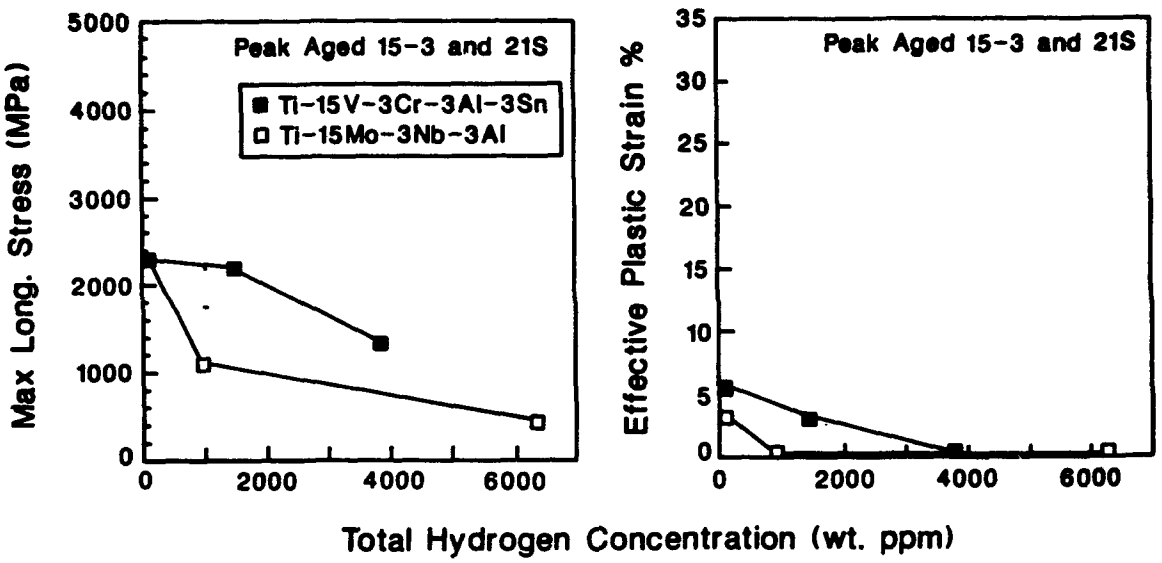

Figure 4. The effect of total internal hydrogen concentration on maximum longitudinal stress and effective plastic strain developed in single step peak aged Ti-15V-3Cr-3Al-3Sn and Ti-15Mo-3Nb-3Al.

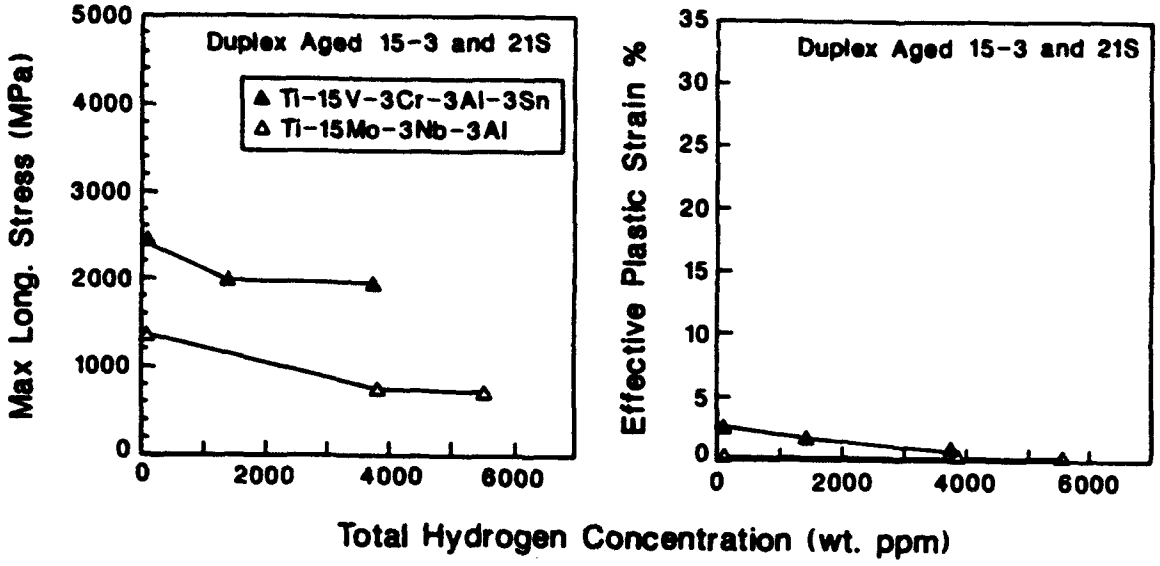

Figure 5. The effect of total internal hydrogen concentration on maximum longitudinal stress and effective plastic strain developed in duplex aged Ti-15V-3Cr-3Al-3Sn and Ti-15Mo-3Nb-3Al.

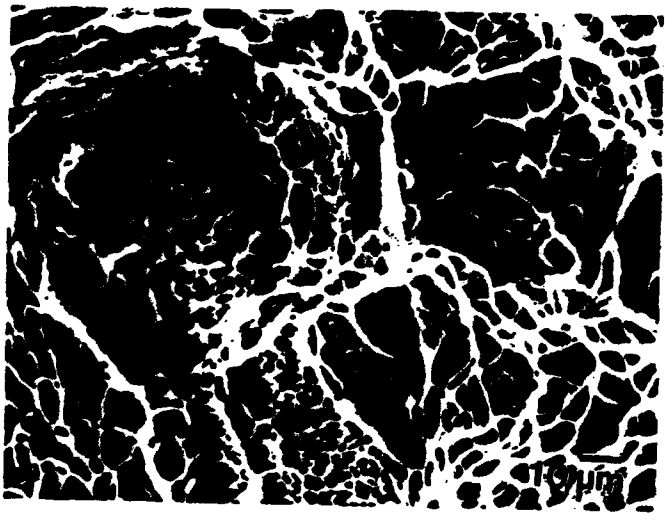

Figure 6a. Fracture surfaces from Ti-15V-3Cr-3Al-3Sn at a constraint level of 1.43 under solution heat treated conditions at the uncharged hydrogen level of 90-120 wt. ppm hydrogen.

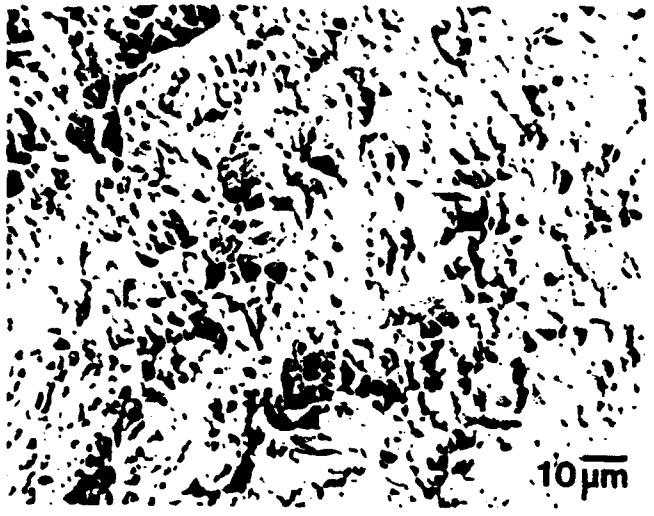

Figure 6b. Fracture surfaces from duplex aged Ti-15V-3Cr-3Al-3Sn at a constraint level of 1.43 with 3700 wt. ppm hydrogen.

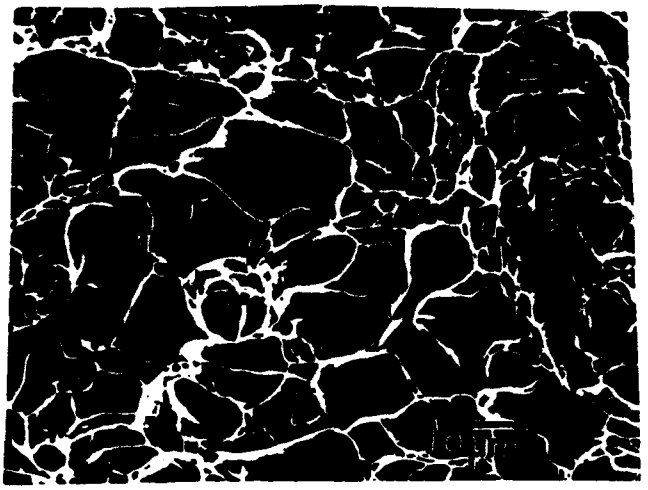

Figure 7a. Fracture mode produced in Ti-15Mo-3Nb-3Al at a constraint level of 1.43: solution heat treated - 100 wt. ppm hydrogen.

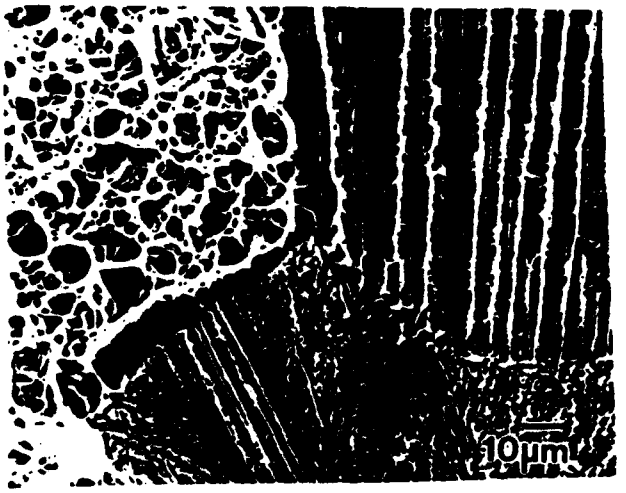

Figure 7b. Fracture mode produced in Ti-15Mo-3Nb-3Al at a constraint level of 1.43: solution heat treated - 3000 wt. ppm hydrogen.

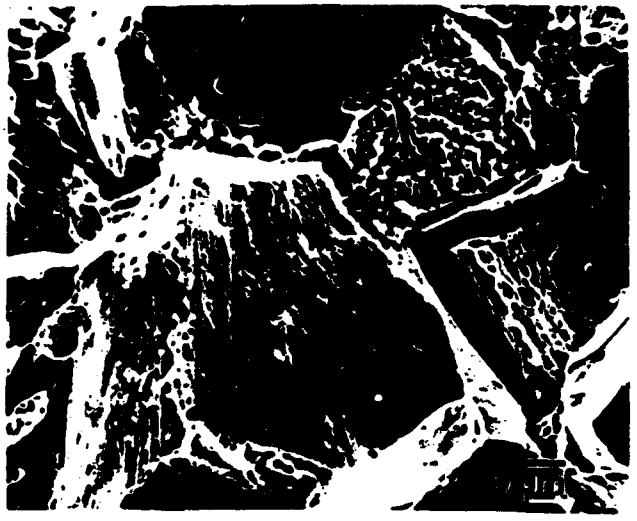

Figure 7c. Fracture modes produced in Ti-15Mo-3Nb-3Al at a constraint level of 1.43: peak aged - 1000 wt. ppm hydrogen.

Figure 7d. Fracture modes produced in Ti-15Mo-3Nb-3Al at a constraint level of 1.43: peak aged - 3500 wt. ppm hydrogen.

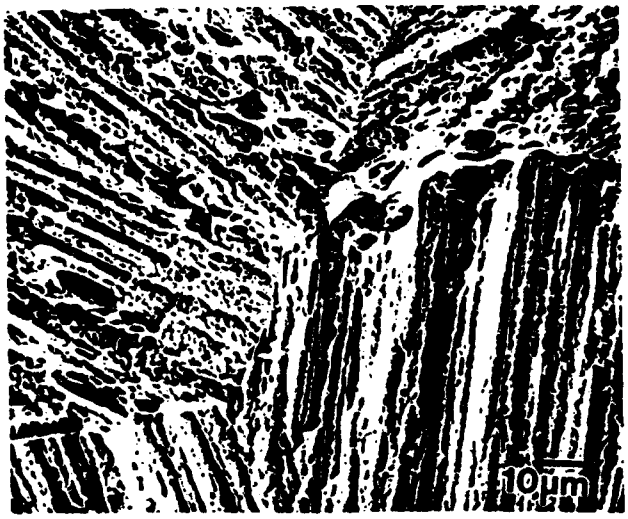

Figure 7e. Fracture modes produced in Ti-15Mo-3Nb-3Al at a constraint level of 1.43: duplex aged - 3800 wt. ppm hydrogen.

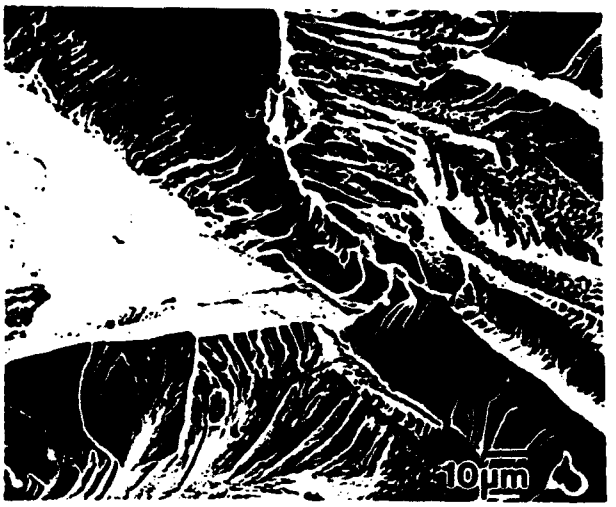

Figure 7f. Fracture modes produced in Ti-15Mo-3Nb-3Al at a constraint level of 1.43: duplex aged - 5600 wt. ppm hydrogen.

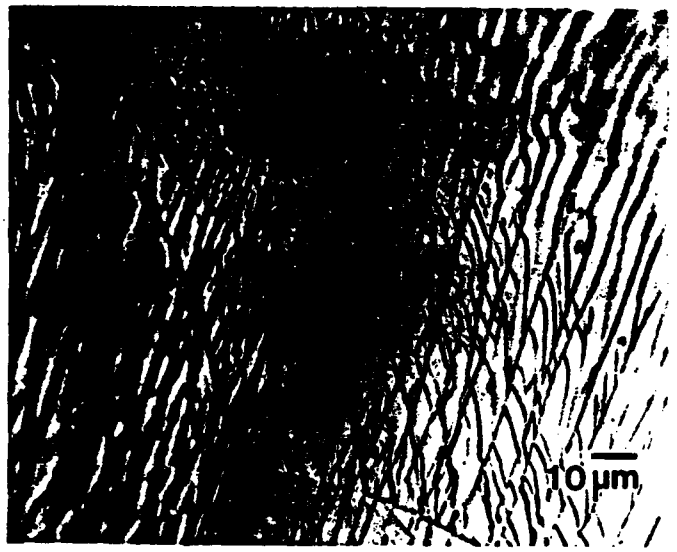

Figure 8a. Surface slip lines observed in solution heat treated Ti-15V-3Cr-3Al-3Sn deformed to approximately 8% plastic strain in compression.

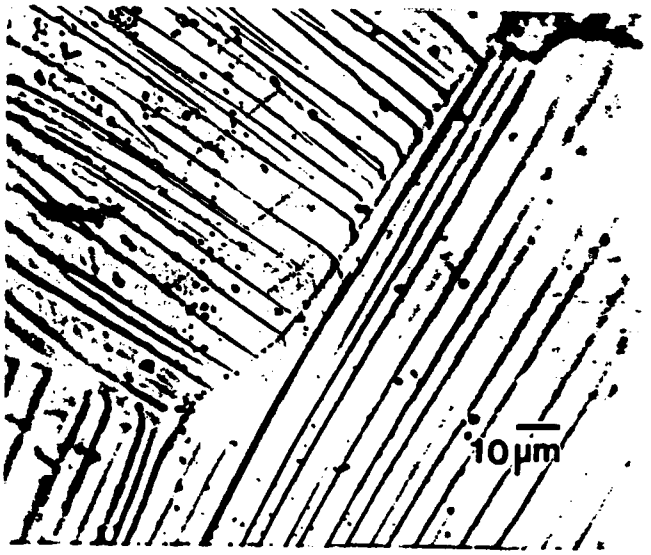

Figure 8b. Surface slip lines observed in solution heat treated Ti-15Mo-3Nb-3Al deformed to approximately 8% plastic strain in compression.

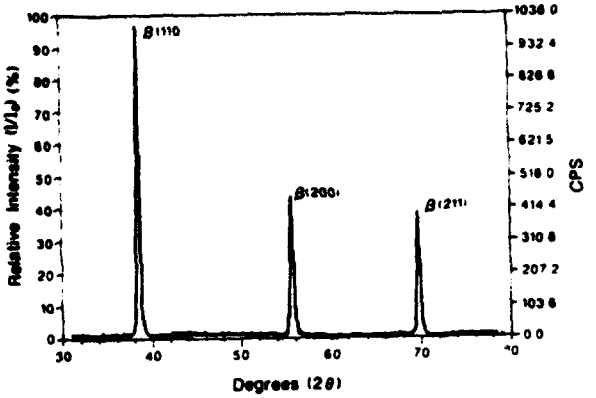

Figure 9a. Diffraction spectra from the surface of peak aged Ti-15Mo-3Nb-3Al charged 64 hours in H_2SO_4 solution at 90°C.

Figure 9b. SEM micrograph of the charged peak aged Ti-15Mo-3Nb-3Al surface illustrating the spalled surface exposed secondary α phase.

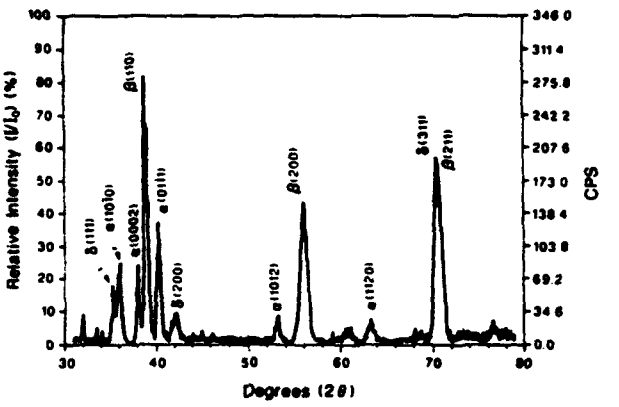

Figure 10. Diffraction spectra taken from the surface of PA Ti-15V-3Cr-3Al-3Sn, charged 24 hours showing the α, β, and δ phase peaks.

ELECTROCHEMISTRY AND PASSIVITY OF A Ti-15Mo-3Nb-3Al BETA-TITANIUM ALLOY IN AMBIENT TEMPERATURE AQUEOUS CHLORIDE SOLUTIONS

D. G. Kolman
J. R. Scully

Electrochemistry and Passivity of a Ti-15Mo-3Nb-3Al Beta-Titanium Alloy in Ambient Temperature Aqueous Chloride Solutions

D. G. Kolman* and J. R. Scully**

Center for Electrochemical Science and Engineering, Department of Materials Science, University of Virginia, Charlottesville, Virginia 22903.

ABSTRACT

To understand the effect of Mo-Nb additions on the electrochemical behavior of β-titanium alloys in ambient temperature chloride solutions, characterization of the electrochemistry and passivity of a Ti-15Mo-3Nb-3Al alloy (β-21S) was undertaken. Both solution heat-treated (SHT) and peak-aged (PA) alloys exhibited passive anodic behavior in aerated and deaerated 0.6*M* NaCl, aerated and deaerated 0.6*M* NaCl adjusted to pH 1 with HCl, as well as aerated 5*M* HCl. X-ray photoelectron spectroscopy (XPS) performed after exposure to neutral 0.6*M* NaCl indicated that both PA and SHT β-21S formed a predominantly TiO_2 film. Auger electron spectroscopy (AES) and cathodic kinetics suggest that the Mo and Nb alloying additions are incorporated into the oxide in amounts less than that found in the alloy. The predominance of the passivating TiO_2 may explain the similarity of the electrochemical behavior observed. However, in deaerated 5*M* HCl, all materials displayed active-passive behavior except for SHT β-21S which was spontaneously passive. This result suggests that the presence of the α-phase is deleterious to the formation of a protective passive film on PA β-21S in deaerated 5*M* HCl.

Metastable β-titanium alloys incorporating Mo and Nb, such as β-21S, were designed initially for improved high temperature properties such as oxidation resistance, elevated temperature strength, and creep resistance.[1] However, interest in these materials for high strength applications in room temperature marine environments is increasing. One question regarding their seawater performance is their resistance to environmentally assisted cracking (EAC). The EAC resistance of α-titanium alloys in seawater is controlled by the tendency of the α-phase to hydride.[2,3] In α + β alloys, a discontinuous β-phase has a positive effect on the EAC resistance, plastically blunting cleavage cracks propagating through the hydrided α-phase.[4] Little is known about the effects of α-phase in a β-titanium matrix, however a continuous β-phase is detrimental to hydrogen embrittlement resistance.[5] In contrast to α-titanium, a large hydrogen concentration (>40 a/o) is required to hydride β-titanium in Ti-H binary compounds.[6] It is unclear whether such levels can be obtained in β-titanium alloys following film rupture in a marine environment. Thus, it is unknown whether a hydrogen mechanism is involved in the EAC behavior of these alloys because of a sequence of events involving (*i*) crack tip passive film destabilization, (*ii*) dissolution, (*iii*) hydrogen production, and (*iv*) hydrogen absorption, or whether EAC is controlled by an entirely different mechanism such as slip-film rupture-dissolution, pre-existing active path dissolution, or film-induced cleavage.[7]

EAC has been observed in PA β-21S in monotonic loading experiments on precracked specimens exposed to 0.6*M* NaCl at −0.6 and −0.15 V *vs.* SCE.[8] Cracking was maximized at intermediate strain rates, suggesting that a balance exists between a combination of film rupture frequency and repassivation rate, and the need for sufficient time to accommodate a time-dependent transport process. Intergranular cracking was observed only when preferential α-precipitation on β-grain boundaries occurred.[8] Coincidentally, coplanar slip was favored in the β-Ti which was prone to preferential grain boundary α-precipitation as opposed to wavy slip.[9] Therefore, it is useful to ascertain whether a preferential dissolution path may have developed. However, little is known about the passivity and repassivation kinetics of β-titanium alloys stabilized with molybdenum and niobium in marine environments over this range of potentials. Tomashov *et al.* reported for Ti-15 Mo in 40% H_2SO_4 at 90°C that dissolution is lowest for 100% β-alloys and increases for β + α and β + ω alloys.[10] Additionally, passive dissolution of hcp α was higher when alloyed with small additions of Al, V, Mo, Zr, or Nb.[10] All these elements increased the passive dissolution rate of α-Ti in H_2SO_4 at 80°C polarized to +1 V. Tomashov *et al.* attributed this effect to a change in ionic conductivity of the predominantly TiO_2 oxide and did not attribute this behavior to any change in the chemical stability of the protective oxide.[10] Initial corrosion research on β-21S alloy has extended only to weight loss measurements.[11] In that study β-21S had a lower dissolution rate and hydrogen uptake efficiency compared to commercially pure Ti and Ti-15Mo. Previous research on molybdenum-containing titanium alloys generally has focused on materials including Zr.[12-15] Others have studied Nb additions[16] and found that there was little effect on the high temperature oxidation resistance of titanium. Therefore, as an initial step in elucidating the role of electrochemical processes on the EAC mechanism of a Mo and Nb stabilized alloy, characterization of the dissolution and passivity of β-21S has been undertaken in room temperature chloride solutions. A subsequent study addresses repassivation kinetics.[17]

To obtain the required strength levels, these alloys are precipitation hardened through growth of an α-precipitate with a needlelike morphology.[8] Hence, a goal of this study is to examine the effect of both composition and microstructure on the electrochemical behavior of these alloys. Both SHT and PA materials were investigated.

Experimental Procedure

The composition of β-21S is reported in Table I. β-21S was SHT for 8 h at 871°C (1600°F) followed by an air cool. Peak-aging comprised a subsequent single-step heat-treatment at 538°C (1000°F) for 8 h followed by an air cool. The presence of an α/β-microstructure, and the absence of other phases, was confirmed by both x-ray diffraction experiments and optical microscopy.[18] α-platelets preferentially nucleate and grow along β-grain boundaries with a Burger's orientation of $(110)_\beta \parallel (0001)_\alpha$, $[111]_\beta \parallel [11\bar{2}0]_\alpha$.[19] This orientation relationship is observed throughout the matrix.[19] Mo and Nb are β-phase stabilizers, while Al is an α-stabilizer.[20] α-Precipitates are Al rich and Mo poor, whereas the β-matrix is the opposite.[21] Therefore, grade 6

Table I. Vendor reported average chemical composition of β-21S.

	Ti	Mo	Al	Nb	Si	O	Fe	N
Weight percent	rem.	14.9	3.15	2.64	0.22	0.198	0.15	0.014
Atomic percent	rem.	7.89	5.99	1.44	0.40	0.629	0.14	0.051

* Electrochemical Society Student Member.
** Electrochemical Society Active Member.

Table II. Vendor reported chemical compositions of grades 2 and 6 Ti in weight percent.

	Ti	Al	Sn	Fe	O	N	H
Grade 2 Ti	rem.	—	—	0.16	0.13	0.005	0.0036
Grade 6 Ti	rem.	5.20	2.30	0.46	0.13	0.010	82 ppm

Ti (Ti-5 Al-2.5 Sn) was utilized to simulate the approximate composition of the α-precipitates found in the β-titanium alloys. The compositions of grades 2 and 6 Ti are listed in Table II. Commercially pure grade 2 Ti (α-phase) also was examined for a baseline comparison.

Samples were polished to a 600 grit finish followed by degreasing in acetone. The testing apparatus comprised 1 cm^2 working electrode area exposed in a flat cell containing a platinized niobium mesh counterelectrode. A saturated calomel reference electrode (SCE) was situated in a well possessing a Luggin capillary.

Rotating disk electrode (RDE) experiments comprised identical counter and reference electrodes as above. The working electrode (0.635 cm diam) surface preparation was the same as stated above. The disk was imbedded in a Kel-F mandrel attached to an analytical rotator and ASR speed controller from Pine Instrument Co. A standard RDE cell was utilized for these experiments.

Polarization measurements were performed with either a Princeton Applied Research (PAR) 173 or PAR 273 potentiostat at a scan rate of 0.05 mV/s. All polarization experiments were performed following exposure to solution for 2 h at open circuit.

Each electrochemical impedance spectroscopy (EIS) experiment comprised ten individual impedance scans. An initial scan was conducted at the open-circuit potential followed by nine scans at 300 mV intervals from −0.3 to 2.1 V *vs.* SCE. Each scan was preceded by a 2 h potentiostatic hold at the given potential, except the open-circuit potential scan which was preceded by 2 h at open circuit. EIS measurements were performed with a Solartron 1286 electrochemical interface and a Model 1255 frequency response analyzer. A 10 mV rms ac voltage signal was applied at frequencies between 10 kHz and 5 mHz using potentiostatic control. Impedance data fitting was performed with CNLS circuit fitting software.[22]

Electrochemical tests were performed on the materials utilizing six different room temperature solutions. These were 0.6*M* NaCl, 0.6*M* NaCl adjusted to pH 1 with HCl, and 5*M* HCl, each in both the aerated and deaerated condition. NaCl solutions (0.6*M*) comprised reagent grade NaCl added to distilled deionized water. Solutions were adjusted to pH 1 with reagent grade HCl. HCl solutions (5*M*) comprised reagent grade HCl and distilled deionized water. The pH of these solutions is −1.64 when the effect of Cl^- on the activity of H^+ is incorporated into the calculation.[23] Deaeration was performed with commercially pure Ar gas. 0.6*M* NaCl solution was utilized to model alloy behavior when exposed to the bulk solution in a marine environment. The pH 1, 0.6*M* NaCl was utilized to discern the behavior of the alloys in a simulated crack tip environment. Although a crack tip solution and its pH has yet to be isolated, a pH 1, 0.6*M* NaCl is considered to be a rough estimate of that solution. Beck[24] has reported that a pH < 1.3 was found next to a corroding pit exposed to neutral chloride solution.[25] Others have reported a pH of 1.7 at a crack tip in Ti-8 Al-1 Mo-1 V.[26] HCl (5*M*) was utilized to analyze material behavior under extremely acidic conditions that are perhaps more severe than a crack tip environment.

Sample surfaces were prepared for Auger electron spectroscopy (AES) in the manner stated above. EIS was then performed on each sample in pH 1, 0.6*M* NaCl as described above, with the final potential at 1.5 V *vs.* SCE. Samples were removed from the cell and rinsed in distilled deionized water. AES was performed on a Perkin Elmer PHI 600 system utilizing a 5 keV beam operated at 0.54 μA. Sputter depth profiling was performed with a 3 keV Ar^+ ion beam. The particular Auger electron transition energies utilized for analysis for each element were selected at Auger energies as close as possible to each other for different elements to obtain comparable escape depths. The transition energies used were Ti_{LMM}-418 eV, O_{KLL}-503 eV, Mo_{MNN}-186 eV, and Al_{KLL}-1396 eV.

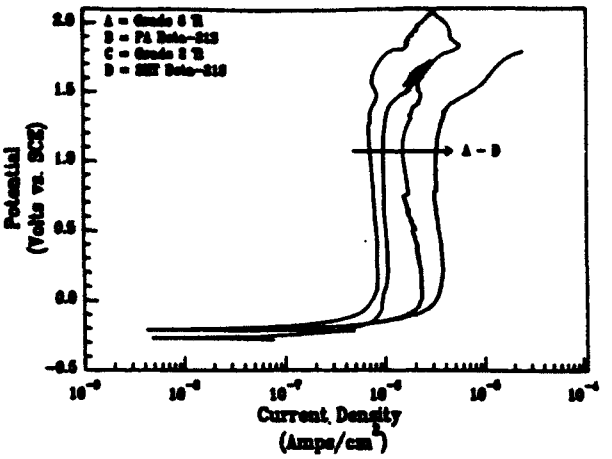

Fig. 1. Representative anodic polarization scans for the four titanium alloys examined in one particular solution (aerated pH 1, 0.6*M* NaCl).

X-ray photoelectron spectroscopy (XPS) was performed on a Kratos XSAM800 utilizing a Mg x-ray source operated at 13 kV and 20 mA, perpendicular to the sample surface. Samples were potentiostatically held at −0.6 V *vs.* SCE in pH 1 0.6*M* NaCl and the surfaces mechanically abraded with SiC paper, thereby allowing the oxides to reform at −0.6V. Samples were rinsed in distilled water upon removal from the cell. The following peaks were used for analysis: Ti-$2p_{3/2}$, O-1s, Mo-$3d_{5/2}$ and $3d_{3/2}$, Nb-$3d_{5/2}$ and $3d_{3/2}$, and Al-2p. Reference to C 1s was used in order to account for specimen charging.

Results and Discussion

Electrochemistry and passivity in pH 1, 0.6M NaCl solutions.—Electrochemistry.—Representative anodic polarization data are reported in Fig. 1 and 2. Figure 1 shows the anodic polarization behavior of the four different materials (SHT and PA β-21S, grade 2, and grade 6) in a particular solution (aerated pH 1, 0.6*M* NaCl). Figure 2 reveals the behavior of one particular material (SHT β-21S) in the six solutions (0.6*M* NaCl, pH 1, 0.6*M* NaCl, and 5*M* HCl, each in the aerated and deaerated conditions). It may be seen in Fig. 1 that a significant increase in anodic current density is observed for each material at approximately 1.4 V. This increase in anodic current density corresponds to the onset

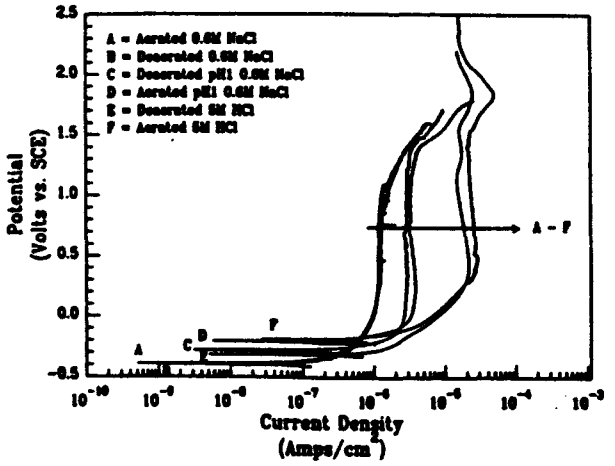

Fig. 2. Representative anodic polarization scans for SHT β-21S in the six chloride-containing solutions.

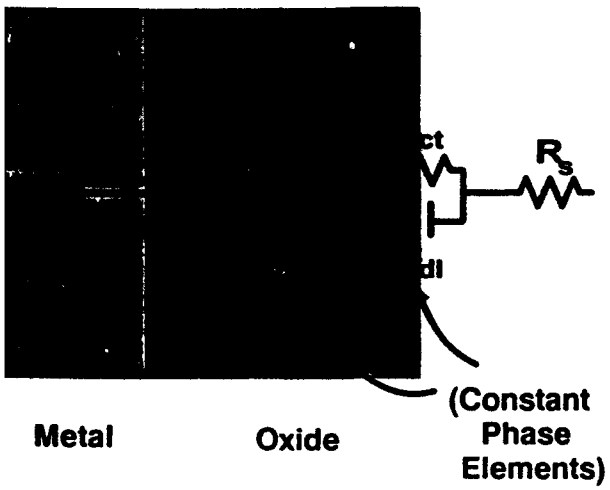

Fig. 3. Proposed circuit model for a passive titanium surface exposed to an aqueous solution.

f oxygen evolution and is not due to pitting. This result as been confirmed by optical microscopy which did not how evidence of pitting. This has also been confirmed by thers, who have stated that pitting is not observed on titaium in room temperature chloride solutions until +9 V is eached.[24] Additionally, Fig. 1 reveals that SHT β-21S has he highest passive current density of all of the materials. 'his was true in all the NaCl solutions examined. In conrast, the magnitudes of the passive current densities of the ther materials varied between solutions and were proba-ly within experimental error.

Figure 1 additionally reveals that the open-circuit potenials for all of the materials are within experimental varibility for one material. Grade 6 Ti, which approximates he composition of the α-precipitates in the PA β-21S, has similar open-circuit potential to that of the SHT materils. This similarity indicates that galvanic cells are unlikely etween the β-titanium matrix and the α-precipitates in he PA materials in this solution. Further, no distinct inreases in anodic current density are observed at applied otential corresponding to the thermodynamic oxidation otentials of the alloying additions.

Figure 2 displays the polarization curves for SHT β-21S n the six solutions. As the pH decreases, the passive curent density increases. Additionally, all of the materials are assive with no pitting observed at potentials as high as .7 V *vs.* SCE. Moreover, no significant differences are oberved between the aerated and deaerated conditions, xcept for a slightly higher passive current density oberved in deaerated 5*M* HCl. The lack of effect of deaeraion has been observed previously by others in abrasion xperiments.[27]

From Figure 2, we see that the oxygen evolution reaction ate becomes small relative to the passive current density at .0 V in 5*M* HCl. This may be due to increased difficulty for lectron-tunneling through the semiconducting passive ilm which thickens with increasing potential. This phe-omenon was observed in all solutions and on all materials, lbeit at different potentials.

In situ characterization of passivity.—EIS was used for n *situ* characterization of the passive layer. A proposed ircuit model for the electrochemical interface may be seen n Fig. 3. This model includes C_{ox} which represents the pace charge capacitance of a compact nonporous oxide. 'he model also comprises a double-layer capacitance (C_{dl}) t the oxide/solution interface. Constant-phase elements re used to better represent the nonidealities of such capacances. EIS data is interpreted in the context of this model.

The impedance response of SHT β-21S exposed to aerted pH 1, 0.6*M* NaCl is seen in Fig. 4a and b. As the potenial is increased, the low frequency impedance decreases. 'urther, as the potential is made more positive with respect to the open circuit, the emergence of two time constants is seen. This occurs until 1.8 V is reached, wherein the two time constants merge again. At these potentials, deconvolution of the data becomes increasingly difficult. However, good correlation was obtained between the model and the experimental data, as seen in Fig. 5.

It was hypothesized here that the high frequency time constant was attributable to the oxide and that the low frequency time constant was attributable to the parallel R_{ct}/C_{dl} combination. To confirm this hypothesis, comparison was undertaken between impedance derived oxide thickness and ellipsometric titanium oxide thickness at various potentials in 0.1*M* HCl.[28] Impedance spectra for grade 2 Ti were obtained at 0, 2, 4, 6, and 8 V *vs.* NHE (normal hydrogen electrode), with the specimen prepared in identical fashion to those of the ellipsometric study.[28] Utilizing a dielectric constant of 100 for TiO_2 in conjunction with the obtained value for C_{ox}, a good correspondence was obtained for the oxide thickness (Fig. 6). This result confirms the hypothesis that the high frequency time constant was indeed attributable to the oxide.

The charge transfer resistance, R_{ct}, is approximately one order of magnitude larger than the oxide resistance, R_{ox}, at the lower potentials. Therefore, we conclude that the charge-transfer reaction is the rate-determining step and dominates the passive dissolution of the alloys. Also, R_{ct} for grade 2 Ti in aerated pH 1, 0.6*M* NaCl increases with potential until approximately 1.2 V whereupon the charge-transfer resistance begins to decrease. The decrease in the charge-transfer resistance coincides with the onset of oxygen evolution, as discussed earlier.

Oxide thickness and apparent resistivity were calculated from the parameters obtained by circuit fitting. The oxide thickness may be calculated by utilizing the equation

$$d_{ox} = \frac{\epsilon \epsilon_o A}{C_{ox}} \quad [1]$$

where d_{ox} is the oxide thickness, C_{ox} is the oxide capacitance, ϵ is the dielectric constant of the oxide, ϵ_o is the permittivity of free space, and A is the surface area. The apparent oxide resistivity may be calculated as follows, assuming that it varies linearly with thickness. From Eq. 1

$$\frac{A}{d_{ox}} = \frac{C_{ox}}{\epsilon \epsilon_o} \quad [2]$$

Assuming that

$$\rho_{ox} = R_{ox}\left(\frac{A}{d_{ox}}\right) \quad [3]$$

and, substituting Eq. 2 into Eq. 3, the following equation is obtained

$$\rho_{ox} = \frac{R_{ox} C_{ox}}{\epsilon \epsilon_o} \quad [4]$$

Equation 4 provides an indication of apparent oxide resistivity that is independent of geometric thickness.

Figures 7 and 8 show plots of the oxide thicknesses and apparent resistivities, respectively, *vs.* potential for the materials in aerated pH 1 solution, utilizing a dielectric constant of 100 for all materials. The oxide thicknesses increase linearly with increasing potential and the growth rate of the β-21S alloys is less than that of either grade 2 or grade 6 Ti. The oxide growth rate for grade 2 Ti (approximately 23 Å/V) corresponds with earlier observations for commercially pure titanium in 0.1*M* HCl.[28] Additionally, the apparent oxide resistivity decreases with potential, implying that the oxide is becoming increasingly defective. Handbook values for bulk TiO_2 resistivity are in the range of 10^{13}-10^{18} Ω cm,[29] while calculated values from the experiments here yield values in the 10^7 to 10^{10} range, depending on potential. This discrepancy may be because a 10-50 Å oxide grown in solution is more electronically and/or ionically defective than a bulk three-dimensional oxide, the oxide incorporates alloying additions, oxide hydration, or chloride ion incorporation. Tomashov *et al.* have expressed a similar viewpoint in their review of the passivity of a broad range of Ti base alloys.[10] The relative rankings of the

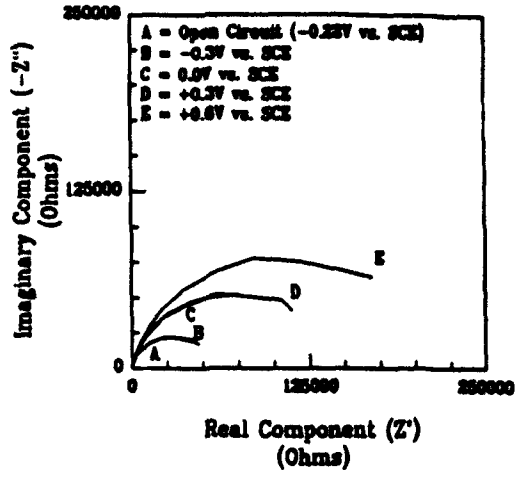

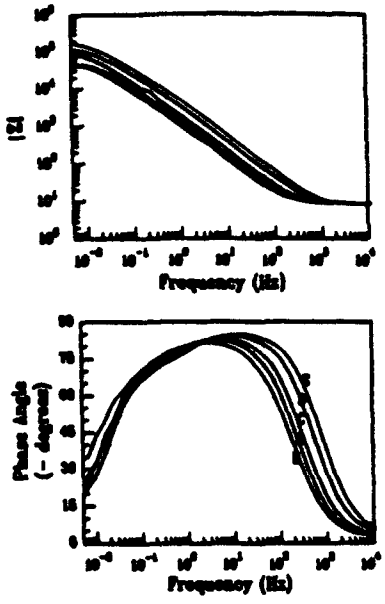

Fig. 4 (a) Electrochemical impedance response of SHTβ-21S exposed to aerated pH 1, 0.6*M* NaCl at potentials ranging from open circuit to 0.6 V vs. SCE.

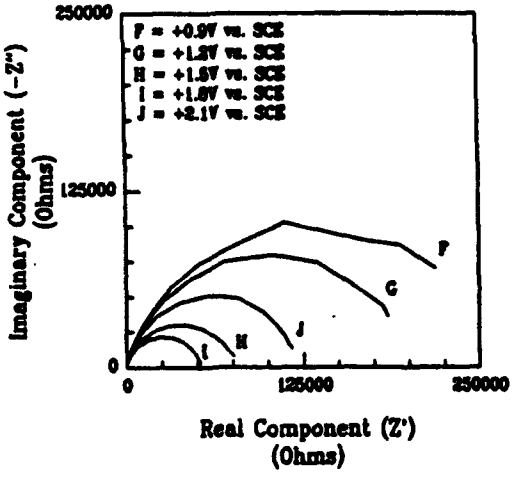

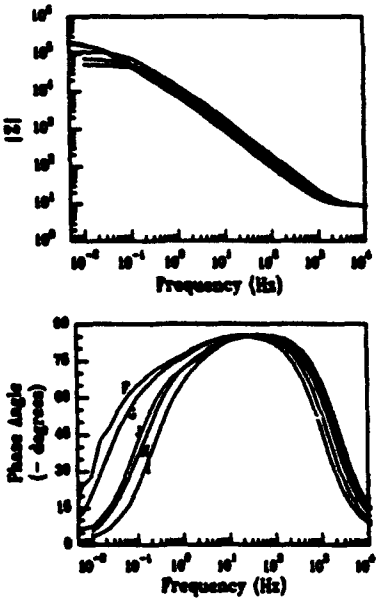

Fig. 4 (b) Electrochemical impedance response of SHTβ-21S exposed to aerated pH 1, 0.6*M* NaCl at potentials ranging from 0.9 to 2.1 V vs. SCE.

oxide thickness and apparent resistivity, from the material with the highest property to that with the lowest, varied nonsystematically from solution to solution.

Ex situ characterization of passivity.—AES was conducted on SHT β-21S previously exposed to aerated pH 1, 0.6*M* NaCl at 1.5 V *vs.* SCE. A sputter depth profile is shown in Fig. 9. The pH 1, 0.6*M* NaCl solution was chosen for *ex situ* characterization experiments because its aggressiveness is between that of 5*M* HCl and 0.6*M* NaCl. EIS experiments were performed every 300 mV from open circuit up to 1.5 V *vs.* SCE, so that the oxide examined by AES after sample removal from the electrochemical cell experienced the same history as in the dc and ac experiments discussed earlier. Due to the small amount of Nb (atomic number 41) in the bulk alloy and significant peak overlap with Mo (atomic number 42), the Nb concentration cannot be accurately determined and is not shown. Na or Cl peaks were not detected. Figure 9 shows that the passive film is rich in O and Ti at an approximate composition of TiO_2. The concentration of Al throughout the passive film appears constant at the concentration observed within the bulk alloy. The increase in Mo concentration as the base metal is approached has been seen elsewhere in β-titanium alloys.[14] This increase has been attributed to a lower mobility of Mo ions through the passive film relative to Ti cations.[14] The low concentration of alloying additions within the passive film may explain the similar passive electrochemical behavior observed between β-21S and grades 2 and 6 Ti.

To determine an oxide thickness, a grade 2 Ti standard was used. EIS experiments were performed in the manner discussed above, with the thickness determined after a final potential of 1.5 V *vs.* SCE was reached. The oxide thickness was computed utilizing a dielectric constant of 100. The oxide was sputter depth profiled to determine the beam sputter rate. This rate was utilized to determine the thickness of the β-21S sample, assuming a uniform sputter rate. The oxide thickness was chosen to be the thickness at which the concentration of oxygen is one-half its maximum. The oxide thickness for SHT β-21S was 24 Å at 1.5 V *vs.* SCE. This value is in agreement with the value determined by EIS (Fig. 7).

From AES, we see that there is little incorporation of alloying additions into the outer layers of the passive film. The minimization of alloying additions in the passive film may account for the similar passive electrochemical behaviors of SHT and PA β-21S, grade 2 and grade 6 titanium as observed here by both the dc and ac methods.

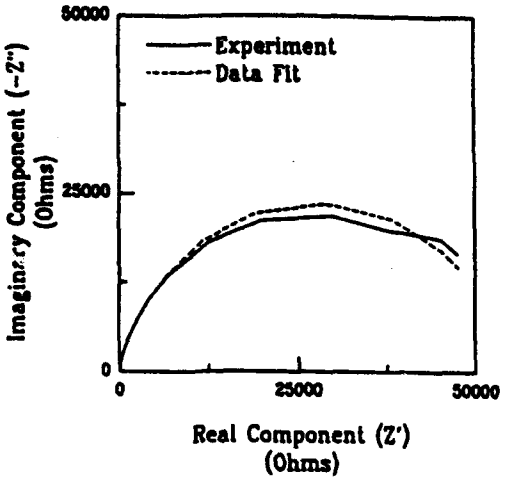

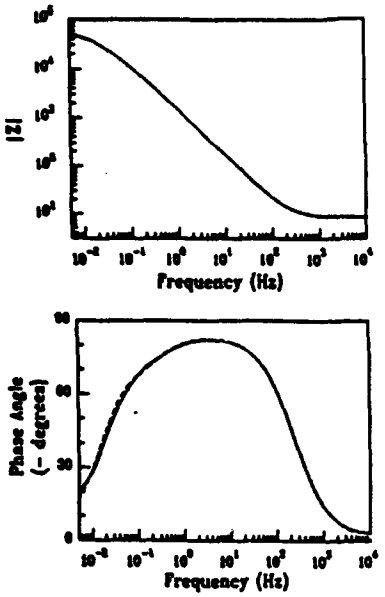

Fig. 5. Comparison of experimental data (SHT β-21S, aerated pH 1, 0.6*M* NaCl, open circuit) to that obtained by data fitting with CNLS fitting software[22] using the circuit model shown in Fig. 3.

To examine an oxide formed in solution, XPS experiments were performed on oxide films of SHT β-21S, PA β-21S, and grade 2 Ti formed at −0.6 V *vs.* SCE following mechanical abrasion with SiC paper in aerated pH 1, 0.6*M* NaCl. XPS revealed that the compositions of the oxides on both PA and SHT β-21S were similar. All oxides were predominantly TiO_2, with small amounts of MoO_2, MoO_3, Nb_2O_5, and Al_2O_3 also detected within the oxides on β-21S (Table III). The particular oxidation states seen here are in agreement with observations on other β-titanium alloys.[12] The smaller peaks associated with all alloying additions occurred at binding energies which were consistent with their being oxidized. Table III contains the energies of the obtained photoelectron peaks, the corresponding handbook values for the compounds attributed to these peaks,[20] and the formation potentials for such oxides over a range of potentials,[21,22] since the surface pH upon mechanical destabilization of the oxide film is not known. For Mo, the observation of MoO_3 is consistent with the participation of hydrated MoO_3 (H_2MoO_4).[21] Because most hexavalent Mo compounds have nearly identical binding energies,[23] the binding energy of H_2MoO_4 is assumed to be equal to that of MoO_3. The similar oxide compositions may explain the similar electrochemical behaviors of the PA and SHT materials. Moreover, there is no evidence suggesting that the oxidation mechanism of β-21S is different from that of grade 2 Ti in pH 1, 0.6*M* NaCl.

Electrochemistry and passivity in 0.6M NaCl solutions.—*Electrochemistry and in situ characterization of passivity.*—The behavior of the titanium alloys in neutral 0.6*M* NaCl (Fig. 10) was similar to that observed in pH 1 adjusted solutions. The passive current densities for all the materials were lower in the neutral solution than in pH 1. These current densities were confirmed by impedance measurements wherein the charge-transfer resistances which dominate the polarization resistance and, hence, the passive current densities were higher. Additionally, the oxide resistances appeared to be higher for the neutral solutions due to both increased apparent oxide resistivity and increased oxide thickness.

As in the pH 1 solutions, there appeared to be no discernible difference between aerated and deaerated conditions. Additionally, as in previous experiments, SHT β-21S displayed the highest passive current density of all the materials examined. The open-circuit potentials, including grade 6 Ti, were within experimental variability, again indicating that no significant galvanic couples are present in the PA material.

Cathodic polarization scans (Fig. 11) performed in deaerated 0.6*M* NaCl indicated similar exchange current densities for the hydrogen evolution reaction (HER) on the β-titanium materials, ranging from 2.0×10^{-11} to 4.6×10^{-11} A/cm^2. Although these are higher than that found for grade 2 Ti (1×10^{-12} A/cm^2), the exchange current densities are far below those found for the HER on pure Mo and Nb,[24] which are the major alloying additions. This result again suggests that there is a low concentration of alloying addi-

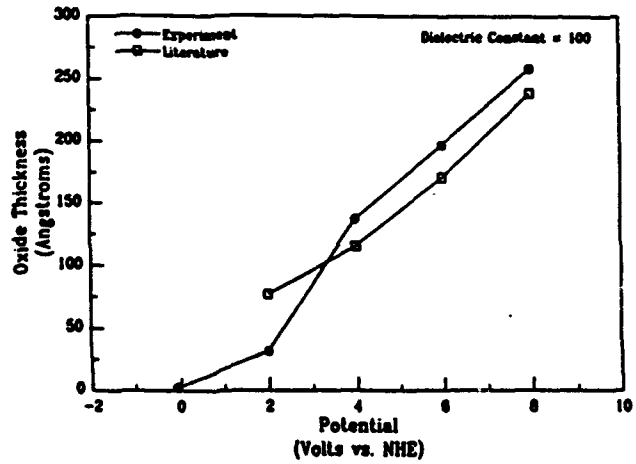

Fig. 6. Comparison of oxide thickneses on grade 2 Ti as a function of applied potential to that found in the literature.[25]

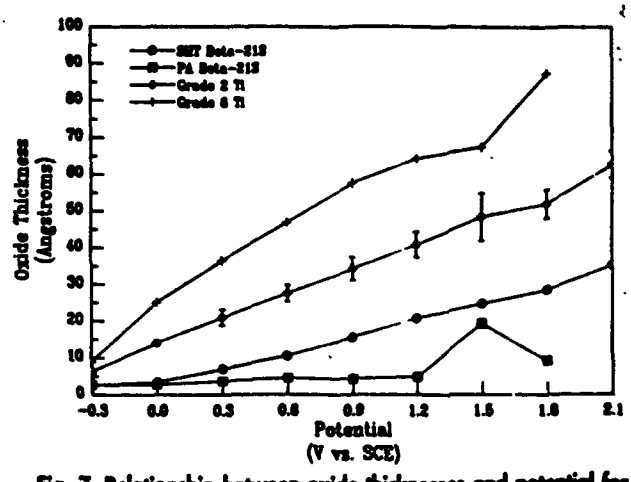

Fig. 7. Relationship between oxide thicknesses and potential for SHT and PA β-21S, grade 2 Ti and grade 6 Ti exposed to aerated pH 1, 0.6*M* NaCl. A dielectric constant of 100 was assumed.

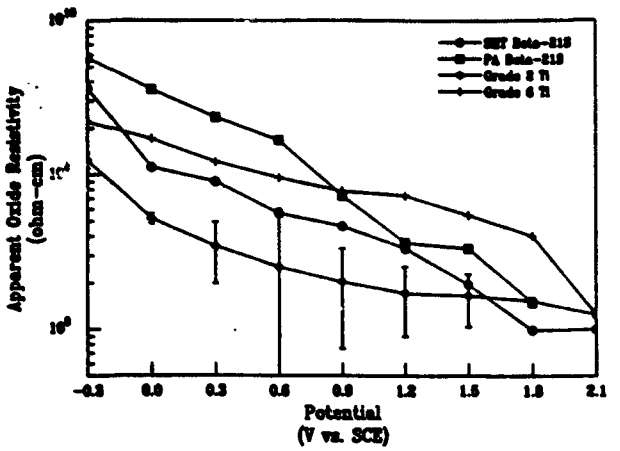

Fig. 8. Relationship between apparent oxide resistivities and potential for SHT and PA β-21S, grade 2 Ti and grade 6 Ti exposed to aerated pH1, 0.6M NaCl. A dielectric constant of 100 was assumed.

Table III. Binding energies obtained from XPS experiments after abrasion (pH 1, 0.6M NaCl, −0.6 V vs. SCE), handbook values for the binding energies of the metal oxides,[30] and the corresponding formation potential of the oxides at two different pH.[31,32]

	Ti $2p_{3/2}$ TiO_2	Mo $3d_{5/2}$ MoO_2	Mo $3d_{5/2}$ MoO_3	Nb $3d_{5/2}$ Nb_2O_5	Al 2p Al_2O_3
Grade 2 Ti	458.5	n/a	n/a	n/a	n/a
SHT β-21S	458.9	229.7	232.0	207.2	74.4
PA β-21S	458.3	229.6	232.2	207.2	74.3
Handbook[30]	458.5	229.2	232.7	207.3	74.7
Minimum formation potential (V vs. SCE) pH 1	−0.889	−0.15[a]	−1.391	−0.589	−2.022[b]
pH = 8	−1.303	−0.786	−1.805	−1.003	−2.264

[a] $-Mo^{3+} + 2H_2O \rightarrow MoO_2 + 4H^+ + 4e^-$ reaction, assuming $[Mo^{3+}] = 10^{-6}$ M; from Yang *et al.*[32]
[b] $-Al \rightarrow Al^{3+} + 3e^-$ reaction, assuming $[Al^{3+}] = 10^{-6}$ M.

tions incorporated into the outer layers of the passive films of SHT and PA β-21S and that the TiO_2-dominated oxide may account for the similar passive electrochemical behavior observed for all the materials examined in neutral 0.6*M* NaCl.

Electrochemistry and passivity in 5M HCl solutions.—Electrochemistry.—All the materials examined were passive in aerated 5*M* HCl except for grade 2 Ti which displayed an active/passive transition (Fig. 12). Others have observed that for commercially pure Ti, an active/passive transition is present in 5*M* HCl[26] but not in 0.1*M* HCl[28] (approximately pH 1). The more active open-circuit potential of grade 2 Ti enables the observation of the active/passive transition. To verify the existence of such a transition on the other materials, similar experiments were performed in deaerated 5*M* HCl (Fig. 13). An active/passive transition occurs on all the alloys in deaerated 5*M* HCl, except for SHT β-21S, which had a significantly higher open-circuit potential. A similar result was observed by Laser and Marcus[14] for beta III (Ti, 11.5% Mo, 4.5% Sn, 6% Zr) which exhibited spontaneous passivity when pure Ti showed an active/passive transition in a pH 2.3 electrolyte. Previous research has observed an active/passive transition on other β-titanium alloys (Ti-13V-11Cr-3 Al) in 20% HCl (6.5*M*), albeit at 35°C.[26] A transition was observed in 5% HCl (1.6*M*) at 65°C.[26] In general, increasing temperatures tend to promote the development of an active/passive transition at fixed HCl concentration.[26] The open-circuit potential of SHT β-21S is more noble than that of both PA β-21S and grade 6 Ti, indicating that the α-phase lowers the open-circuit potential of PA β-21S. An active/passive transition is observed in addition to an increased passive current density. Moreover, a galvanic couple between the α and β-phases may be present under these conditions.

The Mo/Nb alloying addition promotes spontaneous passivity on SHT β-21S in deaerated 5*M* HCl. However, it was unclear if the lack of an active/passive transition is due to an actual effect upon the anodic oxidation process or whether increased cathodic kinetics (exchange current density, or lower Tafel slope) raised the open-circuit potential above such a transition. Therefore, cathodic scans on SHT β-21S in deaerated 5*M* HCl were performed. Although the exchange current density for the HER on SHT β-21S is higher than that on the α-alloys (Table IV), it is not high enough to account for a 300 mV increase in the open-circuit potential. PA β-21S supports a higher exchange current density for hydrogen evolution than SHT β-21S, even though its open-circuit potential is lower. Therefore, we conclude that the presence of Mo and Nb affects the anodic process, rendering titanium spontaneously passive in deaerated 5*M* HCl. The exact process by which the material is rendered passive is unknown. One hypothesis is that incorporation of Mo^{+3} into a normally nonprotective Ti_2O_3 film renders it more protective. Another hypothesis is that Mo in the solid state lowers the oxidation rate of the metal substrate beneath the nonprotective film. A nonprotective Ti_2O_3 film exists in the potential region associated with the active/passive transition on Ti.[27] It is possible that elemental Mo occupies kink sites to impede metal dissolution. Additionally, others have put forth models explaining beneficial effects of Mo on passive films that may be applicable

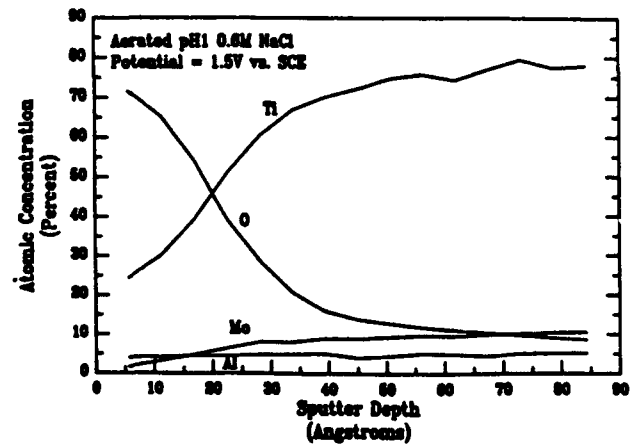

Fig. 9. AES sputter depth profile of SHT β-21S exposed to aerated pH 1, 0.6M NaCl.

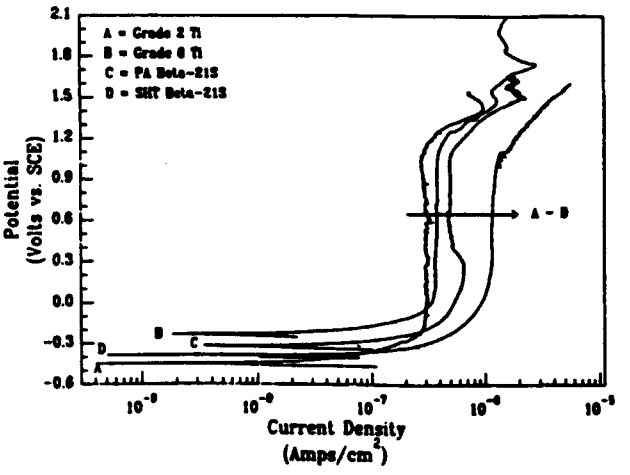

Fig. 10. Anodic polarization scans for SHT β-21S, PA β-21S, grade 2 Ti, and grade 6 Ti aerated 0.6M NaCl.

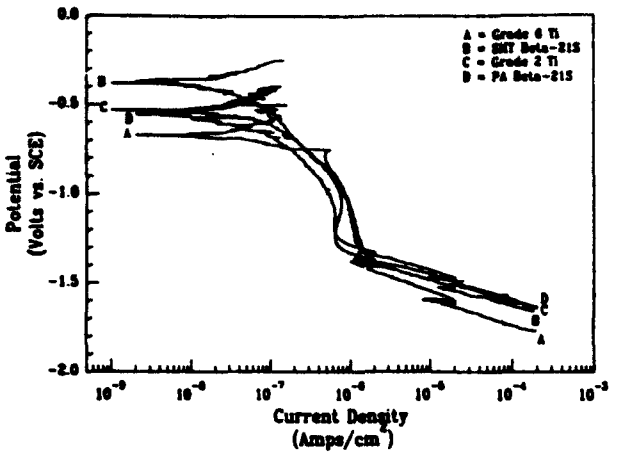

Fig. 11. Cathodic polarization scans for SHT β-21S, PA β-21S, grade 2 Ti, and grade 6 Ti exposed to 0.6M NaCl.

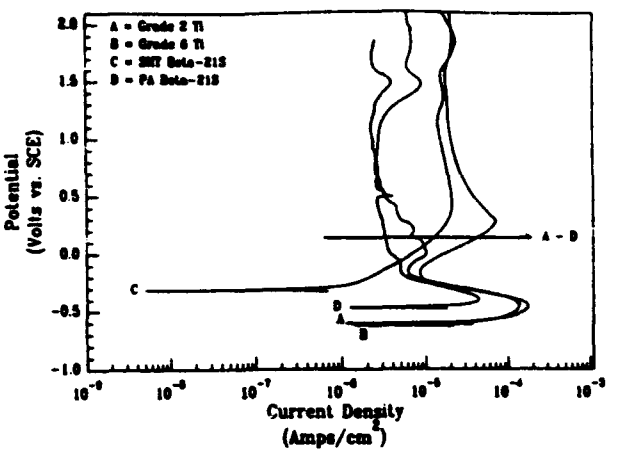

Fig. 13. Anodic polarization scans for SHT β-21S, PA β-21S, grade 2 Ti, and grade 6 Ti in deaerated 5M HCl.

here,[36] however these theories require the presence of Mo^{+6} which is not thermodynamically stable over a portion of the potential range we have examined.

A pitting potential was not observed for any alloy in 5M HCl up to 2.0 V *vs.* SCE. Furthermore, the passive current densities for all the materials were highest in 5M HCl. As in NaCl solutions, SHT β-21S displayed the highest passive current density of all of the materials in aerated 5M HCl, but PA β-21S displayed a higher passive current density in deaerated 5M HCl.

The peak current density for PA β-21S in 5M HCl (4.5×10^{-5} A/cm²), the most aggressive solution examined, is two orders of magnitude too low to account solely for the slowest crack growth rates observed (10^{-6} mm/s, 2.54×10^{-4} mm/min displacement rate).[8] Therefore, we conclude that highly localized mechanical destabilization of the passive film is required for EAC of these alloys even after crack tip cation hydrolysis and acidification, regardless of the exact mechanism of EAC.

In situ characterization of passivity.—Impedance spectra for grade 2 Ti exposed to aerated 5M HCl in the active range display distinct two time constant behavior although the polarization curve indicates that the material is active upon anodic polarization over a wide potential range. However, active behavior does not imply that no oxide is present. Other researchers have stated that even in the active region, dissolution is strongly inhibited by an oxide which apparently can exist metastably even in strong acid solution.[38] It was hypothesized that steady-state dissolution may proceed through oxide formation and dissolution steps.[39] Others have noted that in the active region, a porous film of Ti_2O_3 is present.[37]

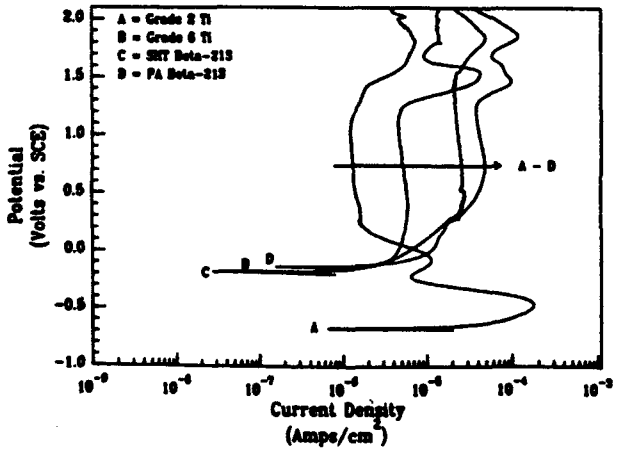

Fig. 12. Anodic polarization scans for SHT β-21S, PA β-21S, grade 2 Ti, and grade 6 Ti in aerated 5M HCl.

Good correlation between the proposed impedance circuit model and data was observed for all the materials in all the examined solutions except 5M HCl. Figure 14 displays the impedance response of PA β-21S in aerated 5M HCl at five different potentials. Additional time constants (*i.e.*, low frequency inductive looping) are present in the spectra that are not seen in any spectra from other solutions. The origin of this looping is unclear but it may indicate a change in the properties of the electrochemical interface.

Impedance spectra similar to that seen for β-21S exposed to aerated 5M HCl have been observed by others. Impedance behavior of Al exposed to 0.5M NaCl below its pitting potential displayed low frequency looping.[40] This looping was attributed to a diffusion-controlled process within the oxide. Others have suggested that a buildup of *surface charge* at the metal-oxide interface may yield similar behavior.[41]

Although the polarization curves in aerated 5M HCl displayed a potential independent region indicative of passivity, it was of interest to confirm this, as the impedance spectra did not yield good agreement with the proposed circuit model for passivated titanium. Therefore, rotating disk electrode experiments were undertaken to distinguish possible anodic mass-transport control from passivity. If the system was passive, the behavior of the system within the passive region should be fluid velocity and, hence, rotation rate independent. However, if the system was anodically mass-transport limited, a change in anodic current density would be observed as a function of rotation rate. Anodic polarization experiments conducted with PA β-21S at 0, 250, 1000, and 5000 rpm in aerated 5M HCl are illustrated in Fig. 15. There is no discernible effect of rotation on the anodic current density of PA β-21S in its region of potential independent behavior. Therefore, we conclude that β-21S is passive in aerated 5M HCl.

Experiments in 5M HCl proved to be beneficial in elucidating the effect of Mo/Nb additions on the passivity of β-21S. The alloying additions promote formation of a passive film on SHT β-21S in deaerated 5M HCl by not only increasing cathodic kinetics, thereby raising the open-circuit potential, but by affecting the anodic process as well. PA β-21S undergoes an active/passive transition, indicat-

Table IV. Exchange current densities and Tafel slopes for the hydrogen evolution reaction on alloys exposed to deaerated 5M HCl.

	Exchange current density (A/cm²)	Tafel slope (mV/decade)
SHT β-21S	6.7×10^{-10}	84
PA β-21S	3.9×10^{-9}	87
Grade 2 Ti	2.0×10^{-10}	91
Grade 6 Ti	2.9×10^{-10}	84

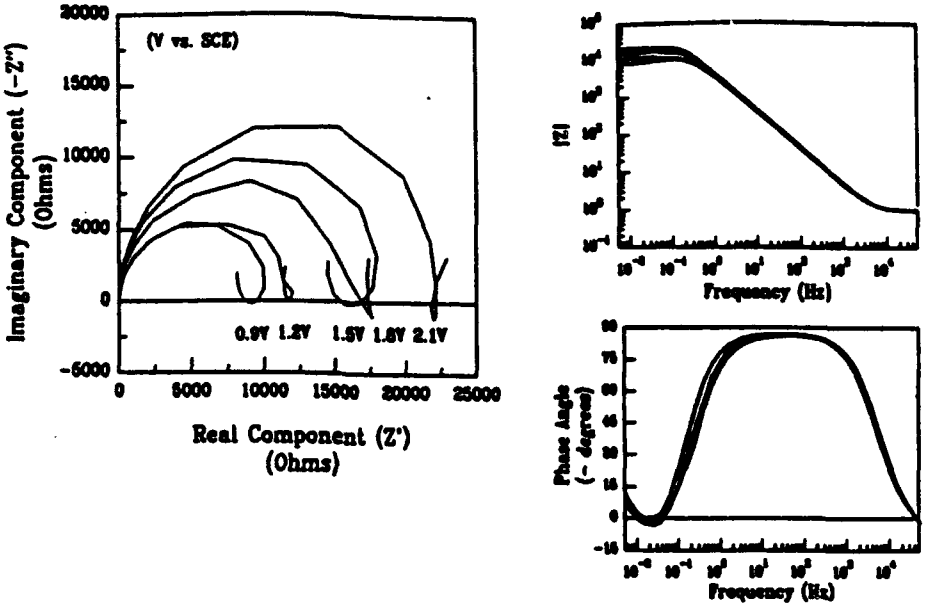

Fig. 14. Electrochemical impedance response of PA β-21S exposed to aerated 5M HCl.

ing that the α-precipitates within the β-matrix are deleterious to the formation of a passive layer. This condition is confirmed since grade 6 Ti, which roughly models the α-precipitates, was active in deaerated 5*M* HCl up to approximately −0.15 V *vs.* SCE.

Conclusion

Analysis of the passive film on Mo and Nb stabilized β-titanium alloy (β-21S) in room temperature solutions simulating crack tip chemistries possible in marine environments has been performed utilizing both dc and ac methods. *There are no major electrochemical differences* between β-21S exposed to 0.6*M* NaCl and pH 1, 0.6*M* NaCl in its PA and SHT forms, although SHT β-21S almost always yielded the largest passive current density. Moreover, significant differences do not exist between either the model precipitate (grade 6 Ti) or commercially pure Ti (grade 2 Ti) and β-21S in the NaCl solutions. This finding suggests that there is minimal galvanic interaction between the matrix and precipitates in PA β-21S in the NaCl environments. All the alloys were spontaneously passive in the NaCl solutions examined and no pitting potentials were observed up to 2.1 V *vs.* SCE. However, experiments in deaerated 5*M* HCl reveal an active/passive transition for all alloys except SHT β-21S, indicating that the α-precipitates in PA β-21S have a deleterious effect upon passivity and that local galvanic coupling between the α- and β-phases may occur. Both the anodic and cathodic kinetics were affected by the Mo/Nb additions in β-21S. Rotating disk electrode experiments confirmed that β-21S is passive in a 5*M* HCl environment. Similarity of hydrogen evolution kinetics, the lack of observed alloying addition oxidation, and AES and XPS studies indicate limited incorporation of alloying additions into the passive film in the NaCl solutions. The passive film on all Ti alloys was predominantly TiO_2 with lesser amounts of oxidized Mo, Nb, and Al contained in the oxides on β-21S. The small quantity of alloying additions within the passive film may account for the similar passive electrochemical behaviors observed among the studied alloys. All the alloys in this study yielded peak current densities that were too low to account solely for crack growth rates observed in separate studies, even after crack tip acidification. The passive film, therefore, must be mechanically destabilized to account for these crack growth rates, regardless of the exact mechanism.

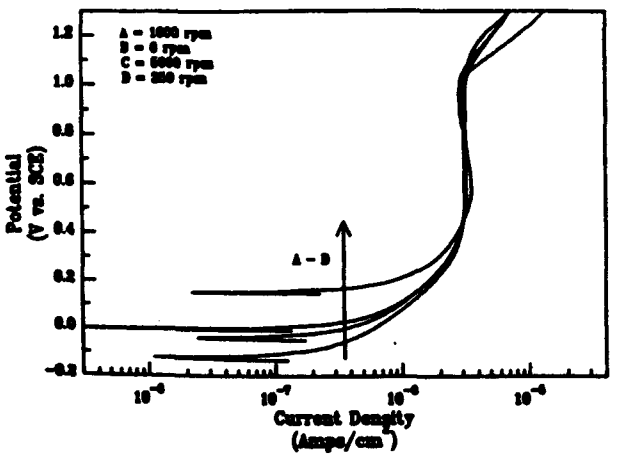

Fig. 15. Anodic polarization response of a PA β-21S rotating disk electrode exposed to aerated 5M HCl.

Acknowledgments

The authors acknowledge the Office of Naval Research (Grant No. N00014-91-J-4164) and the Virginia Center for Innovative Technology for their support of this work. The authors also thank Titanium Metals Corporation for their generous donation of alloys. The authors acknowledge Dr. R. Bayles and the Naval Research Laboratory for help with AES experiments, S. McCartney and Virginia Polytechnic Institute for help with XPS experiments, and L. Young, G. Young, and R. P. Gangloff for helpful discussions.

Manuscript submitted April 2, 1993; revised manuscript received June 18, 1993. This was Paper 144 presented at the Toronto, ON, Canada, Meeting of the Society, Oct. 11-16, 1992.

The University of Virginia assisted in meeting the publication costs of this article.

REFERENCES

1. *Titanium and Its Alloys*, Titanium Development Association, Boulder, CO (1992).
2. D. N. Williams, *J. Inst. Met.*, **91**, 147 (1962-1963).
3. H. G. Nelson, in *First Thermal Structures Conference*, E. Thornton, Editor, p. 301, University of Virginia, Charlottesville, VA (1990).
4. D. N. Fager and W. F. Spurr, *Trans. ASM*, **61**, 283 (1968).
5. H. G. Nelson, D. P. Williams, and J. E. Stein, *Metall. Trans. A*, **33**, 469 (1972).
6. A. D. McQuillan, *Proc. R. Soc. London, Ser. A*, **204**, 309 (1950).
7. T. R. Beck, *Corrosion*, **30**, 408 (1974).
8. L. M. Hartman and R. P. Gangloff, *Proceedings, Seventh World Conference on Titanium*, S. H. Froes, Editor, TMS-AIME, Warrendale, PA in press.

9. G. A. Young, Jr., and J. R. Scully, *Proceedings of the β-titanium Symposium*, TMS Annual Meeting, Denver, CO, D. Eylon, Editor, Feb. 21-25, 1993.
10. N. D. Tomashov, G. P. Chernova, Y. S. Ruscol, and G. A. Ayuyan, *Electrochim. Acta.*, 19, 159 (1974).
11. J. S. Grauman, *Proceedings, Seventh World Conference on Titanium*, S. H. Froes, Editor, TMS-AIME, Warrendale, PA, in press.
12. P. A. Mäusli, S. G. Steinemann, and J. P. Simpson, in *Proceedings of the Sixth World Conference on Titanium*, P. Lacombe, R. Tricot, and G. Béranger, Editors, p. 1759 (1988).
13. R. W. Schutz and J. S. Grauman, in *Industrial Applications of Titanium and Zirconium: Fourth Volume, ASTM STP 917*, C. S. Young and J. C. Durham, Editors, p. 130, American Society for Testing and Materials, Philadelphia (1986).
14. D. Laser and H. L. Marcus, *This Journal*, 127, 763 (1980).
15. J. A. Petit, D. Delaunay, D. Leroy, and G. Chatainier, *Proceedings, Fourth World Conference on Titanium*, H. Kimura and O. Izumi, Editors, p. 1363, TMS-AIME, Warrendale, PA.
16. P. Kofstad, K. Hauffe, and H. Kjolesdal, *Acta Chem. Scand.*, 12, 239 (1958).
17. D. G. Kolman and J. R. Scully, Unpublished research.
18. G. A. Young, Jr., and J. R. Scully, UVA Report No. UVA/525464/MSE93/101, October 1992.
19. G. A. Young, Jr., Master's Thesis, University of Virginia, Charlottesville, VA (1993).
20. *Metals Handbook*, 8th ed., Vol. 8, American Society for Metals, Metals Park, OH (1973).
21. E. W. Collings, *Physical Metallurgy of Ti Alloys*, p. 70, ASM International, Metals Park, OH (1984).
22. J. R. MacDonald, *Complex Nonlinear Least Squares Immitance Fitting Program*, University of North Carolina, Chapel Hill, NC, Version 3.02.
23. P. O. Garland, SINTEF publication STF16-A88085, Trondheim, Norway (1988).
24. T. R. Beck, *Localized Corrosion*, B. F. Brown *et al.*, Editors, p. 644, NACE, Houston, TX (1974).
25. R. W. Powers and J. F. Wilfore, in *Fundamentals of Electrochemical Machining*, C. L. Faust, Editor, p. 135, The Electrochemical Society, Inc., Princeton, NJ (1971).
26. B. F. Brown, C. T. Fujii, and E. P. Dahlberg, *This Journal*, 116, 218 (1969).
27. N. D. Tomashov and L. P. Vershinina, *Electrochim. Acta.*, 15, 501 (1970).
28. T. Ohtsuka, M. Masuda, and N. Sato, *This Journal*, 132, 787 (1985).
29. *Handbook of Chemistry and Physics*, 64th ed., R. C. Weast, Editor, p. E-55, Chemical Rubber Publishing Co., Boca Raton, FL (1983-1984).
30. *Handbook of X-ray Photoelectron Spectroscopy*, C. D. Wagner *et al.*, Editors, Perkin Elmer Corp., Norwalk, CT (1979).
31. *Atlas of Electrochemical Equilibria in Aqueous Solutions*, M. Pourbaix, 2nd ed, NACE, Houston, TX (1974).
32. W. Yang, R. Ni, H. Hua, and A. Pourbaix, *Corros. Sci.*, 24, 691 (1984).
33. W. E. Swartz and D. M. Hercules, *Anal. Chem.*, 43, 1774 (1971).
34. B. E. Conway, *Electrochemical Data*, Elsevier, New York (1952).
35. A. Caprani and J. P. Frayret, *Electrochim. Acta.*, 24, 835 (1979).
36. M. Levy and G. N. Sklover, *This Journal*, 116, 323 (1969).
37. H. Kaesche, *Metallic Corrosion*, p. 265, NACE, Houston, TX (1985).
38. D. D. Macdonald, in *Critical Factors in Localized Corrosion*, G. S. Frankel and R. C. Newman, Editors, PV 92-9, p. 1, The Electrochemical Society Proceedings Series, Pennington, NJ (1992).
39. T. R. Beck, *Electrochim. Acta.*, 18, 815 (1973).
40. J. B. Bessone, D. R. Salinas, C. E. Mayer, M. Ebert, and W. J. Lorenz, *ibid.*, 37, 2283 (1992).
41. H. J. de Wit, C. Wijenberg, and C. Crevecoeur, *This Journal*, 126, 779 (1979).

DISTRIBUTION LIST

1 - 3	Dr. A. John Sedriks Materials Division, Code 1131 Office of Naval Research 800 N. Quincy Street Arlington, VA 22217-5660
4	Mr. Michael Karp Administrative Contracting Officer Office of Naval Research Resident Representative 101 Marietta Tower, Suite 2805 101 Marietta Street Atlanta, GA 30303
5 - 6	F. O'Bryant, Clark Hall
7 - 12	R. P. Gangloff
13	J. R. Scully
14	R. G. Kelly
15	W. A. Jesser
*	SEAS Postaward Administration
16	SEAS Preaward Administration

*Cover Letter

JO#5429:ph

June 1993

BASIC DISTRIBUTION LIST

Technical Reports and Publications

Organization	Copies
Defense Technical Information Center Cameron Station Alexandria, VA 22304-6145	2
Office of Naval Research 800 N. Quincy Street Arlington, VA 22217-5660 ATTN: Code 3310	3
Naval Research Laboratory 4555 Overlook Ave, S.W. Washington, DC 20375 ATTN: Code 6000	1
Code 6300	1
Code 5227	1
Naval Air Warfare Center White Oak Detachment Silver Spring, MD 20903-5000 ATTN: Library	1
Code R33	1
Naval Postgraduate School Monterey, CA 93940 ATTN: Mechanical Engineering Department	1
Naval Air Systems Command Washington, DC 20361 ATTN: Code 5304	1
Naval Sea Systems Command Washington, DC 20362 ATTN: Code 05M	1
Code 05R	1

Organization	Copies
Naval Air Warfare Center Aircraft Division, Trenton Trenton, NJ 08628 ATTN: Library	1
Naval Facilities Engineering Service Center Port Hueneme, CA 94043 ATTN: Materials Div.	1
Naval Surface Warfare Center Carderock Division Bethesda, MD 20084 ATTN: Library	1
Naval Underwater Warfare Ctr. Newport, RI 02840 ATTN: Library	1
Naval Air Warfare Center Weapons Division China Lake, CA 93555-6001 ATTN: Library	1
NASA Lewis Research Center 21000 Brookpark Road Cleveland, OH 44135 ATTN: Library	1
National Institute of Standards and Technology Gaithersburg, MD 20899 ATTN: Metallurgy Division	1
Ceramics Division	1
Fracture & Deformation Division	1

Organization	Copies
Naval Command, Control and Ocean Surveilance Center R&D Division San Diego, CA 92152-5000 ATTN: Library	1
Office of the Assistant Commander HQ Marine Corps 2 Navy Annex Washington, DC 20380-1775 ATTN: Scientific Advisor	1
Army Research Office P.O. Box 12211 Research Triangle Park, NC 27709 ATTN: Metallurgy & Ceramics Program	1
Army Materials Technology Laboratory Watertown, MA 02172-0001 ATTN: SLCMT-TMM	1
Air Force Office of Scientific Research Building 410 Bolling Air Force Base Washington, DC 20332 ATTN: Electronics & Materials Science Directorate	1
NASA Headquarters Washington, DC 20546 ATTN: Code RN	1
Naval Surface Warfare Center Port Hueneme Division 4363 Missile Way Port Hueneme CA 93043-4307 ATTN: Library	1
Metals Information Analysis Center Purdue University 2595 Yeager Road West Lafayette IN 47906	1

Organization	Copies
Naval Facilities Engineering Command Alexandria, VA 22331 ATTN: Code 03	1
Oak Ridge National Laboratory Metals and Ceramics Div. P.O. Box X Oak Ridge, TN 37380	1
Los Alamos Scientific Lab. P.O. Box 1663 Los Alamos, NM 87544 ATTN: Report Librarian	1
Argonne National Laboratory Metallurgy Division P.O. Box 229 Lemont, IL 60439	1
Brookhaven National Laboratory Upton, Long Island NY 11973 ATTN: Research Library	1
Lawrence Berkeley Lab. 1 Cyclotron Rd Berkeley, CA 94720 ATTN: Library	1
Naval Surface Warfare Center Annapolis Detachment Annapolis, MD 21402-5067 ATTN: Code 61 Code 613 Code 0115	1 1 1

4315DIST
04 June 1993

Supplemental Distribution List

Profs. G.H. Meier and F.S.Pettit
Dept. of Mat'ls Science & Eng.
848 Benedum Hall
University of Pittsburgh
Pittsburgh, PA 15261

Dr. G. D. Davis
Martin Marietta Laboratories 848
1450 South Rolling Rd.
Baltimore, MD 21227-3898

Prof. Gordon P. Bierwagen
North Dakota State University
Dept. of Polymers and Coatings
Box 5227
Fargo, ND 58105

Dr. S.M. Lipka
Dept. of Ocean Engineering
Florida Atlantic University
Boca Raton, FL 33431-0991

Prof. H.W. Pickering
The Pennsylvania State Univ.
209 Steidle Bldg.
University Park, PA 16802

Dr. D.D. Macdonald
The Pennsylvania State Univ.
517 Deike Bldg.
University Park, PA 16802

Prof. D.J. Duquette
Dept. of Metallurgical Eng.
Rensselaer Polytechnic Inst.
Troy, NY 12181

Dr. B.G. Pound
SRI International
333 Ravenswood Ave.
Menlo Park, CA 94025

Prof. D. Tomanek
Michigan State University
Dept. of Physics and Astronomy
East Lansing, MI 48824-1116

Prof. C.R. Clayton
Dept. of Materials Science & Eng.
State University of New York
Stony Brook
Long Island, NY 11794

Dr. M. W. Kendig
Rockwell International Sci.Ctr.
1049 Camino Dos Rios
P.O. Box 1085
Thousand Oaks, CA 91360

Dr. J.W. Oldfield
Cortest Laboratories Ltd
23 Shepherd Street
Sheffield, S3 7BA, U.K.

Prof. R. A. Rapp
Dept. of Metallurgical Eng.
The Ohio State University
116 West 19th Avenue
Columbus, OH 43210-1179

Ms. D.M. Aylor
Code 613
Naval Surface Warfare Center
Annapolis, MD 21402-5067

Dr. R.D. Granata
Sinclair Laboratory #7
Lehigh University
Bethleham, PA 18015

Prof. K. Sieradzki
Dept. of Materials Sci. & Eng.
The Johns Hopkins University
Baltimore, MD 21218

Dr. P.S. Pao
Code 6326
Naval Research Laboratory
Washington, D.C. 20375-5343

Dr. W.P. Allen
United Technologies Research Ctr.
East Hartford, CT 06108

Dr. B.A. Shaw
Dept. of Eng. Sci. & Mechanics
207 Hallowell Building
The Pennsylvania State University
University Park, PA 16802-1484

Dr. P. Cox
SRI International
333 Ravenswood Ave.
Menlo Park, CA 94025-3493

Dr. R. E. Ricker
National Institute of Standards and Technology
Bldg. 223, Room B-266
Gaithersburg, MD 20899

Dr. F.B. Mansfeld
Dept. of Materials Science
University of Southern California
University Park
Los Angeles, CA 90089-0241

Prof. R.E. White
Dept. of Chemical Engineering
University of South Carolina
Columbia, SC 29208

Prof. R.A. Buchanan
Dept. of Materials Science & Eng.
University of Tennessee
Knoxville, TN 37996-2200

Dr. B.J. Little
NRL Detachment
Bldg. 1105, Room D415
Stennis Space Center
MS 39529-5004

Prof. M.E. Orazem
Dept. of Chemical Engineering
University of Florida
Gainesville, FL 32611

Prof. J. O'M. Bockris
Dept. of Chemistry
Texas A & M University
College Station, TX 77843

Dr. V. S. Agarwala
Code 6062
Naval Air Warfare Center
Warminster, PA 18974-0591

Prof. R.C. Newman
UMIST
Corrosion and Protection Center
P.O. Box 88
Manchester M60 1QD, U.K.

Prof. S. C. Dexter
College of Marine Studies
University of Delaware
700 Pilottown Rd
Lewes, DE 19958

Prof. R.P. Gangloff
Dept. of Mat'ls Science & Eng.
Thornton Hall
University of Virginia
Charlottesville, VA 22903-2442

Dr. R. Brown
Dept. of Chemical Engineering
University of Rhode Island
Kingston, R.I. 02881-0805

Dr. J. Jones-Meehan
Code R301
Naval Surface Warfare Center
10901 New Hampshire Ave.
Silver Spring, MD 20903

Dr. P. Natishan
Code 6322
Naval Research Laboratory
Washington, D.C. 20375-5343

Dr. R. L. Jones
Code 6170
Naval Research Lab.
Washington, D.C. 20375-5342